Masters in Mechanical Engineering
Faculdade de Engenharia da Universidade do Porto

Master's Dissertation in:

Production of Sustainable Composite Powders for Direct Energy Deposition (DED)

Author:
João Pedro Castro Conceição

Advisor at FEUP:
Professora Dra. Ana Rosanete Reis

Advisor at Inegi:
Dr. Omid Emadinia

26/09/2022

'There is only one thing that makes a dream impossible to achieve: the fear of failure.'

Paulo Coelho

Abstract

Additive manufacturing (AM) processes, such as Direct Energy Deposition (DED) or Selective Laser Melting (SLM) originate residue powders that are wasted. The reuse of this material can become a sustainable alternative to existing resources, and thus add value to the waste produced. To these powders, a reinforcement can be added and therefore create hardened coatings or metal matrix composite structures via AM.

This study investigates the printability of a reused Inconel 625 powder with and without Alumina particles through the DED process. A mixture with 10 wt.% Alumina was prepared by ball mill shaking process for 9 hours. The parametrization of these powders was done by printing different lines on an AISI 4140 substrate.

Obtaining an optimised bead geometry was targeted by considering laser power, scanning speed and powder feed rate, to subsequently perform the printing of 20x20 mm^2 planes (one and three layers), considering different printing patterns and overlaps.

Cross-section evaluations on the polished samples included analyses of the porosity and microstructure of the material, as well as microhardness measurements of the material. The microscopic observations involved optical and scanning electron microscopies.

The residue powder after printing, was compared with the commercial one exhibiting similar hardness and oxidation. For the Inconel 625 residue powder combined with alumina, the mixing process influenced the roughness of the metallic particles damaging the flowability of the material, which hindered the printing process. Furthermore the microstructure of the printed mixture displayed a gamma matrix containing very small aluminium oxide particles, with reinforcement agglomerations on the surface of the printed material.

Additionally to both studied powders, the printing of the commercial powder Metco 51060A, was also performed in order to complement the study, following the same procedure. The material despite exhibiting a complex microstructure with the precipitation of carbides in different forms (angular blocks, dendrites, spherical particles), presented cracks and porosities of varying dimensions.

Keywords: Metal Additive Manufacturing, Direct Energy Deposition, Sustainability, Metal Matrix Composites, Inconel 625, Alumina, Metco 51060A, AISI 4140

Resumo

Processos de fabrico aditivo (AM), como Direct Energy Deposition (DED) ou Selective Laser Melting (SLM) originam pós resíduos que são desperdiçados. A reutilização deste material pode se tornar uma alternativa sustentável aos recursos já existentes, e assim acrescentar valor ao desperdicio produzido. A estes pós, a adição de um reforço pode ser efetuada e por conseguinte criar revestimentos endurecidos ou estruturas compósitas de matriz metálica via AM.

Este estudo investiga a capacidade de impressão de um pó Inconel 625 anteriormente utilizado com e sem partículas de Alumina através do processo de DED. Uma mistura com 10 wt.% de alumina foi preparada através do processo de ball mill shaking durante 9 horas. A parametrização destes pós foi efectuada através da impressão de diferentes linhas num substrato AISI 4140.

A obtenção de uma geometria optimizada de cordão foi procurada considerando a potência do laser, a velocidade de scan e a taxa de alimentação de pó, para posteriormente efetuar a impressão de planos de 20x20 mm^2 (uma e três camadas), considerando diferentes padrões de impressão e sobreposições de camada.

As avaliações em secções transversais nas amostras polidas incluíram análises da porosidade e microestrutura do material como também de medição de microdureza do material. As observações microscópicas envolveram microscopias electrónicas de scan e ópticas.

O pó resíduo após impressão, foi comparado com o comercial exibindo dureza e oxidação semelhantes. Para o pó resíduo de Inconel 625 misturado com alumina, o processo de mistura influenciou a rugosidade das partículas metálicas prejudicando a fluídez do material, o que dificultou o processo de impressão. Para além disso a microestrutura da mistura imprimida apresentou uma matriz gama contendo partículas muito reduzidas de óxido de alumínio, com aglomerações de reforço na superfície do material impresso.

Adicionalmente a ambos os pós estudados, a impressão do pó comercial Metco 51060A, também foi realizada de forma a complementar o estudo, seguindo o mesmo procedimento. O material apesar de exibir uma microestrutura complexa com a precipitação de carbonetos sob diferentes formas (blocos angulares, dendrites, partículas esféricas), apresentou fissuras e porosidades de dimensões variadas.

Palavras-Chave: Fabrico Aditivo Metálico, Direct Energy Deposition, Sustentabilidade, Compósitos de Matriz Metálica, Inconel 625, Alumina, Metco 51060A, AISI 4140

Acknowledgements

Throughout the study developed both in the research of the theoretical aspect, as in the course of all steps taken in the practical part, much time and effort was spent. The work carried out in this thesis, however, would not have been possible without the contribution of the people mentioned below, whom I thank:

To Dra.Ana Reis, who thanks to her experience and mentoring ensured the best possible path.

To Dr.Omid Emadinia, to whom I would like to express my gratitude, as he not only welcomed me in the best way at INEGI, but also did everything possible to help throughout the study, with his kindness and availability.

To Engineer Jorge Gil, who always demonstrated to be open in the accomplishment of the work, either to eventual doubts or in the accomplishment of the metallic impressions with all his sympathy, and also for the performance of printings;

To the engineer Fahad Zafar who provided his contribution during the work and to Lara Castanheira who also followed the same journey in her dissertation and was always willing to help. To Armanda Teixeira and Emilia Soares who helped in the preparation and image acquisition of the samples.

To all INEGI collaborators, which I had the pleasure of meeting and who treated me with respect and sympathy.

To my parents, to whom I had the privilege of being raised, and who always made every effort to give me everything I needed, and who always did everything to enable me to succeed in life. To my sister Joana Alves and my cousin Daniela Nunes, who were always available to give me advice and to be there for me whenever I needed.

To my other family, which includes uncles, cousins and my grandmother, whom I thank for helping me to become who I am today.

To Inês Santos, who was my company and stood by me even when things got complicated.

To my friends, who allowed me to make amazing memories, before and during the course of the 5 years of college. To my uncle and grandfather, who are no longer present and who will be somewhere watching over me.

To you all I am eternally grateful,

João Castro

Institutional Acknowledgements

Gratefully acknowledge the financial support form Portuguese Foundation for Science and Technology (FCT) under the projects UIDB/50022/2020, UIDP/50022/2020, ADDing (POCI-01-0145-FEDER-030490), Add.Strength (POCI-01-0145-FEDER-031307) and MAM-Tool (POCI-01-0145-FEDER-031895) by UE/FEDER through the programs COMPETE 2020.

Also express gratitude to CEMUP(Centro de Materiais da Universidade do Porto) for expert assistance with SEM, and to the department of Metallurgical and Materials Engineering for providing powder analysis and milling facilities.

Contents

List of Figures

List of Tables

Abbreviations

AM - Additive Manufacturing

ASTM - American Society for Testing and Materials

BTF - Buy-to-Fly ratio

CAD - Computer-aided Design

CCA - Close-Coupled Gas Atomization

CEMUP - Materials Centre of the University of Porto

CIP - Close Isostatic Pressing

CNTs - Carbon Nanotubes

DED- Direct Enegy Deposition

DMD- Direct Metal Deposition

DLF- Direct Light Fabrication

DLS- Dynamic Light Scattering

EDS - Energy Dispersive Spectroscopy

EIGA - Electro Induced Gas Atomization

FGM - Functionally Graded Material

HAZ - Heated Affected Zone

IN625 - Inconel 625

IN718 - Inconel 718

INEGI - Institute for Science and Innovation in Mechanical and Industrial Engineering

LAM-DED - Laser Additive Manufacturing Direct Energy Deposition

LENS - Laser Engineered Net Shaping

LMD - Laser Metal Deposition

LSF - Laser Solid Forming

MMC - Metal Matrix Composite

PBF - Powder Bed Fusion

PSD - Particle Size Distribution

rpm - Rotations per Minute

SEM - Scanning Electron Microscope

SLM - Selective Laser Melting

SLS - Selective Laser Sintering

SMA - Shape Memory Alloys

STL - Standard Triangle Language

TEC - Thermal Expansion Coefficient

WAAM - Wire Arc Additive Manufacturing

WEAM - Electron Beam Wire Additive Manufacturing

WLAM - Laser Wire Additive Manufacturing

Symbols

Ad - Deposit Area

As - Dilution Area

D - Depth

d10 - It is the maximum particle diameter that exists in that range for 10% of a sample

d50 - It is the maximum particle diameter that exists in that range for 50% of a sample

d90 - It is the maximum particle diameter that exists in that range for 90% of a sample

Da - Distance between adjacent strands

$\mathbf{E}_{specific}$ - Specific Energy

FR - Powder Feed Rate

H - Height

HV - Vickers Hardness

$\mathbf{K}_{IC}$ - Fracture Toughness

LEIPUL - Laser Energy per Unit Length

LP - Laser Power

$\mathbf{O}_R$ - Overlap Ratio

$\mathbf{P}_{density}$ - Powder Density

Ra - Roughness

$\mathbf{SE}_{density}$ - Specific energy density

SS - Scanning Speed

vol.% - Volume Percentage

W - Width

wt.% - Weight Percentage

Φ - Spot Size Diameter

Chapter 1

Introduction

1.1 Layout

The present thesis will be addressed by segmenting the research into five distinct chapters, which includes:

1. **Introduction-** Throughout this current chapter, a context for the addressed topic is provided, as well as the proposed aims during the period of the current study;
2. **State of the Art-** Theoretical research in the approached field is conducted to support and supplement further experimental results;
3. **Materials and Methods-** An overview of the equipment, materials and experimental techniques required are supplied;
4. **Results and Discussion-** With the results obtained, a comprehensive analysis and discussion of these findings is performed;
5. **Conclusion and Future Works-** In the last section, series of conclusions achieved throughout the study are presented, as well as future works, recommendations based on the investigation conducted;

1.2 Context

Nowadays, the manufacturing area is evolving, where the conventional processes are getting aided with a new branch of technologies, known as additive manufacturing processes. With these new methods, there is a chance to use the benefits of these new techniques, in order to revolutionize the way products are created, such as achieving faster manufacturing rates, free design, as well as a reduction in the waste obtained.

Despite the new benefits inherent in these new technologies, there are still issues that must be addressed, as the case of the cost of the raw material needed to build the pretended part, the post processing or the cost of entry since these new technologies are initially expensive and difficult to afford.

The development for alternative resources is becoming increasingly important in order to reduce costs and enhance the appeal of AM processes. Using sustainable approaches to avoid the present rise in material prices is thus becoming vital.

Using the Direct Energy Deposition technique, a method implemented in this thesis, metal powder is used and melted on a substrate in order to create different layers and form a part. During the process a portion of the powder is not used and ends up being wasted.

This waste powder may be recovered to create feedstock material, giving it a new life and providing an effective alternative to virgin powder. It is possible to combine this residue, specifically Inconel 625, with ceramic reinforcement to create a matrix composite material capable of enhancing the mechanical properties of the base material and therefore adding value to a depreciated material.

This work proposes the mixing of the waste powder, with an alumina ceramic reinforcement and from the DED machine technique, the parameterization of both the mixture and the waste powder. With the following printing of one and three layer plans, the impact of the waste and virgin powder quality are evaluated, as well as the reinforcement powder mixture from microstructural and/or hardness assessments of the printed material.

In addition to the IN625 residue powder mixture, a commercial Metco 51060A powder, which already has WC reinforcement mixed into the base metal powder, was printed and analyzed as a basis for comparison with the targeted mixture, for the first time at the INEGI facilities.

1.3 Objectives

As mentioned before, the main focus of the current dissertation is the creation of a metallic matrix composite by adding value to residue powder using the direct energy deposition (DED) process. For this, there is a combination of intermediate objectives necessary to accomplish and thereby complete the final goal. Of these, the following stand out:

1. Review of the state of the art, in order to complement the experimental side, which includes: mixing and parametrization, additive manufacturing of IN625 composites, as well as researched literature related to the powder recycling, formation of metal matrix composites and streghtening mechanisms;
2. Characterization of the conditions and mixing of the metallic powder with ceramic reinforcement;
3. Inconel 625 residue powder parametrization and subsequent residue, as well as virgin material printing of one and three layer plans on an AISI 4140 substrate;
4. Inconel 625-Alumina powder printing of one and three layer plans on an AISI 4140 substrate;
5. Metco 51060A powder printing of one and three layer plans on an AISI 4140 substrate;
6. Evaluation of the final results, based on the analysis of the microhardness, density and metallography of the printed materials, and further results discussion.

Chapter 2

State of the Art

2.1 Additive Manufacturing Sustainability

In light of the alarming industrial impact on the environment, both in terms of resource consuming, waste handling, and pollution prevention, sustainability is becoming increasingly crucial [1]. In general, additive manufacturing technologies have come to provide considerable environmental advantages to the industry since their usage, when compared to subtractive techniques, creates significantly less waste, which may be reduced by up to 90% through the use of these methods [1, 2].

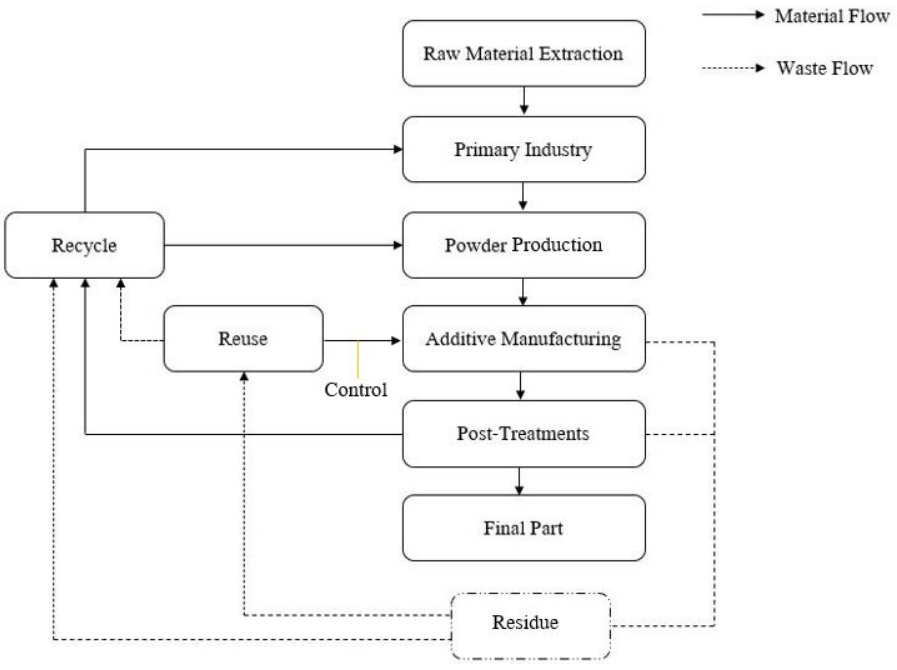

Figure 2.1: Circular metal AM economy cycle, adapted from [4].

Although waste is decreased, raw materials that are not utilized throughout manufacturing cycles continue to exist, including powders that cannot be recycled, waste caused by

unanticipated errors, and support structures for the original item [1]. In response to this issue, and in reaction to today's increasing consumption for products and goods, the idea of circular economy emerges [3].

The circular economy (figure 2.1) is described as preserving the value of goods, materials, and resources for as long as possible through waste reduction, reuse and recycling [4]. With the closed cycle, it is feasible to give discarded material new life and so promote natural resource preservation while also minimizing costs production.

In circumstances where the material is damaged and cannot be reused, it can be remelted using metallurgical procedures and, following chemical correction, returned to powder form, allowing it to be recycled and utilized in succeeding manufacturing cycles [4].

2.2 Powder Production

To produce metallic powder, a critical raw material for additive manufacturing techniques, there are a variety of procedures that can be used to convert the base material. Figure 2.2 depicts the various steps in the production of metallic powder, in which atomization (via water, air, gas, centrifugation, or plasma), mechanical friction, melt spinning, chemical processes and so forth may all be used to alter the original material in the final product, being water and gas atomization the most popular techniques [5, 6].

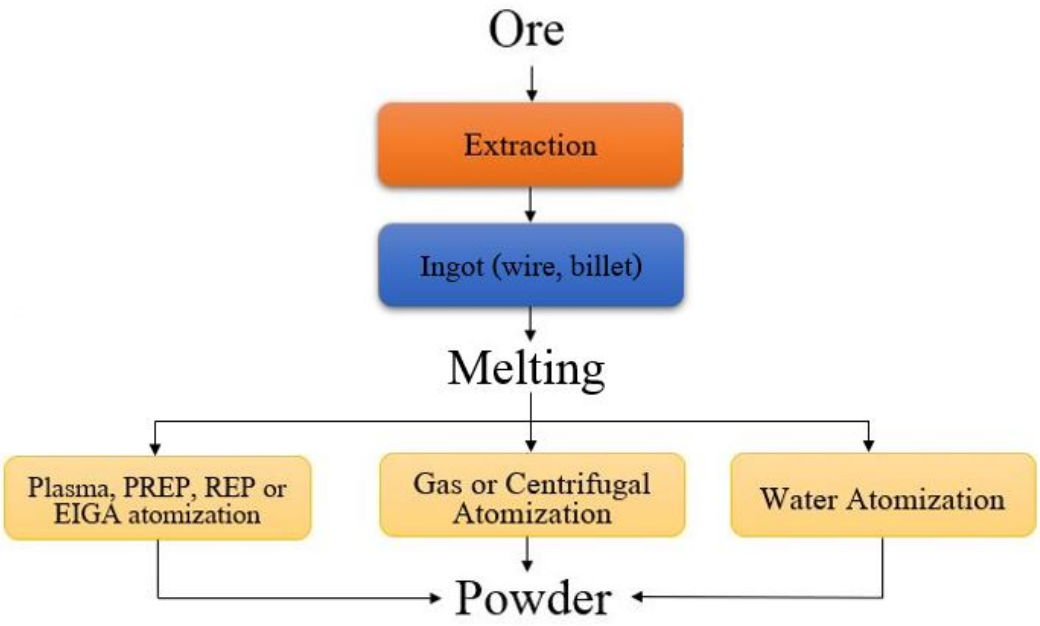

Figure 2.2: Flowchart for the manufacture of metallic powder by atomization means, adapted from [9].

Initially, open or closed systems melt the material with the appropriate form and geometry and the liquid material in open systems is contacting with the environment, while the slag layer covers the liquid metal. Closed systems employ vacuum as a casting environment to avoid oxidation of the material that occurs when it comes into contact with air, as well as degassing of the material feedstock without causing atmospheric pollution and excluding undesired residues of material constituents from the system [7].

After the metal fuses, the atomization process begins, which goes through two stages. In the first process, the liquid metal is sliced into small liquid particles by the atomization type selected, and furthermore in the second step, the metallic droplets generated earlier solidify to form the metallic powder [8].

2.2.1 Water Atomization

In water atomization, the alloy is heated in an induction furnace until it reaches the liquid condition before being put into a tundish. To atomize the material as it pours, a water jet is released by a high-pressure pump [7].

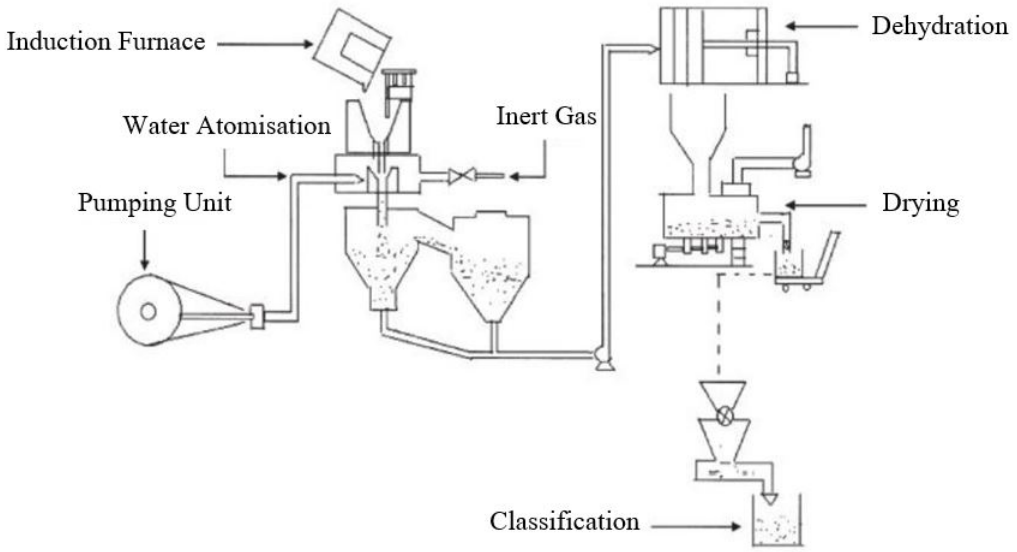

Figure 2.3: Flowchart for the manufacture of metallic powder, adapted from [8].

The resultant water-metal powder combination is then dried and subsequently classified and separated into suitable sizes as seen by figure 2.3 [7]. The uneven form of the particles affects packing and flow characteristics, although it may also be modified by atomising settings [9, 6].

2.2.2 Gas Atomization

To fractionate the molten metal, gas atomization can be performed using air, steam, or an inert gas, where the procedure takes place under a protective atmosphere or under vacuum conditions. It can also be melted in an induction furnace or a gas furnace, where it is moved from a shell to a tundish and reduced to powder using gas jets [8].

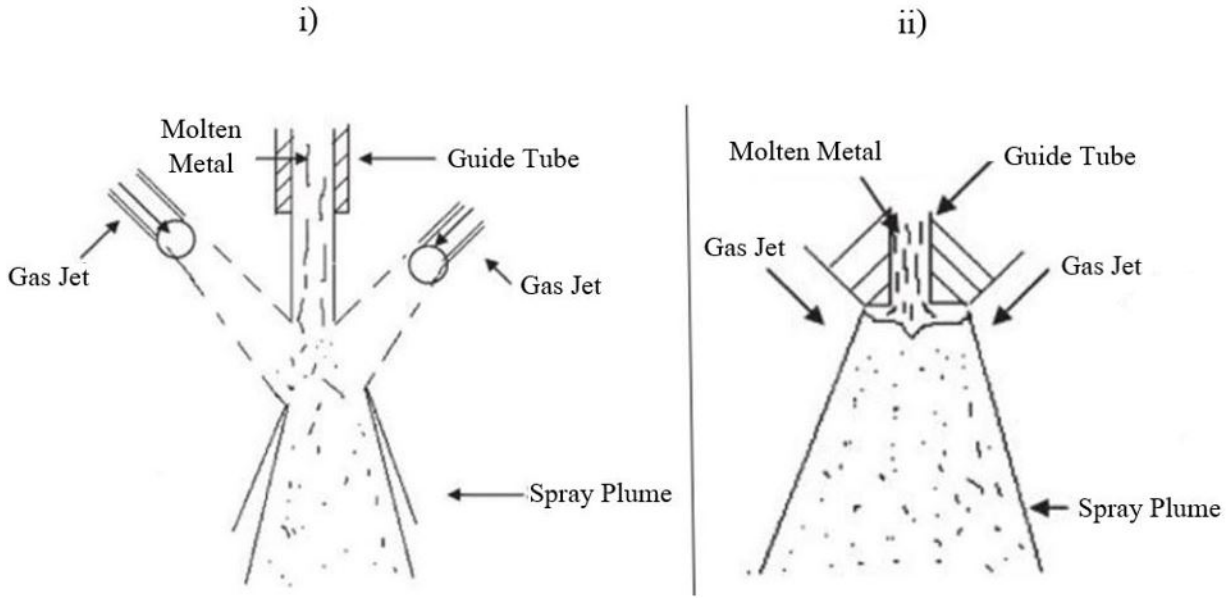

Figure 2.4: *i)* Free-fall atomization and *ii)* Close-coupled gas atomization processes, adapted from [8].

The technique can be carried out using either free-fall atomization or closed-coupled gas atomization (CCA). In free-fall atomization (figure 2.4*i*), the molten metal falls for a predetermined distance before being struck by the jets, causing the molten metal to form spherically shaped droplets of varying sizes that solidify when they come into contact with the gas jets. In contrast to the preceding situation, in closed-coupled gas atomization the gas jets (figure 2.4 *ii*) are positioned near the exit of the liquid metal, allowing for finer particles but with backflow issues [7].

Another method to avoid contamination of the molten metal by ceramic particles in the induction crucible or the tundish is to employ the Electrode Induced Gas Atomization Process (EIGA), that can also be used for reactive alloys. An induction coil is utilized instead of a crucible furnace to heat the feedstock material, which is melted and sent to the jets of inert gas where it is atomized [10].

2.2.3 Plasma Atomization

Plasma atomization (figure 2.5) is a method of producing high purity and sphericity powders by the use of plasma torches in an inert atmosphere [7]. This process is used to make powders with a minimal level of oxygen, in which the feedstock material, that is in the form of metallic wire, is placed in contact with plasma jets in order to melt the material and create droplets [7].

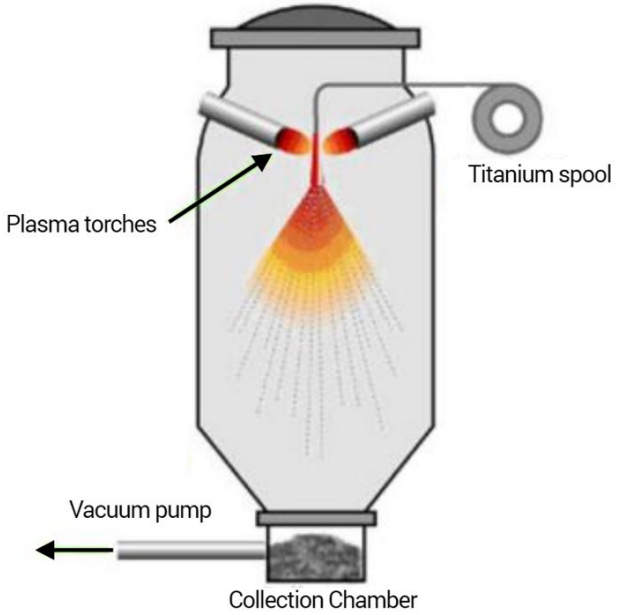

Figure 2.5: Plasma atomization process, adapted from [9].

Despite creating high-quality powders, the technique is limited in the raw materials it may employ. There must be the option of converting the metallic substance into a wire, which comes at a significant cost and is thus the only method to use this technology [11].

2.3 Powder Characteristics

One of the significant aspects regarding the printing process is the characteristics that the powder has to present, which will later affect the printing quality due to the strong influence on both flowability and density. These aspects are namely:

- Particle size and size distribution (PSD);
- Powder morphology;

- Powder Structure [12].

Particle size as the name indicates refers to the particle dimension that can be measured by its nominal diameter, whereas particle size distribution refers to the range of values that defines the relative quantity, usually by mass, of particles present according to their size. Normally the nomenclature d10, d50 and d90 can be used in PSD, to refer to each of these percentages is the maximum particle diameter that exists in that range. The PSD and the particle size, can directly influence the packing behaviour of the powder, depending on the variation of the range of existing particles [13]. This characteristic can be ascertained by methods such as laser diffraction or dynamic light scattering (DLS) [14, 15].

Powder morphology is another factor that turns out to be important, as particles can acquire different shapes such as spherical, porous or irregular. As with PSD, morphology also influences packing, as it does in other important aspects such as density and flowability, since spherical and smooth particles are more appreciated than irregular and rough ones, given that in addition to the improvement seen in flowability, in the case of metallic additive manufacturing methods, it also ensures uniform flow [16]. The shape of the particles can be analysed using scanning electron microscopy (SEM) and x-ray computed tomography [14].

Finally the particle structure assumes a major role in the characterisation of metallic powders. Factors such as atomic arrangement are important to be analysed that will have an influence on the degree of crystallinity and consequently affect the microstructure of the powder, of which include the phases that constitute the material, subsequently affecting the mechanical properties of the material. Its verification can be done using electron transmission microscopy (TEM), X-ray diffraction (XRD) or electron backscatter diffraction (EBSD) analysis [12].

2.4 Powder Reuse and Recycling

As mentioned earlier the first phase of the study focuses on the reuse of powder obtained from the DED process. The use of these powders contains certain advantages, however they can cause several issues that can difficult their use.

The main advantage of using reused powders, being also the principal goal of their usage, is the reduction of costs alluding to the price of the printing material that can become an efficient alternative to high-priced powders. Considering the material residue (figure 2.6) during depositions, a small proportion is thermally affected with the possibility to be partially oxidized and melted or even suffer chemical changes [17].

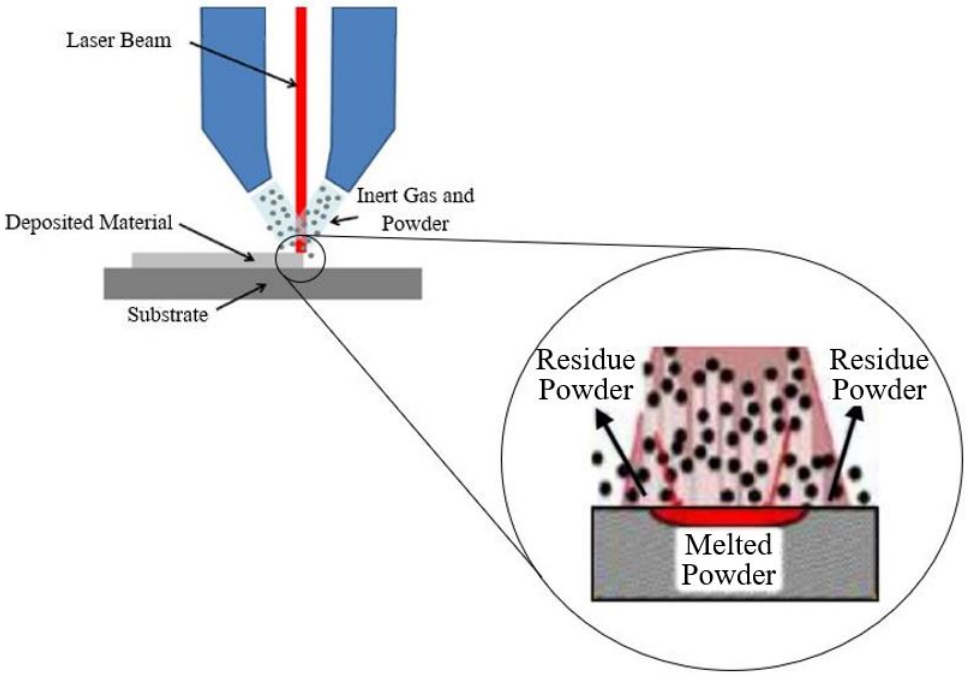

Figure 2.6: Schematic of the waste production during DED process, adapted from [17,39].

Recycling is delicate depending on the process employed. In methods like PBF, recycling is more critical, as the costs of metal powder are higher than for techniques like DED, and additionally, as a powder bed is required, the residue quantities are also higher. The direct energy deposition process, contrary to the previous one, registers lower quantities of waste, nevertheless the study of recycling can reveal the residue to be a sustainable alternative [17]. However, regardless of the process addressed, as the reuse cycles augment, there is an increase in the oxygen content in the metallic powder, which can cause an augment in the density of associated defects such as oxide formation, which may later affect both mechanical properties and final parts [17, 18, 19].

In the reuse of powders, some particles are partially melted and form agglomerates, creating particles of larger sizes that can be removed by seiving, however very fine particles that were affected by the process and particles of high proportion tend to pass through the mesh in the cleavage method [20].

It is also verified that during the reuse cycles the properties rarely change demonstrating high resistance during reuse, and maintenance of the spherical shape, despite a residual percentage of particles showing modifications in their size and morphology. Although particles can present some degradation, their phase composition and hardness hardly change [21]. Therefore, the material should be inspected in order to eliminate the presence of contamination's and particles with undesirable sizes.

2.5 Additive Manufacturing

As the name indicates, additive manufacturing techniques relate to the act of constructing items by adding material, as opposed to removal procedures such as machining. This methodology enables the creation of parts using 3D computer models, where the material is printed, cured, or consolidated selectively, layer by layer, allowing for the creation of very complex geometries, which are difficult, if not impossible, to achieve using traditional processes [22].

A CAD model, or virtual model of a desired part, can be created using software intended for this purpose, such as AutoCAD or Solidworks. Other methods, such as image capture, which includes scanning, can also be used to obtain this model [23].

The CAD is turned into an STL file, which emphasizes the geometry of the part by eliminating common design features such as textures [23]. The geometry is represented by triangles derived from Cartesian coordinates on the x, y, and z axes [24]. The STL with the part information is then sliced into many horizontal layers based on the geometry of the component, generating the g-code that permits the material to be printed using the selected technique [23]. This sequence is represented in the figure 2.7.

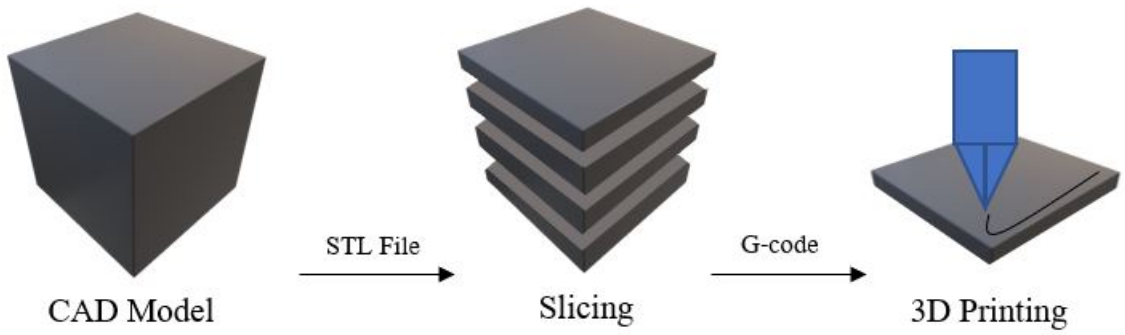

Figure 2.7: Additive manufacturing process steps, adapted from [23,24].

AM technologies have grown tremendously over the last 30 years, progressing from a promising but uncommercialized industry in the 1980s to a method with a value in the range of 4 billion dollars in 2014, and with a large estimate of growth over the years, where products generated by additive manufacturing procedures can now reach a wide range of activities such as art, architecture, or education, and also enable the direct manufacture of final parts in a variety of industries, as medical, dental or aerospace [25].

This increased popularity is due to a plenty of advantages that traditional techniques do not provide. This variety of approaches provides significant design freedom without large constraints or the requirement for additional external tools, which promotes great customization that fits market need. However, it still has several issues that need to be addressed, such

as slow build rates, which hinder the manufacturing of high volume productions, and surface quality that requires post-treatment. Furthermore, the machines are still expensive in industrial terms, and the majority have build size constraints [26].

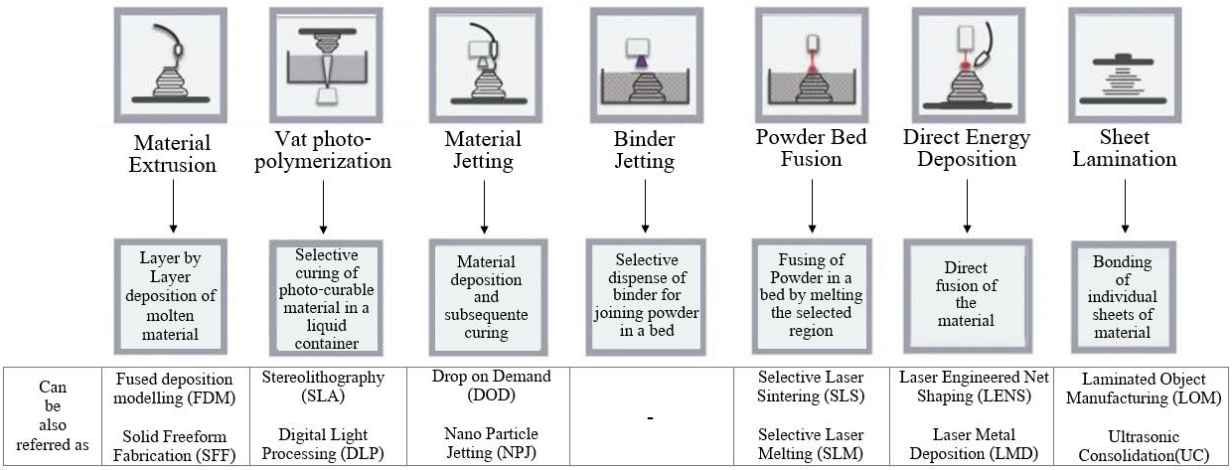

Figure 2.8: Classes of AM technologies, adapted from [30].

ASTM International has classified AM processes into seven groups: material extrusion, vat photo-polymerization, material jetting, binder jetting, powder bed fusion, sheet lamination and direct energy deposition [27]. Classification may be accomplished in a variety of ways, one of which is by the type of material utilized or the condition of the raw material, which can be liquid, discrete particles, or solid sheets [28].

Thermoplastics are used as raw materials in processes like material extrusion, vat-photopolymerization, and material jetting. Amorphous thermoplastics such as PLA or ABS, due to their melting qualities, are employed in material extrusion. Photosensitive polymers, such as epoxies or acrylics, are commonly used for vat-photopolymerization and material jetting. PBF and DED procedures are the most often utilized commercially to generate excellent metallic components from metallic raw materials [29, 30].

Inside the AM technologies shown in figure 2.8, the DED process is the method that will be used to perform the depositions furthermore in the present dissertation as previously mentioned. As a result, this technology will be duly investigated in the following sub-chapters.

2.5.1 Direct Energy Deposition Method

2.5.1.1 Process

Direct Energy Deposition is an AM process that allows, from the feedstock material, which can be powder or wire, the fusion of the input material with a source of heat, at

the same time it deposits it in a substrate, creating a meltpool and further a bond between the additive, the base material and the previous line [31]. As the material solidifies on the substrate, the DED machine moves and forms a path, creating a layer. Subsequently, the machine nozzle increases its height in relation to the substrate and the bead formed, to generate other layers until the desired part is finished [32].

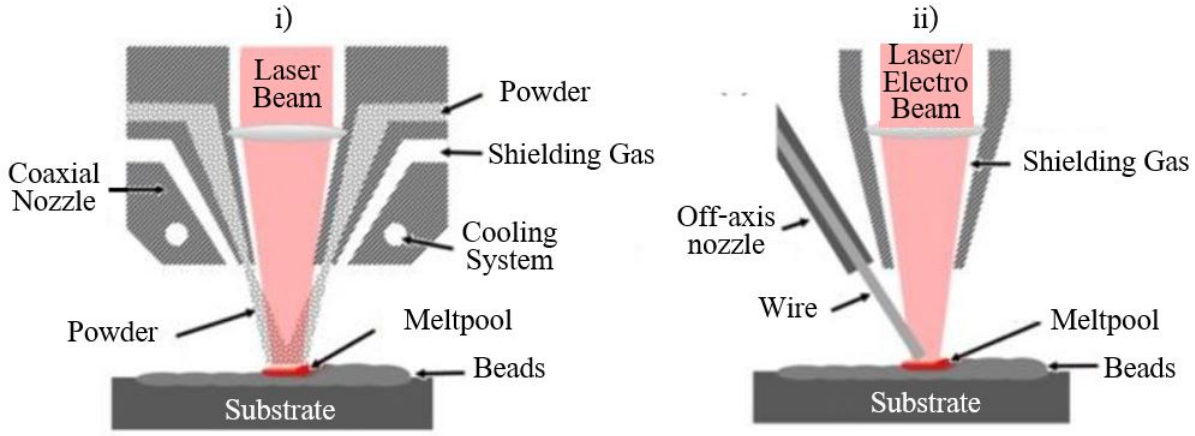

Figure 2.9: DED process with i) powder and ii) wire feedstock, adapted from [32].

The type of heat source varies with the machine used, where laser, electro beam or plasma/electric arcs can be used [33]. Most machines use a continuous pulse in order to manufacture the part, and the type of laser, as well as its maximum capacity, can vary. Typically, Nd:YAG (neodymium-doped yttrium aluminum garnet) lasers are the most used, since the spectral radiation emitted is less reflected by the metal, with an available power between 1 and 5 kW, however it is possible to use a wide variety of other alternatives, such as pulse-varying or CO_2-type lasers [34, 35].

CO_2-type lasers contain higher wavelengths with lower material energy absorption compared to Nd:YAG lasers, and because of this, higher powers are required to melt both the input material and the substrate, with maximum capacities up to 18 kW [34, 35]. For the creation of simpler and low-precision parts, the use of CO_2 lasers are more appropriate, in which, instead of this, the use of Nd:YAG lasers are more qualified to generate finer and more complex parts [36].

Direct Energy Deposition can be classified based on the input material and/or the heat source, i.e. the material used for deposition can be a powder feedstock or wire type though the source of energy can be provided by laser, electric arc and electron beam. However, depending on the feedstock and the type of energy source, the process can be classified into different nomenclatures. Within the processes where a wire feedstock is applied, energy sources such as laser, electric arc and electron beam can be employed, where for powders only laser energy sources are applicable.

Regarding powder-based methods, the process can also be referred to as LENS, LMD, DMD, LSF or DLF [33].

Some differences are also pointed out for the protective atmosphere employed. In the case of LAAM-DED, WAAM and WLAM, a shielding gas is used and for WEAM a vacuum atmosphere is typical [32]. He or Ar are used as protective gases in order to prevent oxidation and contamination of both feedstock and substrate. Vacuum also serves to avoid these problems, as well as to allow obtaining parts free of porosity [37].

In direct energy deposition, the machine is very adaptable, having a wide range of materials that can be used. Ceramic or composites are feasible, being metal the most common material. Stainless and tool steels and similarly titanium-based, nickel-based, aluminium, copper, high entropy, intermetallic or shape memory (SMA) alloys can be applied [38].

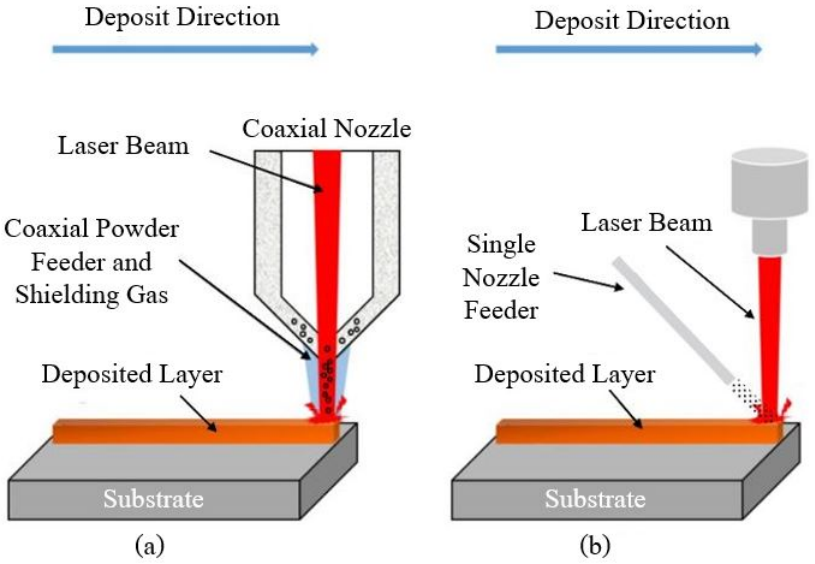

Figure 2.10: DED process with a) coaxial feeding and b) single-nozzle feeding, adapted from [31].

For powder feedstock (figure 2.9i), the efficiency of powder capture is not total (<100%), with unused powder creating residues [39]. The addition of material to the substrate can be completed from a four-nozzle, coaxial or a single-nozzle feed [35]. Both coaxial and single-nozzle feeding are represented in the figure 2.10.

Coaxial feeding is done by introducing powder around the laser in a toroid configuration, using a protective gas. It has the great advantage, that the deposition has a greater powder capture effectiveness regarding all feedings, and allow the application of the shielding gas [35].

Machines with a single-nozzle are less expensive, with a greater powder catch efficiency than 4-nozzle feeding and higher capability of adding material in constrained areas. However, the use of this type of feeder has the problem of creating a meltpool with a particular direction,

depending on the nozzle configuration. The feeding of 4 nozzles is done by each of the nozzles positioned at 90 degrees around the laser source. The flow properties induced by the feeding enable better stability in building height in complicated geometries, which is its major benefit [35].

During deposition, the layers acquire a rough and wavy geometry typical of the DED process. The use of powder as a feedstock material, allows to reduce the geometry differences resulting from the combination of the different beads. Powder flow can be changed, impacting the resulting meltpool shape and, as a result, modifying the differences between neighboring beads, resulting in smoother surfaces [35].

In the case of wire feeding (figure 2.9ii), its volume is fully deposited on the substrate (=100%), obtaining a total capture of the raw material. This type of feed is used to create simpler geometries, without great variation in the thickness of each layer, since it is complicated with this technique to level the generated surface, as well as to change the orientation of the deposition direction enabling a deposition rate and layer thickness higher than powder feed. The use of powder facilitates direction changing, providing to the final part lower residual stresses [35, 32].

2.5.1.2 Advantages and Disadvantages

This additive manufacturing process contains certain advantages over conventional production processes, like the others belonging to this classification, which facilitate the buyer's preference for these for a given application. Among these, the following stand out:

- **A wide variety of feed stock materials** - As previously mentioned, possible to use ceramics, composites and metals;
- **Possibility to create multi-materials and FGM's** - Creation of parts with localized different material properties;
- **High deposition rates** - Superior to other AM technologies, as for example the PBF process;
- **Freedom of Design** - Possible to decide the desired design without limitations;
- **Deposition does not need to be done on a horizontal surface** - Due to the existence of multiple axis, the machine can deposit in surfaces with different angular disposals, with no need of supports;
- **Creation of larger pieces in comparation to the PBF process** - There is a high liberty of construction height of the pretended parts;

- **Good mechanical properties and larger particle powders** - Better static and dynamic mechanical properties in the deposited condition than in PBF process, allowing particles with larger dimensions to be used in comparation with PBF with laser;

However, certain aspects may limit the use of this machine depending on the final product to be obtained. These are:

- **Low resolution process** - The parts generated from the DED machine has difficulties in terms of geometric precision, being practically impossible to create the finest details;
- **High roughness** - Compared to other AM processes, the surface roughness of the layers are greater ;
- **Efficiency** - Has lower powder efficiency, when compared to the PBF process;
- **Post processing** - Due to the low resolution and complexity obtained in the final parts, there is a need for post processing techniques, in order to ensure and adjust the precision quality of the product [33].

2.5.1.3 Applications

Applications of the DED method are familiar to other additive manufacturing techniques, but also stand out due to the unique features and functionalities that this method gives to the final product. It's incidence reaches various fields such as the automotive, energy, biomedical or aerospace industries, taking advantage of the benefits of technology, such as good mechanical properties, design freedom and high customization of parts, with the aim of creating lightweight structures with a significant reduction in weight, achieving waste reduction and carbon dioxide emissions [40]. The most typical applications of the process can be seen in figure 2.11.

In addition to the production of parts, of which large dimensions components are included, it is also used to repair damaged parts and restore into a desired shape and/or mechanical properties, increasing wear resistance by hard coating and part life, while reducing costs and lead time when designing a new part [32]. Repair turns out to be a common industrial practice, especially in large pieces with high metallic value. This methodology can repair structures and add material to prevent and minimize future erosion or damage that may occur [33].

The metallic printing also contains a unique feature in the reuse of the material for a given purpose, in order to edit it by manufacturing a new part from an existing part, providing improved functionality, and thus avoiding the production of waste [41].

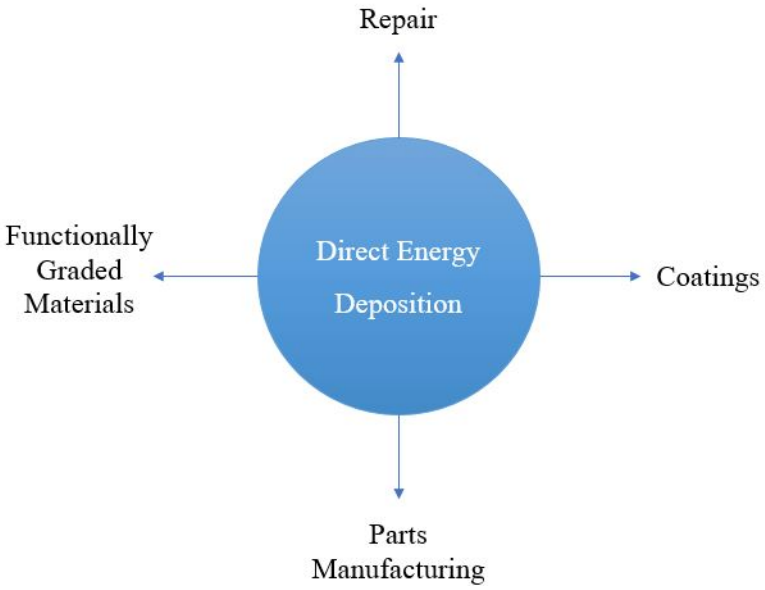

Figure 2.11: Common applications of the direct energy deposition method, adapted from [33].

The creation of porous materials and coatings, such as metallic foams and porous structures in biomedical materials, have been an emerging focus on additive manufacturing processes by DED, such as their use in implants, proving to be an alternative to conventional casting processes, improving biocompatibility and buy-to-fly (BTF) ratio, which consists of the mass used in the final piece compared to of the raw material. The possible use of materials with different properties also opens a window for the creation of tailored structures and materials, in which these mechanical or chemical properties vary locally depending on the type of powder used in a given layer or portion. This allows the creation of functionally graded materials (FGM's), multi-layer coatings of heterogeneous material, allowing better control of material properties, increasing corrosion and wear resistance [32].

Other studies on the application of the method in thermal management were carried out with the creation of conformal cooling channels and heat sinks for molding, forming and mold casting tools, improving control of temperature distribution, uniform and rapid cooling characteristics, reduced cooling and cycle time and improved material quality [32].

In the present dissertation, the main objective in terms of final application, focuses on the creation of value-added parts, in order to produce an advanced material of high hardness and/or wear resistance.

2.5.2 Parameters of DED

Some parameters inherent to the Direct Energy Deposition process, have the ability to influence the properties, characteristics and defects of the final part, and as a consequence

it is necessary to investigate these to obtain the best attributes of the material, from the manipulation of these variables.

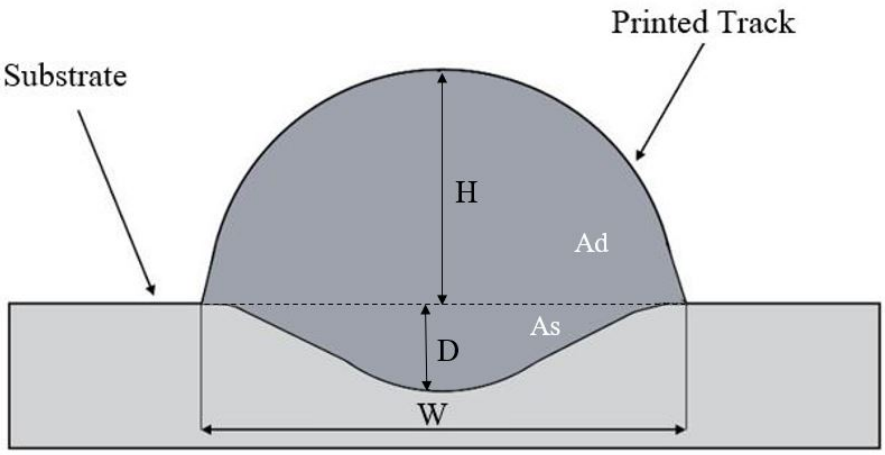

Figure 2.12: Schematic printed track during the DED process and significant dimensions, adapted from [43].

As the powder from the printing machine flows out, both the powder and the substrate melt, forming a meltpool and the Marangoni convection forces. Due to tension discrepancies between different regions of the meltpool, this phenomenon causes internal movements of molten material [42].

The presence of low surface tension values in the centre of the pool and high tension values at the solid-liquid frontier causes radial motions and material transport inside the printed material. The Marangoni Effect subsequently influences the dimensions of the melt pool [42].

These dimensions displayed in figure 2.12 become important, as dilution occurs in the substrate, by the deposited material. The dilution percentage can be calculated by the following expression, where Ad and As are respectively the deposit and dilution area [43].

$$Dilution(\%) = \frac{As}{As + Ad} \tag{2.1}$$

High levels of dilution have to be avoided, as they contribute to the deterioration of the mechanical and corrosion properties of the material [43]. However, a minimal amount is required to ensure the metallurgical bond between the substrate and the feed stock material, and similarly between the different neighbouring tracks and stacked layers, becoming crucial the monitoring of process parameters [44].

The height (H), depth (D) and width (W) of the deposits can be altered by the adjustable parameters, shown in figure 2.13.

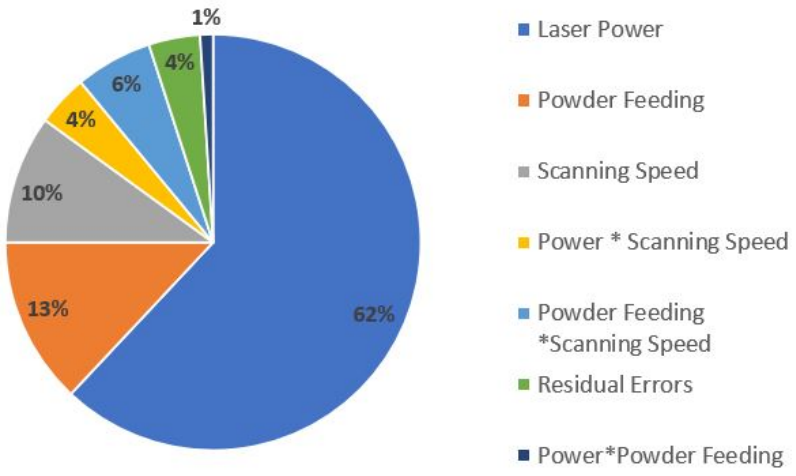

Figure 2.13: Major elements influencing the melted volume of the substrate, adapted from [42].

According to Goodarzi et al. of the existing parameters, there are three elements that possess a major influence on the final results of the deposited material, which are Laser Power, Scanning Speed and Powder Feeding. A significant influence is pointed out to the laser power with 62% of influence, and for the powder feeding rate it is evaluated as the second most important parameter in this analysis with 13%, being succeeded by the scanning speed with 10%. The relationships between parameters are also reported with little influence, as are uncontrollable residual errors in the process [42].

2.5.2.1 Laser Power

The quantity of energy given by the laser source and further applied to melt the filler material to the substrate is known as laser power. The power determined for the manufacture of the part must be carefully delineated, since the use of high laser amounts can lead to vaporization of the additive material, however at the same time low power can lead to improper fusion, and consequently creating defects, such as lack of fusion or porosity, or even no fusion of the material [41].

When the laser power increases, keeping the remaining parameters constant, induces an increase in the amount of molten material. It will cause the material residing in the substrate to increase it's melting, and consequently increase the dilution level of the metallic track, as depicted in figure 2.14. Otherwise, its reduction will lead to a smaller amount of energy for the same amount of material to be melted, which will reduce the amount of dilution [43].

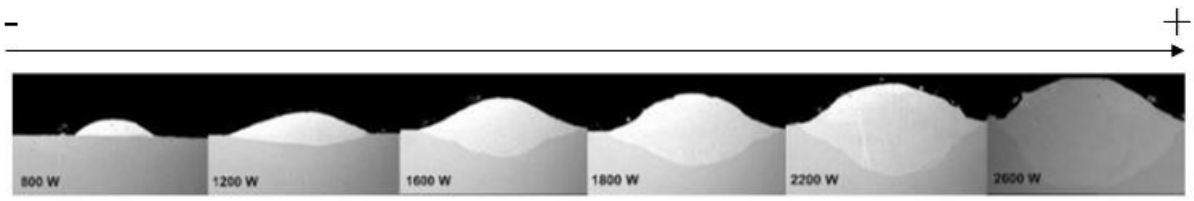

Figure 2.14: Influence of Laser Power in the melt pool area, adapted from [45].

With the increase in power, the depth and width of the melt pool also increases, unlike the height, which does not behave as linearly. Initially, for an increase at low powers, this tends to increase, and with the successive increase at higher powers this relationship begins to be eliminated, without notable differences [45].

In addition to the melt pool, other differences can also be pointed out, such as the reduction of the wavy-like texture and the roughness, while the energy power increases, due to the proper melting of the filler material [41].

2.5.2.2 Powder Feed Rate

Powder feed rate is a parameter that, along with scanning speed, determines the amount of raw material in powder form that will incorporate the deposition layer, thereby complementing and counterbalancing the effects of laser power.

It is yet another factor that will have a significant impact on the final product's quality. It can present a variety of challenges during deposition. Feed rates greater than melt rates can result in high roughness and non melted powder, whereas feed rates less than melt rates can result in powder and substrate material vaporization. As a result, a good compromise between laser power and powder feed rate is desired for the production of parts at a faster rate while minimizing defects [46].

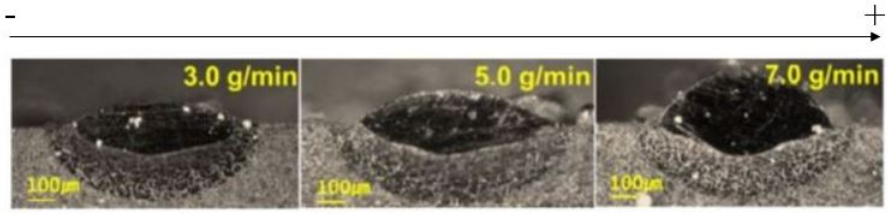

Figure 2.15: Influence of Powder Feed Rate in the melt pool area, adapted from [46].

As the concentration of this element rises, more raw material must be melted, resulting in a higher concentration of energy in the filler material than in the substrate material, which retains less energy absorption, lowering the melting volume of the substrate, as well as the pool dilution level [42].

The powder feed rate has an effect on the other layer dimensions as well. Due to the lower energy absorption with the increase of powder and subsequent melting, the height of the meltpool will also increase (figure 2.15), as will the thickness of the metallic rail, affecting the width of the meltpool as well [47]. The bead grows into a sharper shape as the bond between the substrate and the powder gets reduced, implying a reduction in width [48].

2.5.2.3 Scanning Speed

This component represents the speed at which the deposition head moves relative to the substrate, which has a direct impact on the part's construction rate. In addition, it will be this one that will manipulate the other parameters characteristics locally in the deposition bead.

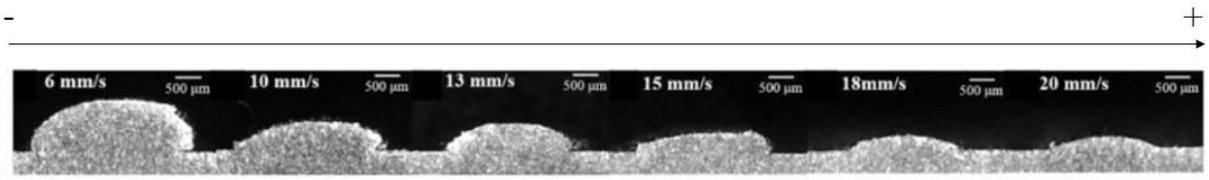

Figure 2.16: Influence of Scanning Speed in the melt pool area, adapted from [50].

If the DED machine moves faster for a given laser power, the concentration of energy absorbed locally at a given point on the metal rail becomes smaller, reducing pool melting time [49]. The same thing happens with the powder feed rate, and as velocity increases, the amount of powder inserted into the meltpool decreases, lowering the material density. This will result in a noticeable decrease in layer height, as well as slight decreases in depth and width, contributing to smaller beads, as shown in figure 2.16 [46, 50].

Slower transit speeds, on the other hand, encourage a more intense contact between the laser and the substrate. It can have the opposite effect, resulting in considerable dilution and evaporation of the material involved, which is not desired by the method [41].

2.5.2.4 Key Formulas

As previously said, throughout this investigation the manufacturing of a component requires the employment of laser power, scanning speed, and powder feed rate. When the study focuses on monitoring each factor alone, evaluating the effects of these parameters between various combinations becomes challenging. As a result, the use of equations involving the relationship between the parameters facilitates, both the analysis of the results and their practical impact on the printed product.

One of the formulations, known as specific energy, takes into account the amount of laser power used, the diameter of the spot, and the scanning speed [51]:

$$E_{specific}[J/\text{mm}^2] = \frac{LP[W]}{\phi[mm] \cdot SS[mm/s]} \tag{2.2}$$

Powder density, also adopted is similar to the previous one, except that the powder feed rate is used instead of the laser power, keeping the other parameters [51]:

$$P_{density}[g/\text{mm}^2] = \frac{FR[g/min]}{\phi[mm] \cdot SS[mm/s]} \tag{2.3}$$

Finally, the specific energy density equation is also used. This formula involves the relation of the laser power and the powder feed rate determined in the parameter selection [52]:

$$SE_{density}[J/g] = \frac{LP[W]}{FR[g/min]} \tag{2.4}$$

2.5.2.5 Tool path strategies

Aside from laser power, scanning speed, and powder feed rate, there are other several aspects that must be considered in order to achieve high-quality deposition. The choice of the print pattern is critical, as with its variation, several aspects are affected by this change, such as the temperature distribution in the material, which can influence the geometry or the presence of defects [53].

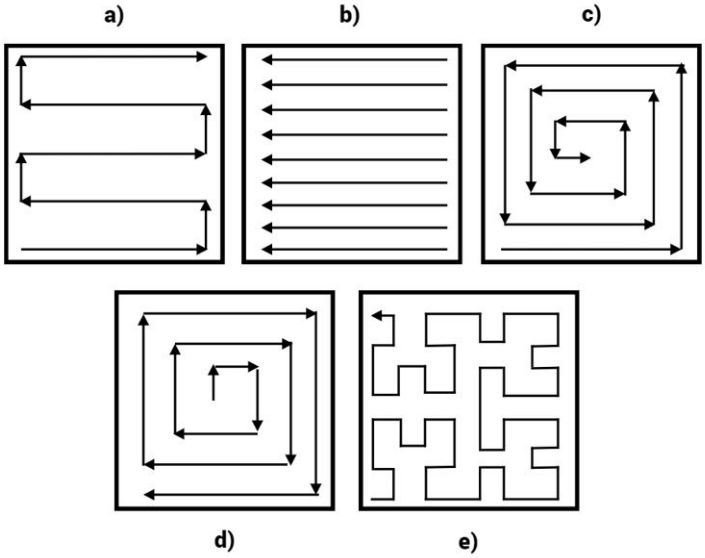

Figure 2.17: a) zig-zag, b) raster, c) offset-in, d) offset-out and e) fractal tool paths, adapted from [53,54].

Raster, offset-in, offset-out and fractal paths are the most common patterns employed [54]. Other trails, such as the zig-zag (identical to the raster but with curved transitions between various lines), still stand out [53]. These patterns are exhibited in figure 2.17.

Printings with raster and zig-zag patterns are more popular in commercial terms, mainly due to a easier implementation and simple algorithms, but at the same time these approaches have dimensional accuracy issues that may restrict their application [55].

In most circumstances, the paths that lead to low temperature gradients produce the best results, [53]. Yu et al. suggested from a comparison of the raster, offset-in, offset-out, and fractal patterns that these last two approaches acquired a better temperature distribution and a better final quality of the part; however, they are difficult to apply and result in an increase in the number of movements without deposition [56, 55].

The use of continuous pathways solves the problem of excessive deposit steps identified by the previously discussed solutions, as well as a reduction in processing time. Ding et al. identified the potential of creating components with continuous closed paths with overlap variation, free of porosities, and requiring few post-machining processes [57].

Wasser et al. explored the design of an algorithm for the manufacture of continuous paths for an arbitrary form, and when the regions to be realized were very large with high accuracy requirements, it resulted in very long production times [58]. In addition, the creation of complicated continuous paths also causes a localized concentration of heat during material deposition, resulting in distortions in the final piece [55].

The usage of hybrid paths shows to be a valuable approach for improving the efficiency of the process, as well as the quality of the product processed by the additive manufacturing process. This approach combines zig-zag and contour patterns in order to maximize part performance and dimensional accuracy [59]. As Jin et al. proposes, the inside of the form to be replicated is manufactured using a zig-zag approach, resulting in rapid production times. Then, it is complemented by the contour technique, which produces the periphery region previously reproduced using zig-zag, enhancing the quality of model's geometrical accuracy [60].

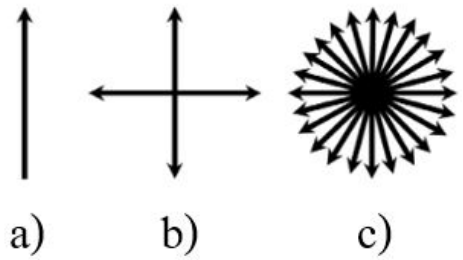

Figure 2.18: Tool path a) 0°, b) 90°, c) 105° rotation angles, adapted from [61].

Some authors additionally emphasize for multiple layers the zig-zag pattern employment with 90° (figure 2.18b) orientation change between segments to reduce the side effects of

high thermal stresses and component deformation caused by deposition orientation, and also increase material isotropy, [59, 54]. Other studies with varying the print direction, specifically with a 105° (figure 2.18c) rotation between consecutive layers, reveal an increase in both horizontal and vertical yield strength to the sample for both this angle and a 90° shift, as compared to printing with no angle change (figure 2.18a) [61].

Table 2.1: Summary of attributes inherent to each scan pattern techniques, adapted from [57].

	Easy Implementation	Geometrical Accuracy	Less Tool-Path Passes
Raster	x		
Zig-Zag	x		
Countour		x	
Continuous			x
Hybrid	x	x	

Any of the strategies outlined above can be employed depending on the final aim, such as dimensional accuracy or manufacturing time, that must be taken into account. The features of each approach are summarized in Table 2.1.

2.5.2.6 Overlapping

The overlap between different lines also needs to be optimized, as it influences the density and consequently the bonding, the mechanical properties as well as the surface roughness [53].

The overlap ratio, that is, the fraction of material of a strand that intersects its antecedent, it can be given by the following expression [62].

$$O_R = \frac{W - Da}{W} \tag{2.5}$$

Where O_R represents the percentage of overlap, W denotes the track width, and Da denotes the distance between adjacent strands, in which the layer geometry is influenced by the variation of this value [63].

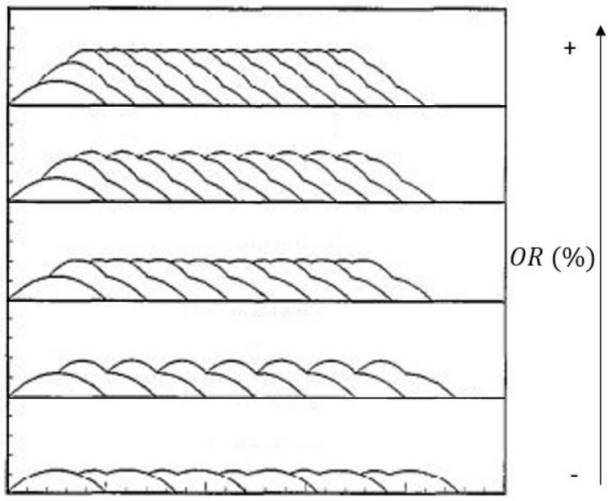

Figure 2.19: Influence of the Overlap Ratio on the bead surface, adapted from [64].

Li et al. studied the influence of overlap on deposition layers theoretically and experimentally concluding that as the percentage of overlap increased, the surface roughness decreased in an oscillatory manner as the figure 2.19 suggests, however when a critical value is reached (too high percentages), due to the stacking of adjacent layers, it would consequently lead to interlayer porosities, and in addition a reduction in scanning speed [64].

Tanigawa et al. also deduced that as the percentage of overlap increased, the surface gained more flatness, with a decrease in Ra values, indicating a decrease in hardness as the percentage of overlap increased, and for high overlap values, the material was as hard as the powder material used in the deposition. Based on the results achieved, it was concluded that both the printed material and the substrate were remelted several times, due to the high overlap, which led to a decrease in this property [63]. According to Zareh et al., the loss in hardness with the overlap augment is also caused by a longer exposure to heat by the neighboring beads, resulting in longer cooling periods [65].

2.6 Metal Matrix Composites

Metallic materials are often molded in bulk form, however, to these it is possible to add other types of materials that, depending on their state, can be in the form of fibers, particles or whiskers. With this combination, metal matrix composites (MMC's) are obtained, which make it possible to improve the qualities and performance of the underlying material [66]. The interest in this kind stems from its functional or structural adaptability, given that traditional materials sometimes struggle to match specific criteria for a certain function.

MMCs allow the base metal to be combined with ceramic or other non-metallic materials, obtaining features dependent on the specific qualities of each material. The ceramics

most commonly used are nitrides, carbides and oxides, given their good strength and stiffness properties, at ambient as well as elevated temperatures [67]. Other kinds of reinforcement, like carbon allotropes, such as graphene, carbon nanotubes (CNTs), and carbon fibers, are also widely used and can come in variety of configurations and morphologies, resulting in outstanding qualities that improve the metallic material [68].

Metal matrix composites can be categorised based on the manufacturing technique used, and can result in ex-situ or in-situ MMCs [69]. Ex situ composites are typically the outcome of traditional manufacturing processes such as powder metallurgy or casting processes including squeeze and rheocasting, in which the reinforcing material is prepared individually before the MMC is created. In contrast with the latter, in-situ composites are formed by chemical reactions between elements or between the material utilized and the compounds involved during the MMC's manufacturing [70].

The use of reinforcements with particle morphology is the most appealing since it generally requires lesser prices and is easier to manufacture. The size of the reinforcement can change, altering the material's characteristics, and it can acquire micro and nano sizes [71].

Composites with micro-sized reinforcements are easier to produce, however for larger particle sizes, the literature points to reductions in ductility and tensile strength [71]. In contrast to micro reinforcements, nano particles tend to improve the strengthening mechanisms of the material, owing to the dislocation effect that will be explained in this subchapter, resulting in a more effective enhancement of the metal matrix material properties when compared to micron particle sizes. One of the issues with manufacturing these composites with this scale reinforcements is the difficulty of utilizing conventional methods, and due to the small size, agglomerations tend to develop and hinder the dispersion of the reinforcement in the matrix [72].

The employment of MMC's opens up a wide variety of options, giving rise to a diverse range of novel materials that can have a significant influence on many industrial domains such as aerospace or automotive, completing design demands [73].

2.6.1 Processing

Metal matrix composites can be manufactured using a variety of available processes. The process selection is determined by the type and amount of reinforcement, the chosen metal, and the purpose of the MMC produced [73].

The processing itself seeks to uniformly introduce the distributed reinforcement into the matrix, [74]. The majority of the techniques used in the industry involve traditional methods, that are the most prominent, and which include casting and powder metallurgy [75].

In general, mixing of the reinforcement over the cast metal matrix is required in casting processes, where it is important that the hard materials have excellent wettability to permit

penetration into the matrix. The most prevalent procedures include the insertion of ceramic fibers into molten metal in the form of porous preforms [76].

This process employs techniques such as direct and indirect squeeze casting. Direct squeeze is used for the creation of composite components with basic geometries, where simple and less expensive moulds are used, whereas indirect squeezing allows for the production of more complex composite elements, where more expensive moulds are used [75].

Other procedures that use liquid metal in a molten state, such as stir casting, can also be used [77]. Powder metallurgy can obtain high composite characteristics, making the technology appealing. Phase control, as well as microstructure refinement and alloy composition control, are all conceivable [74].

An initial mix of metallic and ceramic powder is then compacted to create a green portion, which is typically achieved by cold isostatic pressing (CIP), and following that, the material is put in a vacuum container where it is degassed and sintered to obtain high densification. The material is subsequently extruded or subjected to a hot working process (forging or hot isostatic pressing) to achieve complete densification and the required microstructure that matches the material properties [74].

Materials with metallic coatings where reinforcement is not present should be removed so that it is not present in later stages, which will result in wasted material [74].

2.6.1.1 Fabrication by Additive Manufacturing

In additive manufacturing in order to perform 3D printing, it is first necessary to have the composite powder, to use it as feedstock and then promote its melting and printing in layers. To do so, it is possible to use several types of mixing processes, which include milling processes, more precisely mechanical milling.

The mechanical milling process is a method that can be applied in powder metallurgy and mineral processing industries, where its implementation can be carried out with the objective of partitioning larger materials or mixing different powders [78]. In this process milling balls are used, which are placed together with the powder and then the container undergoes movements of rotation, vibration, horizontal, vertical, and so on, depending on the selected process and the definition of parameters such as the quantity (ball to powder) and size of balls, the time and the rpm desired [79]. Processes such as planetary ball mills, shaken ball mills or vibrating mills can be employed [80]. One of the possible schemes that shows the milling by rotation is demonstrated in the figure 2.20

During the milling process, the clashes caused by the collision of the balls with the powder or the mixture of powders, leads to plastic deformation of the material, which can consequently affect the properties of the material. Therefore, the size of the powder to be treated runs the risk of its particles being reduced, and consequently affecting the particle size distribution [78].

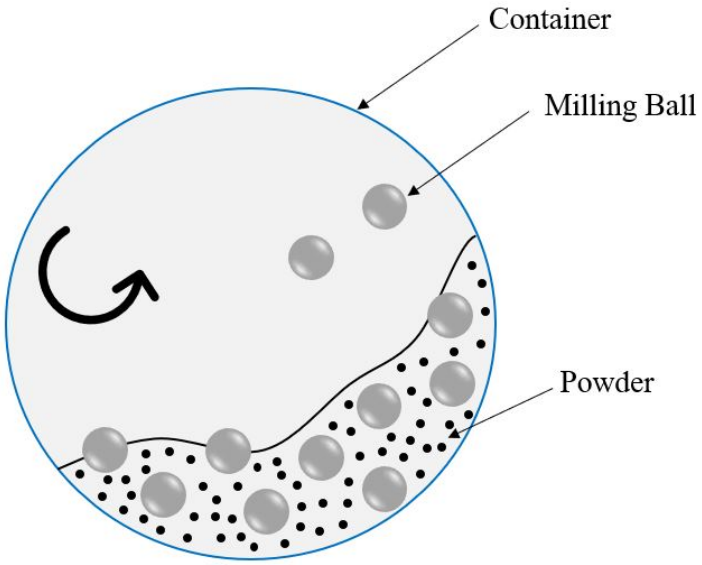

Figure 2.20: Mechanical milling process scheme by rotation, adapted from [79].

The milling process is effective in the treatment of metal powder mixtures in conjunction with ceramic reinforcement, in that it deals with the incorporation of ceramic particles into metallic ones, providing, with the continuation of the method, the fragmentation of the reinforcement into smaller and smaller sizes [78]. As in the case of the plastic deformation previously explained, the attachment of the ceramic reinforcement can propitiate the alteration of the particles and further influence the properties.

With the mixture already conceived, the use of additive manufacturing processes can be used, given the benefits that these techniques have to offer such as design freedom and the production of environmentally friendly products [81]. Processes where powder-based raw material is used, such as SLS, SLM or DED can be used, as they make it possible from a powder-based feed, transform composite powder by melting it to form a piece or constitute functional parts, such as hard coatings.

2.6.2 Strengthening Mechanisms

Different sorts of strengthening processes can be achieved by adding a reinforcement phase to a metallic base matrix, providing the composite with improved capabilities over its original alloy. The material's properties are reflected in the displayed microstructure and internal interfaces, which include both the matrix and the reinforcing phases integrated in it [73].

The methods that allow the composite to acquire hardening qualities in the material are detailed in the following subchapters of this topic.

2.6.2.1 Grain Size Refinement

When it comes to the production and analysis of composites, one of the most widely reported occurrences is grain refinement. Zhang et al. conducted a study on functional gradient titanium matrix composites with TiC reinforcement varying from 0 to 40 vol.% , and discovered that increasing this element boosted both hardness and tensile strength despite a loss in ductility, whereas the partly melted and solidified TiC particles offered microstructure refinement [82].

Other research using nickel matrices support this conclusion. Nguyen et al. created an Inconel 718 composite with the addition of WC particles in which the reinforcement inhibited the columnar development of the matrix grains, resulting in the refinement of this material [83]. Reinforcement particles, which are introduced at the interfaces between the liquid and solid phases, fix the grain boundary while also causing microstructure refinement by inhibiting grain growth. These particles, together with the phases formed by in situ processes, function as nucleation zones, promoting grain refinement [84].

2.6.2.2 Density of Dislocations

The dislocation strengthening mechanism is another documented phenomena. Zheng et al. observed substantial density displacements around the reinforcement particles due to opposite thermal expansion coefficients (TEC) of the TiC particles and the matrix in their investigation of Inconel 625 with and without TiC coating. Lin et al. produced iron composites with the inclusion of nano-TiN, and therefore, noted high density dislocations, providing higher residual stress stability [83].

The thermal expansion in the material is caused by the TEC differences between the reinforcement and the metal. As a result, plastic deformation occurs, resulting in high density displacements surrounding the reinforcing grains, providing greater resistance to deformation and increased material strength [84].

2.6.2.3 Orowan Effects

The hard phase in the metallic matrix increases as reinforcement is introduced. Due to the big resistance particles provide to movement, the dislocation lines which pass over these elements produce loops. This makes it difficult for motions in the matrix to occur, such as the migration of the interface to other locations, increasing the material's and deformation resistance. With the decrease in size and distance between particles, this mechanism becomes more effective, turning the motion impediment greater [84].

2.6.2.4 Load Transferring

The reaction between the matrix and the reinforcement phase at the interface of both constituents is typical in composites and promotes the creation of previously mentioned in situ phases as a result of chemical reactions between earlier ex situ phases. The in situ phases at these boundaries create a far stronger interface bond, which is reflected in the composite's characteristics and, as a consequence, its enhanced strength [85].

2.7 Inconel Matrix Composites Processed by AM methodologies

In the current thesis, several researches were conducted in order to produce metallic composites using an Inconel matrix (those are presented in the Appendix - A). An examination of the data obtained from each research was performed, taking into consideration the alloy utilized, the reinforcement, the particle size, the powder mixing conditions, the proportion of reinforcement added to the metallic powder and the AM process used to perform the deposition. Table 2.2 presents the reinforcements mostly used for reinforcing IN625 and IN718, showing the parameters interested.

Table 2.2: Parameters considered in the present investigation.

Alloy	Reinforcement	Reinforcement Percentage	Powders attributes	Milling Conditions	Deposition Parameters
IN625 IN718	TiC WC	wt.%	Size Shape	Milling Time rpm's	Laser Power Powder Feed Rate Scan Speed

Other reinforcements, such as Al_2O_3, TiB_2, or Gr, were taken into account, as well as other forms of reinforcement percentages, such as vol.%, but due to the lack of publications and data addressing these reinforcement, as well as this sort of measure for IN625 and IN718 alloys, these studys were not considered.

As a result, based on the results obtained in each article regarding the hardness and wear resistance of the composite obtained in each situation, different graphs were made for the Inconel 625 and 718 alloys, as well as, if possible, the increase in percentage of mechanical properties relative to to the values obtained in the original alloy.

Following that, an examination of the particle size of the reinforcement was fulfilled, comparing the performance of particles of micro and nano size from prior research in order to understand its impact on the final product.

2.7.1 Inconel 625 Matrix Composites Analysis

Given the scarcity of wear resistance data, the sole feature examined for analysis in this section was the hardness of the composites. The same colour was assigned to the points corresponding to the same investigation, where the circles and diamonds were the TiC and WC reinforcements applied to the Inconel 625 powders, respectively [86, 87, 88, 89].

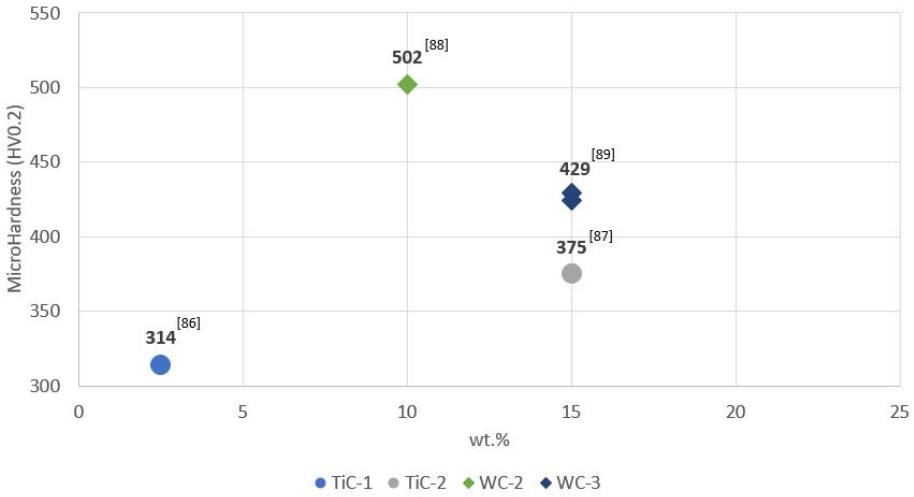

Figure 2.21: Inconel 625 composites microhardness data through the articles analyzed

.

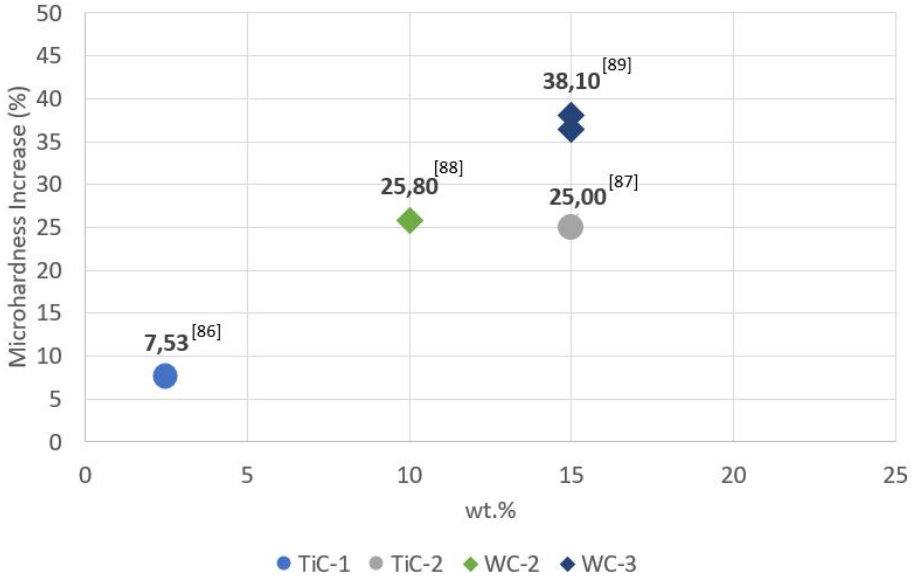

Figure 2.22: Inconel 625 composites micro-Hardness percentage growth data through articles analyzed.

Figure 2.21 shows the microhardness values (HV0.2) for both reinforcements listed at different percentages, however no apparent behavior is discernible. For TiC an increase of 61 HV is denoted when the percentage of reinforcement increases from 2.5 wt.% to 15 wt.%, while for WC, when the percentage increases by 5% (10 to 15 wt.%), a decrease of 72 HV is observed when comparing the two studies.

The impact of adding reinforcement in a metal matrix becomes obvious when comparing the percentage increase in microhardness for the same values compared to the base value of Inconel 625 recorded in each research (figure 2.22). When TiC is considered, the percentage improvement increases significantly from 7.53 to 25% with the increase in reinforcement from 2.5 to 15 wt.%. In the case of WC, from 10 to 15 wt.% also a growth in percentage improvement is observed, although less marked, from 25.8% to 38.1%.

In both cases, the behaviour is the same, showing that as the amount of reinforcement mixed with the alloy increases, the quality of the material properties, more precisely of hardness, acquires greater and greater improvements. It is expected that wt.% higher than those shown in both graphs, that also the action of the reinforcement is increasingly effective, further improving the micro-hardness of the material.

2.7.2 Inconel 718 Matrix Composites Analysis

Figure 2.23 depicts the findings for composites made by an Inconel 718 base alloy, corresponding to the studies conducted for composites formed by WC and TiC [90, 91, 92, 93].

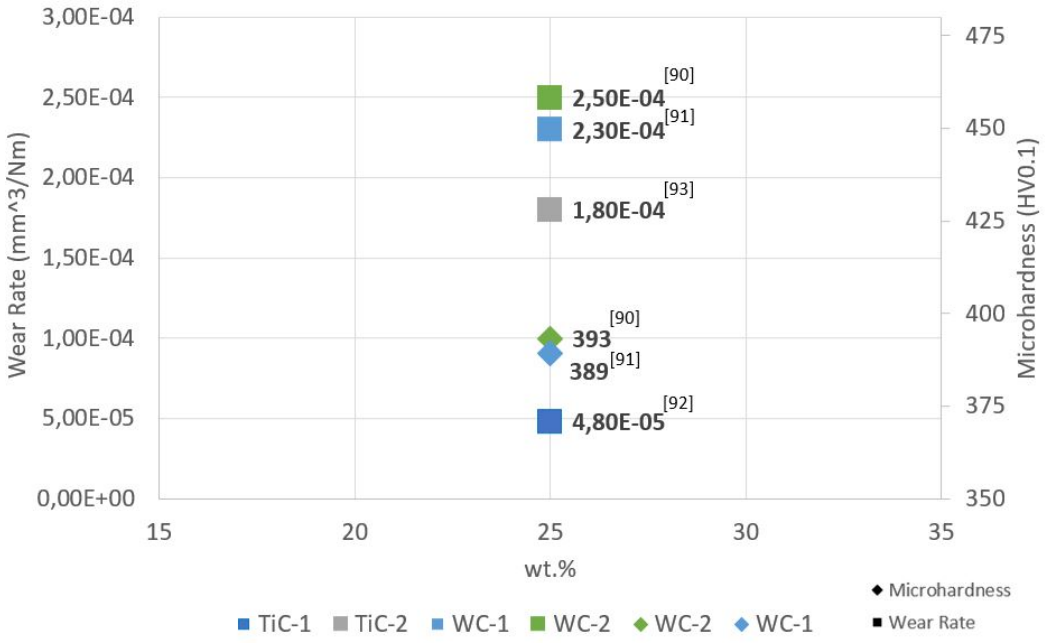

Figure 2.23: Inconel 718 composites microhardness and wear rate data through the articles analyzed.

As in the previous case, each colour represents a research, with the diamonds representing WC, and also the squares signifying wear resistance.

Considering the values of Inconel 718 regarding the final properties of the composite for each case, it was not conceivable to estimate the percentage of improvement for both hardness and wear resistance, since the values of the articles focused on the influence of the deposition parameters of material. For each case the best values were pointed in the figure 2.23.

According to the results obtained by C. Hong et al., the characteristics are successively optimized with increasing laser energy per unit length (LEIPUL), from 80 to 160 kJ/m, reaching values of 4.80×10^{-5} mm^3/Nm and an ever-growing refinement of the matrix [92].

$$LEIPUL[J/\text{mm}] = \frac{LP[W]}{SS[mm/s]} \tag{2.6}$$

Gu et al. discovered that for a given increase in the density of laser energy (J/mm^3), there is an optimization of the values of wear resistance in a first instance (1.80×10^{-4} mm^3/Nm), and that with subsequent increases in the applied laser energy, there is thickening of the reinforcement crystals and a decrease in microstructure uniformity, deteriorating the results obtained [93].

T. Rong et al. investigated the effect of scan speed on the final properties of Inconel 718-WC composites, finding similar results to Gu et al.'s study of the application of laser energy. It was discovered that the values improved up to a certain speed (393 HV and 2.50×10^{-4} mm^3/Nm), however the properties degraded for very fast depositions [90].

This is consistent with the previous research from the DED parameters, since increased connection between the material and the laser, influenced by the parameters previously explored, generates more superior outcomes, but extremely powerful interactions can compromise the final composite.

Despite the fact that most of the values obtained have no reference values, there is a significant difference in the wear resistance results when TiC is used for a 25 wt.%.

Table 2.3: Comparison of parameters related to wear resistance results for 25 wt% TiC.

25 wt%	Particle Size	Milling Conditions	$SE_{density}$ [kJ/g]	Wear Rate [mm^3/Nm]
	IN625 - 15 to 45 µm TiC - 22.5 to 45 µm	Planetary Ball Mill - 200 rpm, 4h	33333	4.80×10^{-5}
	IN625 - 15 to 45 µm TiC - 22.5 to 45 µm	Planetary Ball Mill - 200 rpm, 4h	24750	1.80×10^{-4}

The pre-setting conditions for Inconel 718-TiC material for 25 weight percent reinforcement addition are shown in table 2.3. Both cases have the same particle size and mixing conditions, with the deposition energy of the process being the distinguishing factor.

The observations show that higher laser energy per gram presented for a wear rate of 4.80×10^{-5} mm^3/Nm, leads to better results, implying a greater compromise in the interaction between laser power and powder deposition. In this situation, C. Hong et al. report completely dense coatings with uniformly dispersed reinforcement, the formation of an interfacial layer between the matrix and TiC, and the refinement of the TiC dendrites/particles leading to a higher wear resistance [92].

Gu et al. despite obtaining a lower wear resistance (1.80×10^{-4} mm^3/Nm), also mentioned an interfacial layer which was graded, and several reinforcement phases that improved the wear resistance [93].

2.7.3 Micro vs Nano Reinforcements

The data collected in chapter 2.4.1 for the MMCs composed of Inconel 625 and TiC were used in order to compare the final properties of these micron particle size reinforcements with nano particle size ones [86, 87, 94, 95, 96].

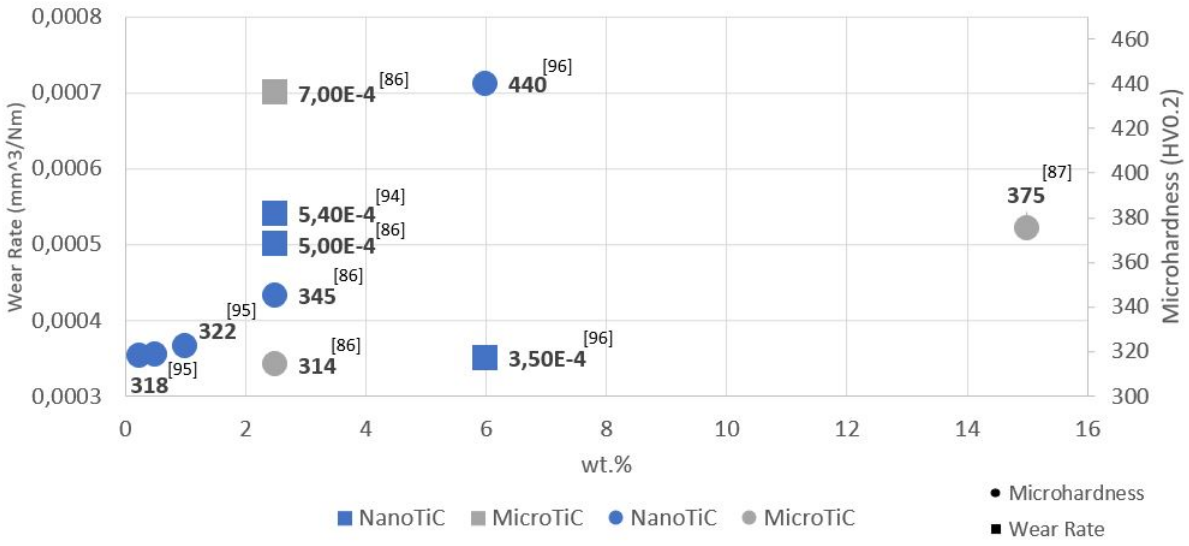

Figure 2.24: Micro and Nano Reinforcements influence on final properties anlysis.

The figure 2.24 displays a direct comparison of microhardness and wear resistance resulting from the two specified reinforcement scales collected from different research for different reinforcement weight percentages. The blue color represents nano scale reinforcements and the gray color micro scale reinforcements, while the circle indicates microhardness values and the square shape wear resistance.

The graph shows that the values offered by nano reinforcements are superior to those of the micro scale, both in hardness and wear resistance, and even for a 0.25 wt.% with

nano reinforcement it produced higher hardness results (318 HV) than for a micro scale reinforcement with 2.5 wt.% (314 HV).

Looking at the figure 2.25, which represents the percentage increase in hardness and reduction in wear resistance, it is clear that the percentages indicated by the nano scale are considerably higher. At 2.5 wt.%, nano-TiC had 2.41 times the hardness of micro-TiC and 1.64 times the wear resistance improvement, and at 6 wt.%, nano-TiC with 1 percent more weight, the microhardness was 1.6 times greater than that of micro-TiC.

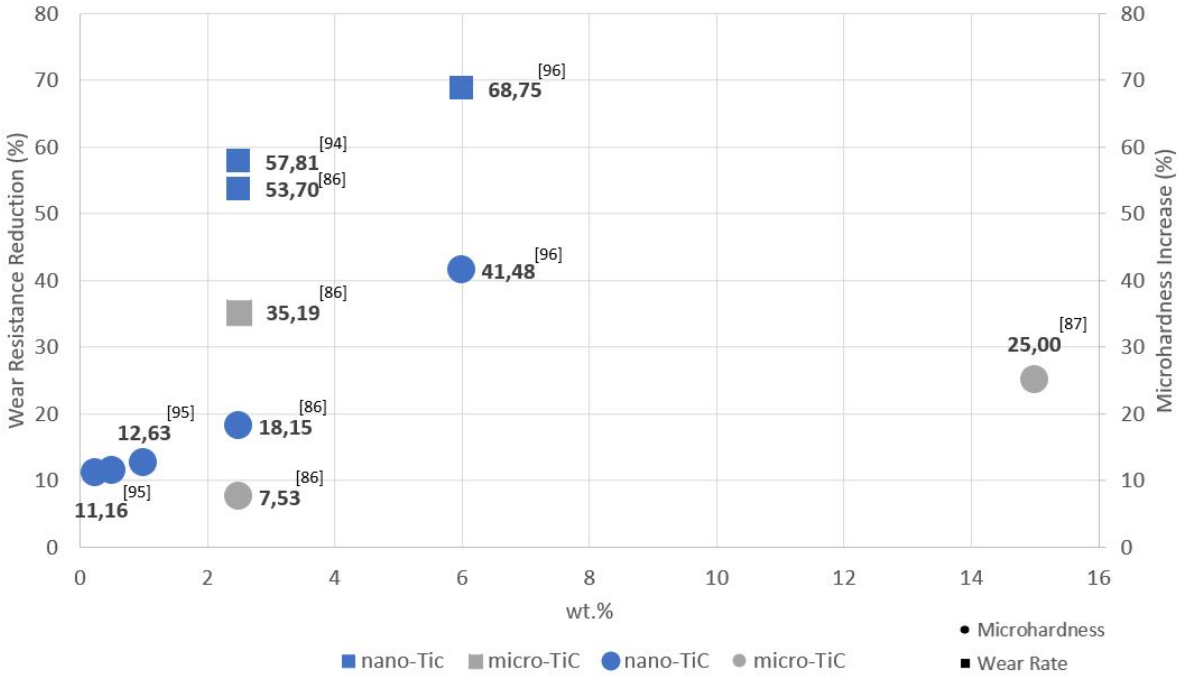

Figure 2.25: Micro and Nano Reinforcements microhardness and wear resistance percentage improvement on the final composites.

According to Gu et al., when nano and micro reinforcements of TiC added to Inconel 625 were examined, nano reinforcements resulted in more refinement of the cellular dendrites with the formation of secondary dendrites, in contrast to micro reinforcements. Furthermore, it stated that the nanoparticles considerably enhanced the microhardness, tensile, and wear characteristics of the composites without affecting their ductility [86].

This can be explained by the fact that for the same weight, the nano scale will contain a greater number of particles since it has smaller particles, making it more efficient if well dispersed, and thus does not require high reinforcement proportions such as microparticles, where a greater presence of reinforcement in composites is more frequent.

Chapter 3

Materials and Methods

3.1 Materials

In this study, different materials were used in order to make the prints by DED-additive manufacturing process. Specifically the alloys of Inconel 625 and Metco 51060A were selected as the feed powder. For IN625, both virgin powder, residue powder and the mixture of the latter with alumina, and additionally Metco 51060A were printed on an AISI 4140 substrate.

In this section, all of the materials involved are investigated, beginning with the chemical composition of the material and progressing through the mechanical properties inherent in each. Furthermore, both applications and typical characteristics of each material are described.

3.1.1 Inconel 625

Inconel 625 is a nickel-based alloy strengthened by the solid solution hardening treatment, niobium and molybdenum in a nickel-chromium matrix, with service temperatures less than 973 K [97, 98]. Due to its inherent benefits, such as resistance to oxidation and corrosion, as well as resilience to high temperatures, the alloy is utilized in a variety of areas such as aerospace, and nuclear [99]. The table 3.1 shows the typical Inconel alloy 625 composition.

Table 3.1: Chemical Composition (%) of Inconel alloy 625, adapted from [100].

	C	Mn	Si	P	S	Cr	Mo	Nb	Co	Ti	Al	Fe	Ni
min						20.00	8.00	3.15					
max	0.10	0.50	0.50	0.015	0.015	23.00	10.00	4.15	1.00	0.40	0.40	5.00	Bal

It is composed by a face-centered cubic crystal that can contain carbides, such as MC and M_6C, which are rich in niobium, molybdenum, and carbon, and when placed at low temperatures also contains $M_{23}C_6$ [100].

The mechanical properties of the material vary depending on the state the material is in. For the different forms and conditions the attributes of Inconel 625 alloy can be seen in the table 2.4.

Table 3.2: Nominal Room-Temperature Mechanical Properties of Inconel alloy 625, adapted from [100].

	Tensile Strength [MPa]	Yield Strength with 0.2% Offset [MPa]	Elongation [%]	Hardness [HV]
Rod, Bar, Plate As-Rolled	827-1103	414-758	30-60	178-247

When mechanical characteristics are deposited using AM technologies, they can vary based on the printing settings selected. G.P. Dinda et al. used the DED process to create samples of Inconel 625, reaching microhardness values of 254 ± 6 HV [97]. A. Gamon et al. reported microhardness values ranging from 223 ± 9 to 263 ± 7 HV for various laser power levels [101].

3.1.2 Alumina

Alumina is an easy to process ceramic material, with the use of the bayer process, by bauxite refinement [102]. A wide range of useful qualities can be appointed, including electrical insulation, fairly high thermal conductivity, high chemical stability and resistance to abrasion and high temperatures. Al_2O_3 is one of the most prevalent compounds in the earth's crust, with great hardness and outstanding wear resistance at a moderate price ranging from 16.3 to 24.5 Eur/kg, making it a sustainable material. It may be utilized for a variety of applications, including electrical insulators, heating constituents, thermal barrier cladding's, and so on [103].

Table 3.3: Alumina Mechanical Properties, adapted from [104].

	Density [g/cm^3]	Compressive Strength [MPa]	Hardness [kg/mm^2]	K_{IC} [MPa$\cdot\ m^{1/2}$]
94% Al_2O_3	3.69	2100	1175	3.5
96% Al_2O_3	3.72	2100	1100	3.5
99.5% Al_2O_3	3.89	2600	1440	4

According to Accuratus, the properties for 3 different percentages of alumina are shown in table 3.3, and are described by the supplier, as a typically hard and wear resistant material, as well as high strength and rigidity [104].

This reinforcement was chosen to be mixed with the IN625 metal powder, given the good stability of the ceramic and due to the low probability of reacting with the matrix, being expected that the chemical/corrosion resistance is not compromised. Other reinforcements having as base carbides, such as TiC, WC or SiC, tend to react with the matrix from in-situ reactions, and consequently influence the material properties.

3.1.3 Metco 51060A

Figure 3.1 illustrates the Metco 51060A powder particles through SEM electron backscattered image mode. It is seen that the powder is composed of two main constituents such

as Inconel alloy and WC respectively in grey and white particles. Moreover there are fine particles as WC dispersed on the surface of Inconel powders as seen in figure 3.1b. However, it seems that this powder feedstock does not correspond with the information provided by the supplier, that is 60% WC.

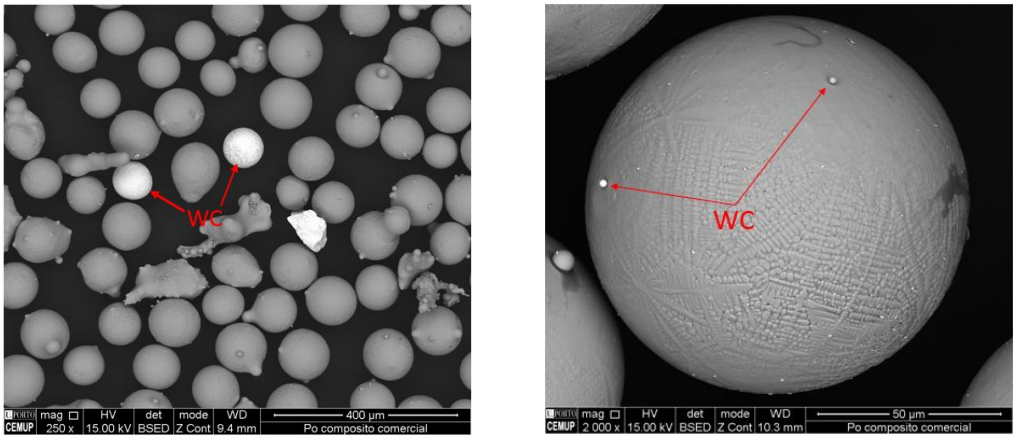

(a) **(b)**

Figure 3.1: Metco 51060A SEM images.

The powder particle size has a maximum and minimal range of 106 and 45 µm, respectively, with an apparent density of 6 to 8 g/cm^3. In terms of microhardness, the material can achieve values ranging from 2700 to 3100 HV0.1 (the powder data sheet is displayed in Appendix - B, where its chemical composition can also be found).

3.1.4 AISI 4140

AISI 4140 alloy steel is a chromium, molybdenum, and manganese alloy steel applied for component materials as for example shafts or gears [105]. Mechanically,it is a steel that in general has a great abrasion resistance, as well as impact and fatigue strength [106]. Table 3.4 describes the alloy nominal composition.

Table 3.4: Chemical Composition (%) of AISI 4140, adapted from [106].

	Cr	Mn	C	Si	Mo	S	P	Fe
min	0.80	0.75	0.38	0.15	0.15			
max	1.10	1.00	0.43	0.30	0.25	0.04	0.035	Bal

Regarding its mechanical properties, table 3.5 shows these characteristics.

Table 3.5: AISI 4140 mechanical Properties, adapted from [106].

	Tensile Strength [Mpa]	Yield Strength [MPa]	Elongation [%]	Hardness [HV]
AISI 4140	655	415	25.70	207

3.1.5 Powder Preparation

In the first step, the residue Inconel 625 powder was mixed with 10% alumina (10 µm average particle size). Materials were placed in a container having milling balls with an average diameter of 3.43 mm and a ball to powder ratio of 2:1, as well as 1/3 of free height left inside the container to enable mixing.

To enable the mixing of powders, repeated batches of 171.92 g and 19.10 g of scrap Inconel 625 and Alumina, respectively, were mixed in the ball mill shaking process (figure 3.2a) and subsequently sieved to remove the mixing balls from the combined powder and thus allow new mixing cycles. The powders were mixed for 3 hours at first, subsequently another 6 hours were added, making a total of 9 hours mixing.

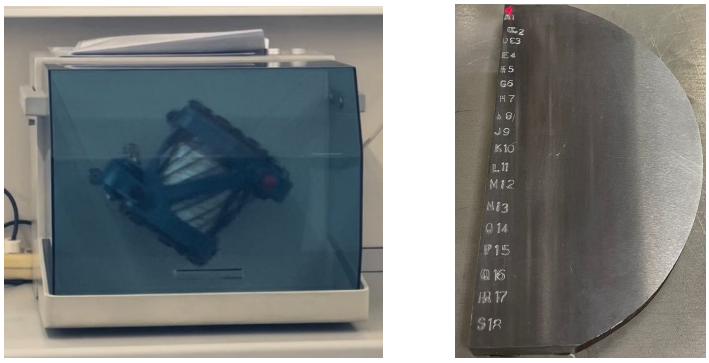

(a) **(b)**

Figure 3.2: a) Ball mill shaking process, and b) AISI 4140 substrate.

The AISI 4140 metal shown in figure 3.2 (b) as previously mentioned, was employed as the substrate for the additive manufacturing process of the composite powder via DED. The substrate faces were rectified with parallelism between both major faces to avoid influencing the material impression, resulting in a thickness of 13.5 mm.

3.2 Methodology Analysis

After the characterization of the material involved, this subchapter discusses the techniques used throughout the study. Methodologies for characterization of flowability of the powder involved are addressed, as well as the machine definitions and parameterizations defined for all powders involved.

Following the manufacturing of the material under investigation, the processing techniques used to gather all the necessary samples are detailed, along with the methodology involved in the material's assessment, such as microscopy and hardness tests.

3.2.1 Flowability Test

Appropriate tests were conducted to evaluate the flowability of the Inconel 625 powder and the composite powder resulting from the mixture. Before beginning the experiments, both powders were dried at 100 °C for 1 h to remove humidity, that would affect the flow rate.

Figure 3.3: ASTM B213-97 flow test setup.

.

Two standard tests, ASTM B213-97 and ASTM B964-09, were employed for this purpose [107, 108]. Both tests allow the flow rate to be determined using a hall flowmeter funnel for metallic powders or powder mixtures. The B213-97 test is appropriate for powders that do not need any assistance to flow through the funnel. For powders that do not show flowability in the first test, B964-09 is used.

For ASTM B213-97, a 2.54 mm diameter funnel and a fixture to hold the funnel, set down without vibration to not influence the powder flow, were used to simulate the test (figure 3.3). 50 g of powder were inserted into the funnel and, after fully placed, were poured into a container.

The ASTM B964-09 standard was performed under the identical conditions as the preceding one, with the exception of a funnel with a diameter of 5.08 mm and a powder mass of 150 g, adapted for powders with lower flow properties.

The flowability of the material is determined by the time it takes for the powder placed into the funnel to exit through its orifice. Powders with a low departure time have higher fluidity, whereas powders with a longer exit time have greater resistance to flowing.

3.2.2 DED Machine Configuration

The DED depositions were conducted by using a Coherent Highlight FL3000 (Coherent, Santa Clara, CA, USA) fiber laser with a maximum power of 3000 W in continuous wave (CW) mode, while to adjust the position of the laser, a Kuka 6 axis industrial robot (KUKA, Augsburg, Germany) was used in the process.

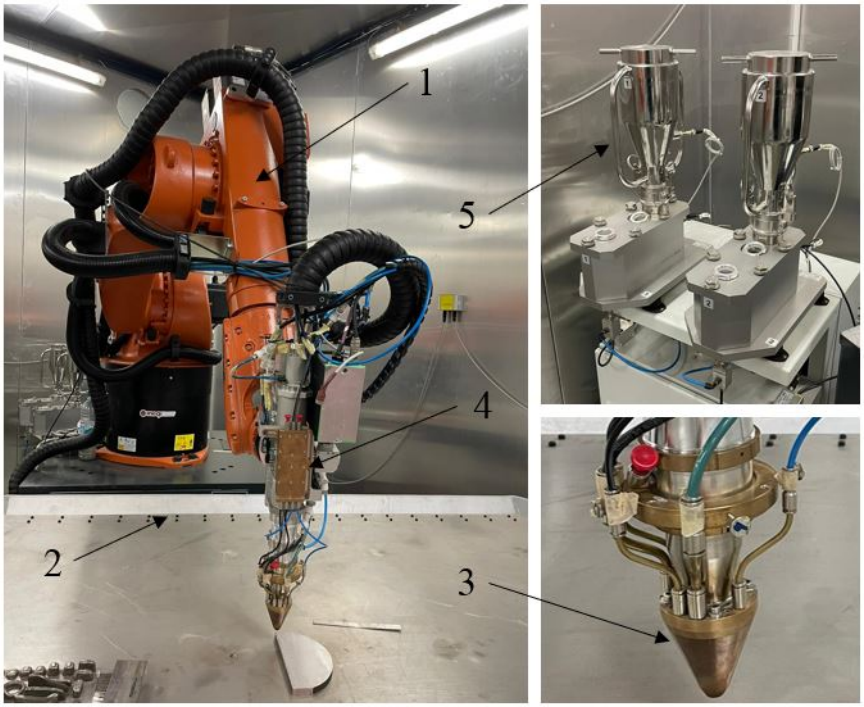

Figure 3.4: Industrial Robot (1) carrying both the head nozzle (3) and the powder splitter (4), as well as the two powder feeders (5), and the welding table (2) below the machine arm.

The robot contains a COAX12V6 nozzle head (Fraunhoffer IWS, Dresden, Germany), with a cooling capacity of 6000 W in continuous operation, connected to a Fraunhoffer IWS powder splitter that allows the separation of the powder material in 4 different channels. To promote a protective atmosphere for the deposited material, an inert gas supply to the system is used, more specifically Argon.

Two Medicoat AG Disk powder feeders (Magenwil, Switzerland) ensure the powder supply, which functions without pulsation from 0.5 g/min to 100 g/min, and can be used individually or combined to generate more complicated materials such as fuctionally graded materials. During the process, substrates are inserted into a DEMMLER 3D welding table (Memmingen, Germany) equipped with eight electrical resistance heating cells, susceptible of accomplishing 600 °C. Some of the components can be seen in the figure 3.4.

3.2.3 Process Parametrization

The procedure of printing parameters development consists of a series of distinct steps until the optimum conditions are determined. Figure 3.5 depicts the same stages.

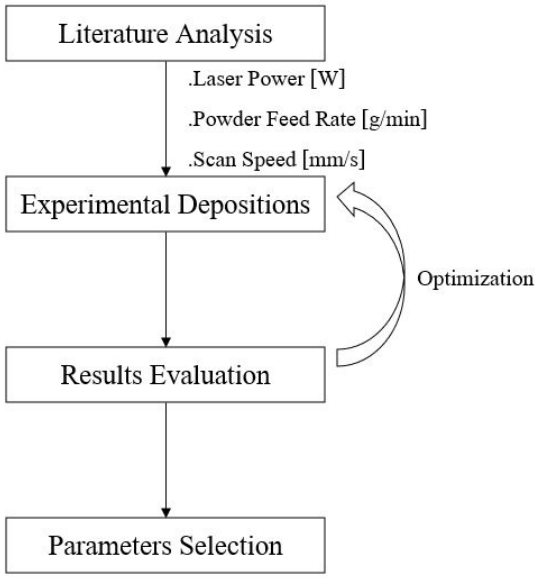

Figure 3.5: Process parameters definition.

Firstly, data reported and experimentally tested in the literature is collected in order to provide a foundation for trialling. With a predefined set of values for laser power, scanning speed, and powder feed rate, as well as other secondary parameters intrinsic to the DED machine, numerous tracks are printed, followed by visual and microscopic inspection.

After determining whether any of the lines have acceptable attributes, the material is deposited in the form of planes. If the criteria are still not fulfilled, the prints are reprinted for optimization and the procedure is continued until acceptable printing characteristics are achieved.

This procedure will be investigated further as this section progresses for residue Inconel 625, Inconel 625-10 wt.% Alumina, and Metco 51060A powders.

3.2.3.1 Inconel 625 Residue Powder

The material deposition conditions were parameterized once the composite powder was created. The Inconel 625 was first utilized to test the arbitrated parameters given in the table 3.6 and thus obtain the optimal material printing conditions.

Table 3.6: Parametrization performed for reused Inconel 625 lines printing.

Line	Laser Power [W]	Scanning Speed [mm/s]	Powder Feed Rate [g/min]	$E_{specific}$ [J/mm^2]	$P_{density}$ [g/mm^2]	$SE_{density}$ [kJ/g]
1	1100	7	4	104.76	0.64×10^{-2}	16.5
2	1200	6	10	133.33	1.85×10^{-2}	7.2
3	1200	10	15	80.00	1.67×10^{-2}	4.8
4	1200	15	20	53.33	1.48×10^{-2}	3.6
5	1500	6	15	166.67	2.78×10^{-2}	6
6	1500	10	20	100.00	2.22×10^{-2}	4.5
7	1500	15	10	66.67	0.74×10^{-2}	9
8	2000	6	20	222.22	3.70×10^{-2}	6
9	2000	10	10	133.33	1.11×10^{-2}	12
10	2000	15	15	88.89	1.11×10^{-2}	8

The first one was adopted due to prior successful printings using this condition at INEGI facility, and the those between 2 and 10 were achieved using the Taguchi L9 method, taking into consideration [109], where an optimised line was obtained for commercial Inconel 625 powder with an $E_{specific}$ of 133.33 J/mm^2. Laser powers of 1200, 1500, and 2000 W, as well as feed rates of 10, 15, and 20 g/min and scan speeds of 6, 10, and 15 mm/s were considered varying the specific energy.

Aside of these parameters, the carrier gas and shielding gas flows were kept constant at 4 L/min and 25 L/min, respectively, as well as the spot size of 1.5 mm and the distance from nozzle to substrate for a 12 mm height. To prevent the machine damage, printed lines with a length of 25 mm were performed with a printing angle of 5°.

The planes are further deposited using parameters equal to the ones used in Inconel 625 powder residue lines, taking into account the most optimal choice between the printed tracks. The prints were created utilizing various tool-path methods and powder quality (residue and virgin). This data is shown in the table 3.7.

Table 3.7: Inconel 625 plane printing conditions.

Plane	Powder State	Dimension [mm]	Pattern	Layers nº	Shielding Gas [L/min]	Overlap [%]
4P1	Used	10x10	Offset-in	1	25	25
4P2	Used	20x20	Offset-in	1	25	25
4P3	Used	20x20	Offset-in	1	25	35
4P4	Used	20x20	Offset-in	1	35	35
4P5	Used	20x20	Zigzag	1	35	40
4P6	Used	20x20	Offset-in	1	35	40
4P7	Used	20x20	Offset-in	3	35	40
4P8	Virgin	20x20	Offset-in	1	35	40
4P9	Virgin	20x20	Offset-in	3	35	40

3.2.3.2 IN625-Alumina Powder

The implementation of the optimal deposition conditions established with the residue powder was maintained for the printing of Inconel 625-10wt.% Alumina powder, but an adjustment of the previously established parameters became required. The table 3.8 shows the resultant circumstances.

Table 3.8: Parametrization performed for Inconel 625-Alumina lines printing

Line	Laser Power [W]	Scan Speed [mm/s]	Valve Opening [%]	Carrier Gas [L/min]
14	600	2.5	5	4
15	600	2.5	10	6
16	600	1.0	10	6
17	600	1.0	15	6
18	300	0.5	15	4
19	200	0.5	15	8
20	200	0.5	30	8
21	300	0.5	50	8
22	350	0.5	100	8
23	450	0.5	100	8
24	400	0.5	100	8

Once the deposition settings were calibrated and the optimal line was acquired, the planes were printed with the tool path varied in the same way that residue powder planes were manufactured. The printing specifications are shown in table 3.9.

Table 3.9: Inconel 625-10 wt.% Alumina plane printing conditions.

Plane	Dimension [mm]	Pattern	Layers nº	Shielding Gas [L/min]	Overlap [%]
4P10	20x20	Offset-in	1	8	40
4P11	20x20	Zig-Zag	1	8	40

3.2.3.3 Metco 51060A Powder

The optimum conditions established for the Inconel 625 material are utilized to print a metco 51060A test line entitled as 25, to provide an accurate comparison with the printed powder residue.

With the track already produced, one and three layer plans were created under the same conditions as the line created with the same material. The printing characteristics are shown in the table.

Table 3.10: Metco 51060A plane printing conditions.

Plane	Dimension [mm]	Pattern	Layers nº	Shielding Gas [L/min]	Overlap [%]
4P12	20x20	Raster	1	8	35
4P13	20x20	Raster	3	8	35

3.2.4 Samples Processing

Once depositions were completed, the different printed components were processed for microscopic material examination. The samples underwent through a slicing stage, in which cutting procedures were first applied to the substrate, to reduce its dimensions and ease internal cutting of the printed material. After the substrate's fraction into small segments with a mechanical saw (figure 3.6a), a cutting disk Remet TR 60 machine (figure 3.6b) was employed to achieve precise cuts in the samples cross section.

(a) **(b)**

Figure 3.6: a) Mechanical Saw and b) Remet TR 60 machines.

Following all of the cuts conclusion, the samples were cold mounted, with 100 g of resin and 13 g of curing agent pre-mixed and poured into each one placed in plastic moulds, followed by a one-day curing time to allow the liquid substance to solidify.

The previously cured material was wet sanded using sandpaper of various meshes. The samples traveled through 180, 320, 800, 1200 and 4000 grinding papers in that order, with the rougher ones, specifically the first two, submitted to 300 rpm and the remaining at 150 rpm.

In addition to the sandpapers listed above, cloth polishers with 3 and 1 µm diamond suspension during 30 minutes in each one were employed for samples which require SEM analysis.

Precautions were made during the polishing process when positioning the sample in contact with the discs. The specimens were not rotated continuously, but its position on

each sandpaper rotated 45° twice and/or 180° for bigger and smaller specimens respectively, and 90° when switching discs.

After grinding-polishing, the samples were washed and dried and finally the polished cross section is immersed in a 2% Nital solution to chemically attack the surface, which is then available for microscopic analysis using a Leica DVM6. These processing stages are summarized in the figure 3.7.

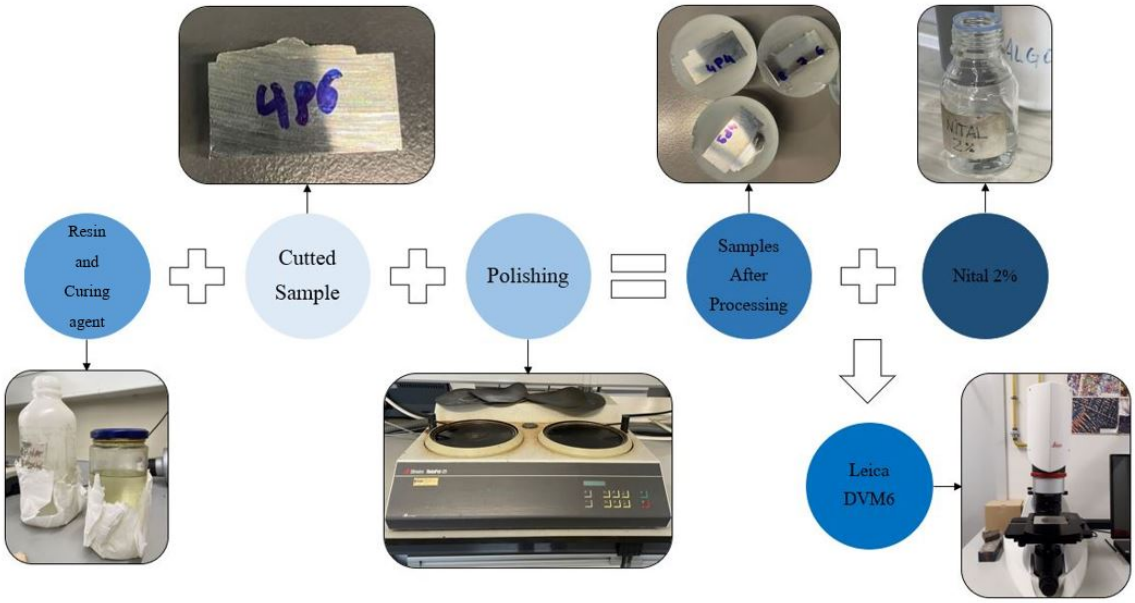

Figure 3.7: Metallography procedure.

3.2.5 Hardness Tests

After treatment and microscopic visualization, the specimens were submitted to hardness measurements. The samples to be analysed in hardness tests were only submitted to these measures after material microscopic observation to not interfere with this analysis.

Figure 3.8: Zwick Roell Emco-Test machine.

Serial hardness measurements were performed on the material using the Zwick Roell Emco Test machine (figure 3.8) provided by the INEGI metallurgical laboratory. The Vickers scale (HV) was used as the measurement unit, and 0.1 HV (100 gf) identations were employed in the test to determine the material's hardness.

3.2.6 Scanning Electron Microscope

The accurate evaluation of the material under examination was possible using the EDS analysis methodology by SEM microscopy, available at CEMUP. The use of SEM was instrumental in supporting microscopic inspection of the printed material, as well as contributing in the assessment of the form and size of both the residue powder and the resultant mixture with alumina.

The EDS was also an important tool to identify the chemical composition of the material, and thus contribute to the analysis and discussion of the microstructures obtained during the work.

Chapter 4

Results and Discussion

4.1 Powder Analysis

After 3 hours of mixing, a visual analysis of the powder showed a lack of homogeneity, so a further 6 hours were applied, making a total of 9 hours. After 9 hours of mixing (figure 4.1), an acceptable distribution of the reinforcement towards the metallic powder was achieved.

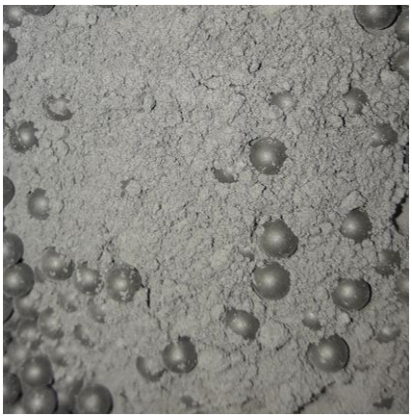

Figure 4.1: Resultant powder + milling balls after 9 hours mixing.

For the evaluation of the influence of the mixing hours and identification of the particle size of the metal powder, samples of Inconel 625 residue and after 3h, and 9h of mixing were analysed through SEM images. Each of the phases can be visualized in figure 4.2.

Figure 4.2 (a), (b), and (c), illustrate approximate diameter measurements corresponding to the particles displayed in the SEM pictures using Image J software in order to determine the particle size distribution of the residue IN625 material, and of the mixtures.

The measurements at each mixing stage indicate a peak for (a) at 70-80 µm and for (b) and (c) at 60-70 µm, with a decreasing frequency of particles above and below these dimensions. This can be attributed to the fact that the measurement of the particles was restricted to a series of SEM photographs, which limited the measurement to a single sample, as well as the preparation method prior to the SEM analysis, whereby the sample was blown to remove impurities which also influenced the amount of particles that were present. Therefore,

by observing the particles depending on the number of hours of mixing applied, there should have been no change in particle size.

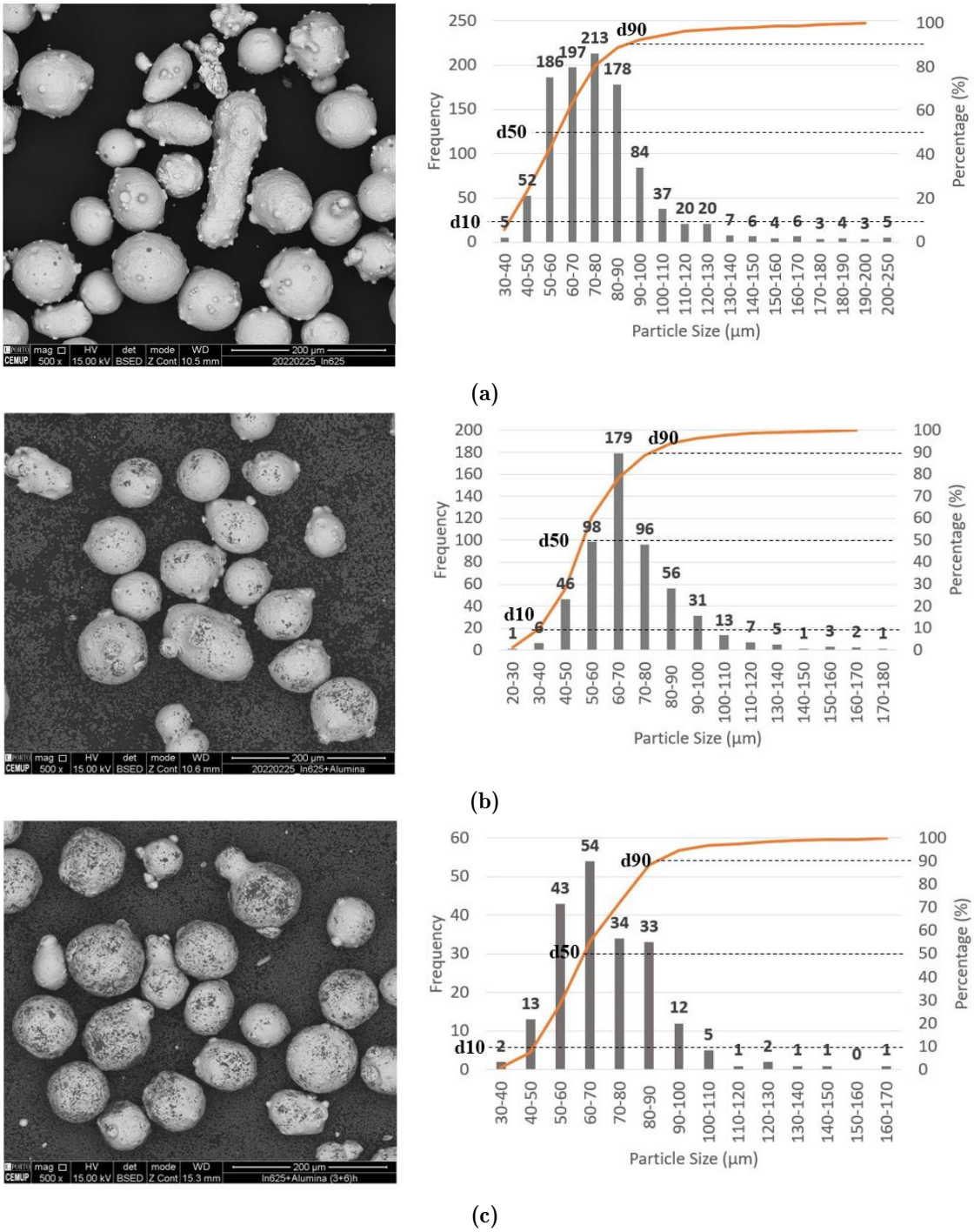

Figure 4.2: SEM images and PSD of a) Inconel 625 powder, b) after 3, and c) 9 hours of milling.

It is also noted that as the number of mixing hours applied to powder increased, so did the adherence of the alumina on the IN625 particles, which is induced by the collision between the powders and the mixing balls.

Based on the graphs in figure 4.2, it was possible to determine the values d10, d50, and d90, as well as the average particle size in each case. Table 4.1 highlights both these values.

Table 4.1: Particle size data acquired for Inconel 625 before and after 3 and 9 h milling, based on image analysis.

	d10 (µm)	*d50* (µm)	*d90* (µm)	Average Particle Size (µm)
IN625 powder	30-40	50-60	80-90	76
IN625-10 wt.%Al_2O_3, 3h milling	30-40	50-60	70-80	69
IN625-10 wt.%Al_2O_3, 9h milling	40-50	60-70	80-90	70

Despite minor differences in the base powder, and after 3 and 9h mixing, no impacts on the particle size of IN625 are apparent. The average particle size, similar to *d10*, *d50*, and *d90*, exhibited minimal variations, supporting the idea of a constant particle size over the mixing cycles.

4.2 Flowability Test

The following flowability findings can be inferred after conducting the ASTM B213-97 standard in table 4.2.

Table 4.2: ASTM B213-97 flowability findings.

	1º Measure [s/50 g]	2º Measure [s/50 g]	3º Measure [s/50 g]	Average [s/50 g]
IN625	10.41	10.43	10.43	10.42
IN625-10 wt.% Al2O3	0	0	0	0

According to the results, the employed Inconel 625 powder had an average flowability of 10.43 s/50 g, but nevertheless the composite powder did not move through the funnel orifice and stayed stationary. To confirm the values obtained, with standard B964-09, from a funnel orifice diameter twice the size of standard B213-97, the flowability test for the composite powder is repeated. The results are shown in table 4.3.

Table 4.3: ASTM B964-97 flowability findings.

	1º Measure [s/150 g]	2º Measure [s/150 g]	3º Measure [s/150 g]	Average [s/150 g]
IN625-10 wt.% Al2O3	0	0	0	0

Similarly the powder remained stationary, although the diameter is larger. This confirms the absence of flowability of the composite material (figure 4.3 a).

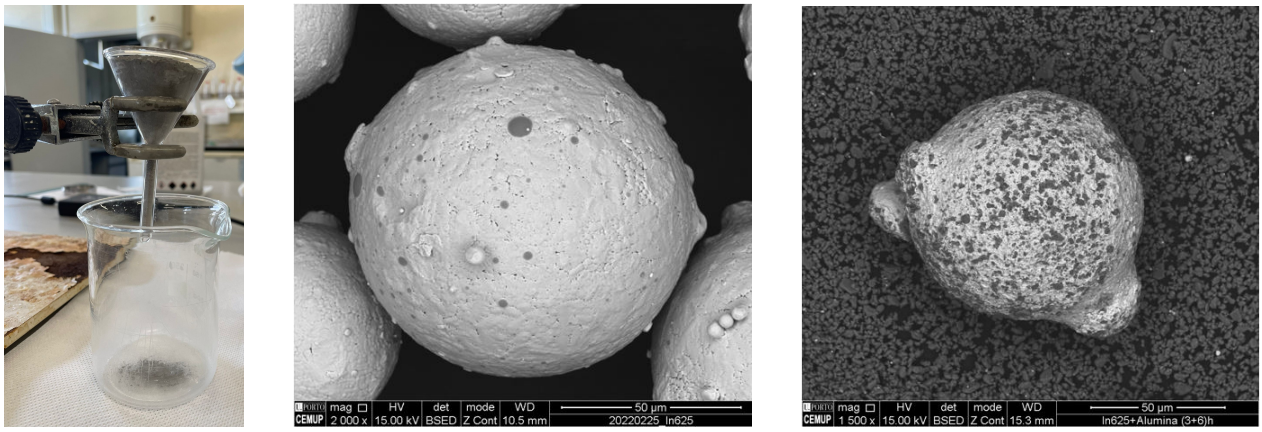

(a) **(b)** **(c)**

Figure 4.3: a) Absence of the mixture powder flowability, and morfologies of b) Inconel 625 residue, and c) mixture powder particles.

The residue Inconel 625 particles (figure 4.3 b) due to the collision energy resulting from the collision of the powder with the milling balls in the mixing process changed their surface roughness through the adhesion of the alumina reinforcement particles (figure 4.3 c). This increase in the roughness of the metallic particles resulting in the elimination of powder flowability

If a different process was applied, in which the alumina was not encouraged to attach to the based powder by the milling balls impacting, the flow rate would likely improve. However, it was supposed that due to the powder carrying capacities of the machine, more precisely of the carrying gas, it would be possible to overcome this short coming.

4.3 Inconel 625 Residue

4.3.1 Parametrization

Based on the parameters shown in table 3.6, 10 different lines were printed by the DED process. Figure 4.4 shows the top view showing the appearance of the printed line, as well as the thickness reporting the bead height.

Due to the time availability, the line conditions were immediately chosen based on the geometry and appearance of the beads produced. To assess the best sample, the following factors were taken into account:

- linearity;
- homogeneity;
- metallic aspect or lack of burning;
- spattering;
- slags, crackings or porosity's;

Visually, none of the lines produced had defects such as porosities or cracks, but the Specific Energy and Powder Density revealed to have an impact on the other elements of analysis.

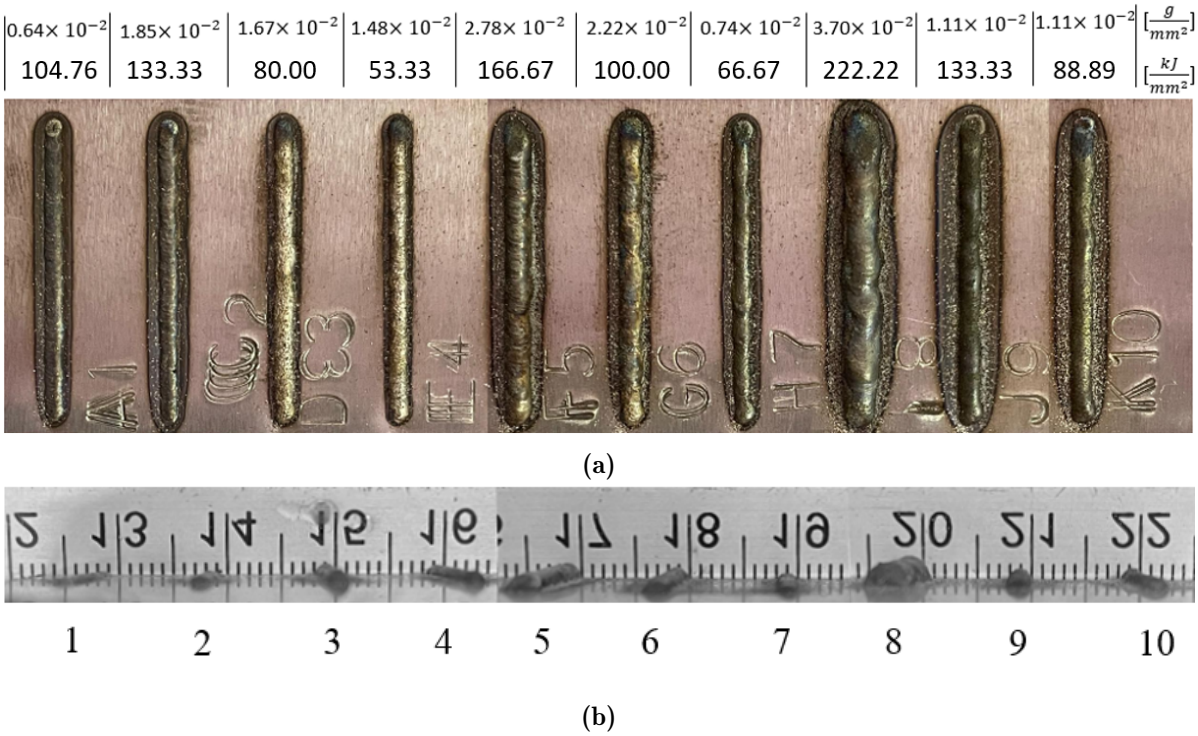

(a)

(b)

Figure 4.4: Top (a) view and (b) thickness of residue IN625 printed lines.

The burned area surrounding the beads was bigger in circumstances when high specific energies were applied, such as lines 5, 8, and 9, and in contrast to the preceding situation where low energies were applied, had substantially smaller burnt areas, as shown by lines 3 and 4.

It is still visible that when the specific energy increases, the linearity of the bead reduces. For line 4 that evidences for a specific energy of 53.33 J/mm^2 great linearity, when the double

of the energy is applied near 100 J/mm^2 it already starts to demonstrate a reduction of the linearity as evidenced by lines 2 and 9, until reaching a maximum of 222.22 J/mm^2 in line 8, where no linearity is really observed.

Variation in printed powder density results in variation in line size. The printed mass per square metre varies from situation to situation, but it can be deduced that for higher order values, such as lines 5, 6, and 8, the line thickness is highly noticeable, in contrast to low density conditions, such as lines 1 and 7, where smaller lines are observed.

In addition higher spattering was denoted as the laser power increased indicating an augment in deposition turbulence, and good overall height uniformity apart from line 9. Few beads had a good metallic appearance, however, 3 and 4 shown good metallic brightness.

Taking into account all of the parameters described and investigated, line 4 was chosen for further plan depositions owing to the consistency displayed in the overall panorama in these aspects.

Following the processing of the cut sections, the visual analysis as well as the geometrical characteristics can be seen in figure 4.5 and table 4.4. Figure 4.5 shows that, in general, the deposited lines do not have internal defects, such as porosities or a lack of fusion, excluding lines 9 and 10. In these two lines, due to the high powers to which the substrate is exposed, the keyhole effect occurs, where a high dilution of the material is verified, and in addition, due to this effect, the appearance of porosities [44]. In line 9 there is also a dark zone which appears to be a crack, but is actually a contamination of the sample. It is also observed that dilution occurred in all samples of the material on the substrate, which was followed by a heat affected zone (HAZ), where these dimensions varied from case to case.

The data presented in the table confirms the previous visual analysis of the samples, in which lower printed powder densities of 0.64×10^{-2} g/mm^2 and 0.74×10^{-2} g/mm^2 for lines 1 and 7 respectively, resulted in smaller bead heights and for these lines whereas higher values were applied more specifically 2.79×10^{-2} and 3.70×10^{-2} g/mm^2 for lines 5 and 8, greater bead heights are reached.

There is no clear correlation between the lines and the modification of the parameters for the width and penetration since these dimensions rely on their proportion to the remaining geometry, therefore the bead area is more appropriate for analysis, than the bead height.

Taking into consideration the bead areas, the dilution of each line can be determined. Lines 1, 2, 7, 9, and 10 have very high percentages of dilution, but lines 3, 4 and 8, despite having values within the limit of what is intended, have lower order values, as seen in the figure 4.5. The amount of energy used has a significant influence on the dilution of the material. When analyzing the energy per gram of powder deposited, it is seen that as the energy increases, so do the percentages of dilution. For the lines with higher dilution, percentages exceeding 50% were recorded, with maximum values obtained for 1 and 9, when bigger specific energy densities of 16.5 and 12 kJ/g are also used.

For lower specific energy densities is denoted in agreement with the previous situation lower dilutions, as reported in 3 and 4, where 4.8 and 3.6 kJ/g are used. It should also be

noted that for lines 5 and 8, that despite giving different dimensions, both present similar dilution for the same specific energy density of 6 kJ/g.

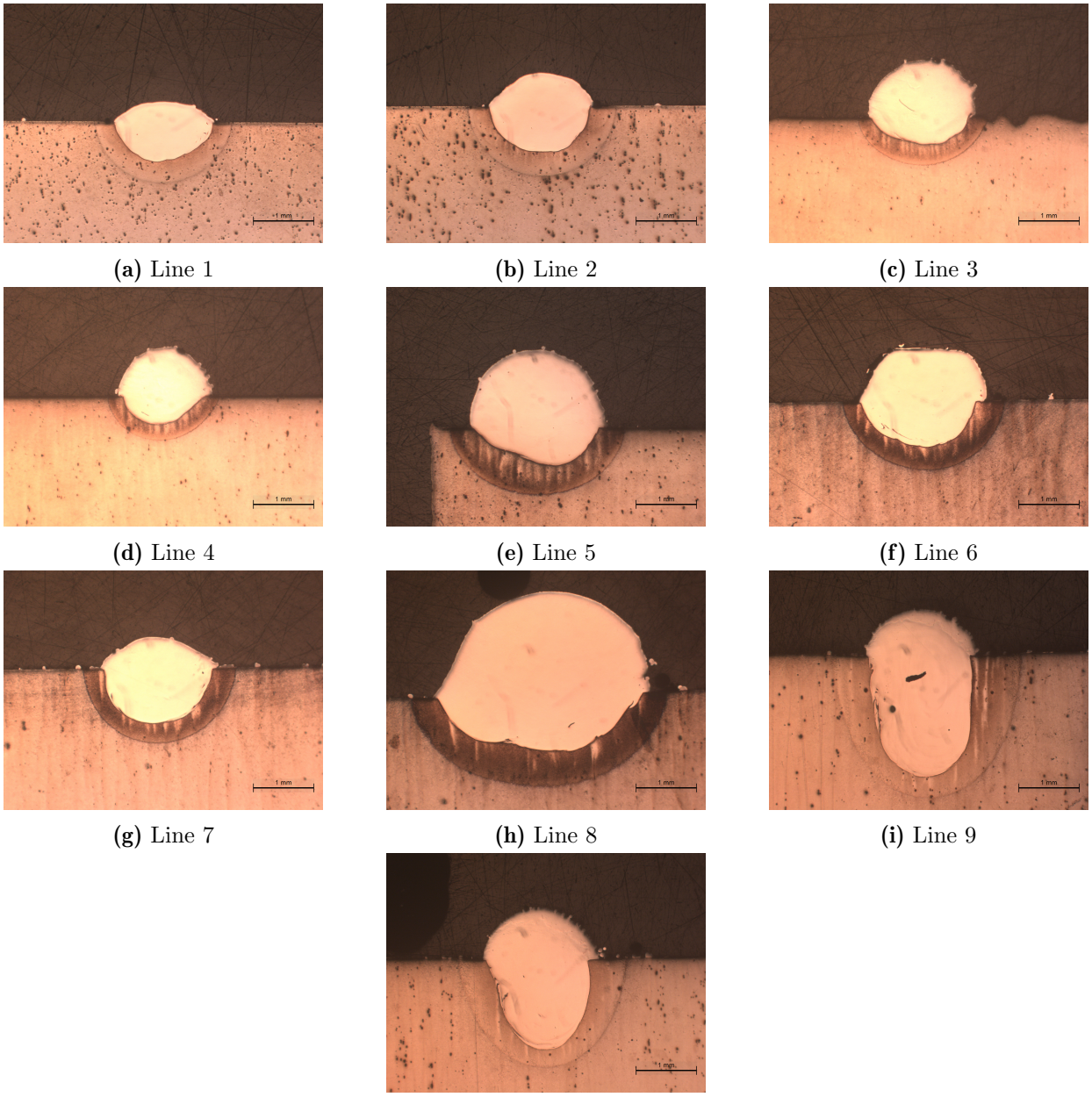

(a) Line 1 **(b)** Line 2 **(c)** Line 3

(d) Line 4 **(e)** Line 5 **(f)** Line 6

(g) Line 7 **(h)** Line 8 **(i)** Line 9

(j) Line 10

Figure 4.5: Used Inconel 625 lines cross section.

Table 4.4: Inconel 625 printed lines geometrical characteristics.

Line	H [mm]	W [mm]	D [mm]	Ad [mm^2]	As [mm^2]	Dilution [%]	Left Wetting Angle [°]	Right Wetting Angle [°]	HAZ [mm^2]	$SE_{density}$ [kJ/g]
1	0.357	1.648	0.661	0.416	0.853	67.22	52.39	49.17	0.981	16.5
2	0.557	1.797	0.774	0.739	1.019	57.96	53.21	63.16	1.229	7.2
3	0.987	1.773	0.468	1.392	0.489	26.00	122.42	98.46	0.735	4.8
4	0.813	1.650	0.466	1.043	0.497	32.27	59.04	69.12	0.815	3.6
5	1.301	2.388	0.576	2.394	1.177	32.96	78.83	60.82	1.086	6.0
6	1.037	2.376	0.691	1.698	1.063	38.50	49.28	54.45	1.400	4.5
7	0.536	1.992	0.921	0.740	1.355	64.68	89.78	87.04	1.087	9.0
8	1.704	3.769	0.934	4.848	2.339	32.54	47.69	63.71	2.928	6.0
9	0.787	2.254	2.030	1.179	3.139	72.70	75.43	83.89	2.628	12.0
10	0.869	1.944	1.435	1.265	2.007	61.34	105.62	69.86	1.979	8.0

Line 3 is from the parametrization considered that has an acceptable dilution, while tracks 4, 5, and 8 can also be considered with an optimization of the printing conditions to decrease the dilution.

In terms of wettability, the angles exhibited in most circumstances when compared the left and right angles of the track itself, show only minor differences. This discrepancy is more noticeable in sample 10, indicating a larger buildup of material on the left side of the bead.

Line 3 stands out among the lines since the angles are quite high, which is undesirable since it might compromise material deposition also revealing a large discrepancy between the left and right angles.

HAZs of 0.981, 1.229, and 0.735 mm^2 were observed for tracks 1, 2, and 3, and these values grew until reach beads 8, 9, and 10, when the HAZ was 2.928, 2.628, and 1.979 mm^2. A tendency is recognized in the heat affected zone of the observed thermally impacted regions. Higher laser energies are employed in samples with greater areas, whereas lower deposition energies are used in samples with smaller areas.

As previously said, very high HAZ must be prevented since they structurally alter the microstructure and hence weaken it. Thus, the most impacted lines must be avoided.

As a result of analyzing the various characteristics, it is deduced that the most suited lines in a first phase at a visual level are lines 3 and 4, owing to their metallic look and linearity. Nevertheless, when analyzed at the microscopic level, the dilutions 3, 4, 5, and 8 are the ones that come closest to a more acceptable percentage of dilution.

In terms of macroscopic examination, lines 8 and 5 exhibit poor linearity and metallic aspect, avoiding what happened in lines 3 and 4, and also exhibit greater heated affected zone. Lines 3 and 4 both show good aesthetic aspects, with the exception that the wettability angle of the first one has to be optimized since it does not meet the requirements.

4.3.2 Plane Printing

4.3.2.1 Samples Evaluation

As reported in section 4.2, planes were printed with identical parametrization circumstances to sample 4 described in table 3.6. In a first instance, the reused Inconel 625 powder was printed with the specifications stated in table 3.7.

A plane of dimensions 10x10 mm (4P1) with offset-in pattern and 25% overlap was first built, but the dimensions were insufficient, thus they were enlarged to 20x20 mm. The distortion of the deposited material did not occur as expected when the printing area was increased, but the indicated overlap proved insufficient since there was no apparent intersection between beads in 4P2.

To address this issue, the overlap was increased to 35% in 4P3, which apparently improved the overlap of neighboring lines. Nevertheless, the plane's surface displayed oxidation, therefore the amount of shielding gas increased to 35 L/min in 4P4, and despite having a superior metallic appearance regarding the previous situation, the sample continued to exhibit oxidation. Line 4-2 was printed with similar settings as line 4 but with this difference in shielding gas to understand the impact of this alteration.

With an 40% overlap in 4P5 and 4P6, for a zigzag and offset-in pattern respectively, the first presented higher surface oxidation and lesser metallic appearance, while 4P6 showed larger distortion in the plane's center. Because of the superior surface aspect, a 3-layer plane with the same characteristics as 4P6 was printed in 4P7, continuing to display oxidation and increasing distortion as the material approaches the sample's center. The above-mentioned samples can be seen in figure 4.6

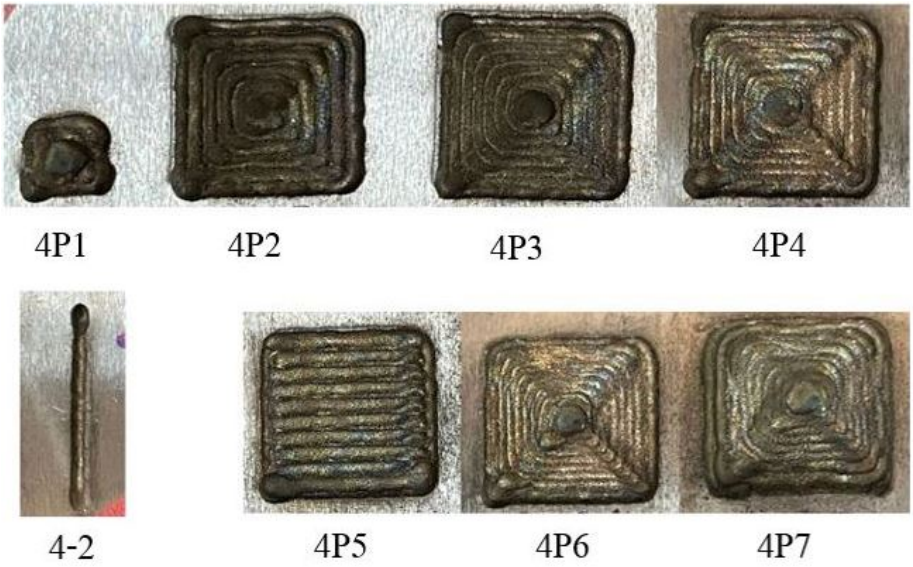

Figure 4.6: Residue IN625 printed planes.

The presence of oxidation of the material was a common complaint in all of the printed plans, and it was unclear if the state of the material had an impact on this phenomena or whether it was due to a lack of optimization of the printing settings.

Figure 4.7: Virgin IN625 printed planes.

With the deposition of, a virgin IN625 alloy, as 4P8 and 4P9 shown in figure 4.7, it was inferred that the material had no effect on this defect. These virgin powder samples were visually identical to those of used powder, which consequently attributes this problem to the lack of optimization of the conditions of the unit responsible for the depositions. Significant quantities of shielding gas proved ineffective in oxidation reduction, and they also resulted in a high consumption of the resource, which raised expenses, necessitating a reduction in the amounts used in subsequent prints.

The characteristics identified in the visual inspection of the deposited planes can be noticed through microscopic investigation.

The plane 4P2's cross section (figure 4.8a) does not show any fractures or porosities, but it does show a lack of fusion between lines. Regardless, the overlap is insufficient since there is a lack of fusion at the interface between the printed lines and the substrate, as well as the layer's excessive surface roughness.

The absence of fusion which had existed earlier owing to the low overlap and high roughness was solved by increasing the overlap at 4P3 (figure 4.8b). Despite the correction of these issues, there is a slight drop in material dilution and also the existence of some regions where lack of fusion can be observed.

The biggest observable difference in the dilution, is the depth reached by the printed material in the centre of the substrate in 4P2, contrary to what is seen in 4P3. In addition, penetration generally in 4P2 acquires larger dimensions than those shown in 4P3, which reduce with the increase in overlap. Despite the reduction in dilution, the frequency of the lack of fusion in 4P2 the cut section is reduced when compared to 4P3, just like the size of these elements.

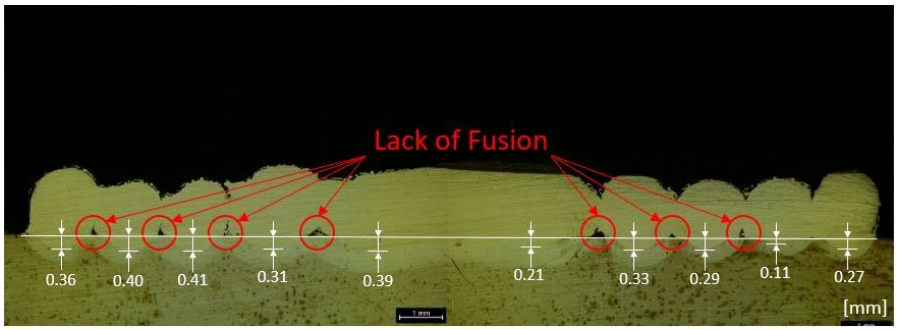

(a)

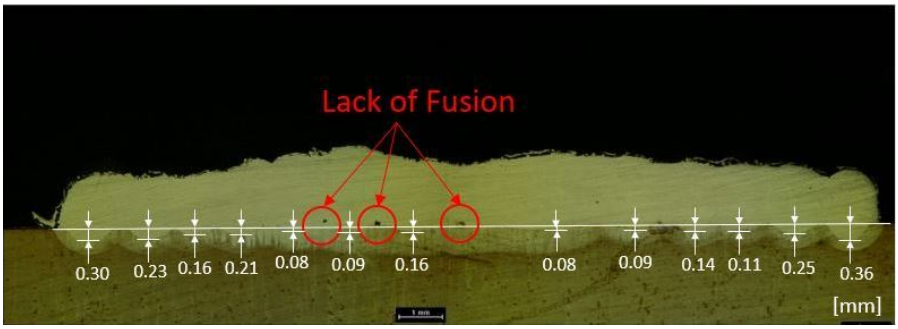

(b)

Figure 4.8: a) 4P2 and b) 4P3 cross sections.

With increased shielding gas for the same parameters applied, there is a big difference with regarding the original track as seen both in figure 4.9 and in table 4.5. In terms of dimensions, the bead height grew considerably while the width and depth decreased.

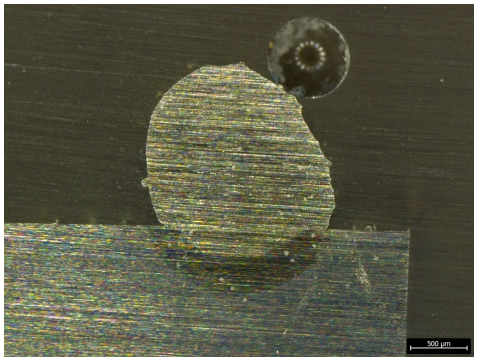

Figure 4.9: Line 4-2 cross section.

Table 4.5: Line 4-2 geometrical characteristics.

Line	H [mm]	W [mm]	D [mm]	Ad [mm^2]	As [mm^2]	Dilution [%]	left wetting angle [°]	right wetting angle [°]	HAZ [mm^2]
4-2	1.435	1.427	0.247	2.04	0.20	8.81	144.43	96.76	0.55

This change in bead size also resulted in a abrupt reduction in dilution from 32.27 to 8.81%, where deposition turbulence produced by higher shielding gas must have played a significant role. It is still observed a high angle of wettability on both sides of the line, with a significant difference between them, indicating a preferential deposition of additive material on the left side of the cord. The increase in turbulence, combined with the machine's deposition angle of 5°, must have favored this phenomenon.

Due to the poor penetration, the material's HAZ area was similarly substantially less. As a result, these modifications would have an effect on the geometry of the planes with a shielding gas flow rate of 35 L/min.

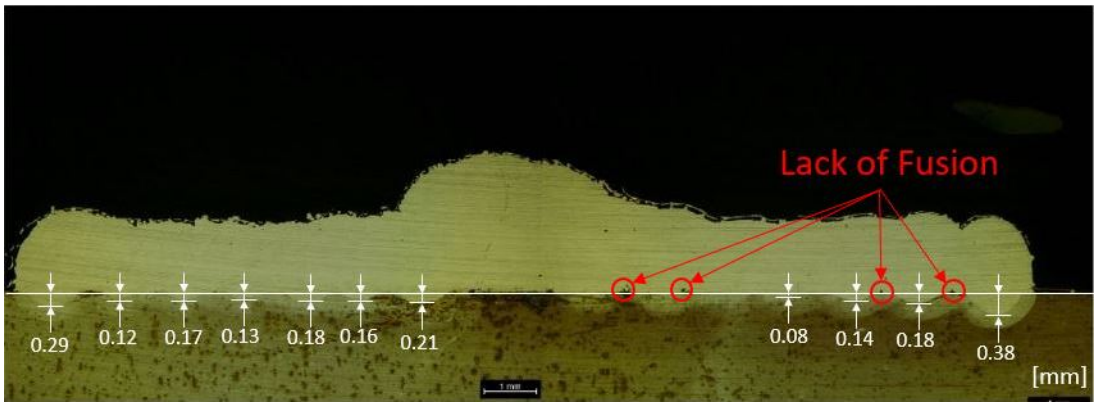

Figure 4.10: 4P4 cross section.

The effect of these changes in plane geometry is represented in 4P4 (figure 4.10) already with the shielding gas of track 4-2 applied. When comparing the planes 4P3 and 4p4 in a first phase it is denoted that there is a decrease of the penetration into the substrate, with this effect being more noticeable in the beads printed on the periphery of the samples.

Similarly to what occurred between 4P2 and 4P3, an identical behaviour in the centre of the plane was observed with an increase in the shielding gas and the production of the 4P4 plane. The geometric changes induced in the new line provided a successive reduction of dilution, leading to its disappearance, both in the central region and in its proximity.

The lack of fusion although appearing under smaller sizes, also appears more frequently in the 4P4 plane, although not in any significant extent. It does not apparently have been altered with shielding gas.

When the overlap percentage is raised to 40%, zigzag (figure 4.11a) and offset-in (figure 4.11b) toolpath techniques are investigated. The plane edge was contoured for zigzag, which deformed the component and resulted in a lack of fusion between tracks as well as a lower uniformity in the plane surface.

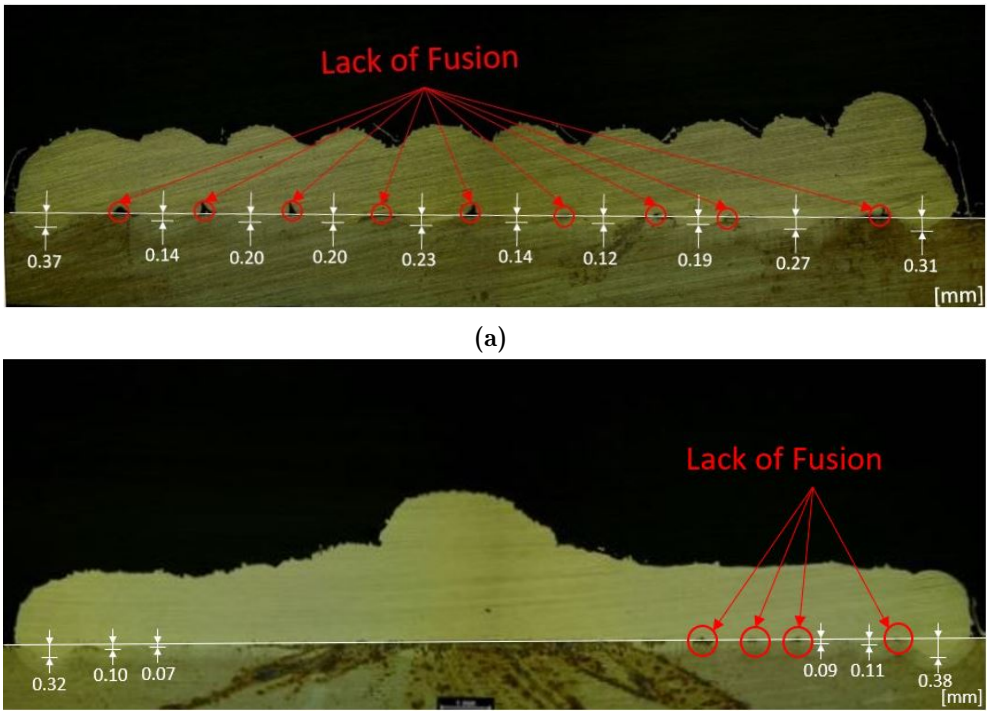

Figure 4.11: a) 4P5 and b) 4P6 cross sections.

Despite this defect, unlike 4P6 offset-in there is clear dilution of the printed material on the substrate. Throughout the cross section of the 4P5 plane there are no major decays in material penetration, ensuring dilution in all areas of the plane.

With offset-in in the 4P6 plane, the same situation did not occur. Compared to 4P4, the increase in overlap created a clear reduction in dilution and further expanded the region that already showed no bonding. The successive increase of the overlap percentage promoted that the energy applied in the fusion of the material was spread not only on the substrate, but also on the adjacent lines during printing. With the reduction of the energy delivered to the substrate, the dilution of the material was reduced until its suppression.

The presence of lack of fusion in 4P6, as expected was improved by increasing the overlap. Its appearance was observed to be even more residual than in 4P4.

The type of method used had a preponderant influence on the aspects described above. As mentioned in section 2.5.2.5, offset toolpath methods achieve a better temperature distribution on the printed material. This therefore leads to a lower energy concentration during printing and consequently a reduction of material dilution. For a zigzag pattern, by conferring worse energy distributions, the high concentration in the material promotes better dilutions, although it may deteriorate the pretended geometric accuracy [55, 56].

Subsequently residue (figure 4.11b and 4.12) and virgin (figure 4.13) IN625 printed

planes were analysed. When the one layer planes in figures 4.11b and 4.13a were investigated, the material quality under the identical printing settings had no influence on the dilution or the surface uniformity of the component. Similar penetrations in the same regions are observed, as well as the same interval with absence of dilution.

As with the residue material, the alloy resulting from the virgin powder impression also shows a minimal lack of fusion at the interface between Inconel 625 and the substrate.

There is a resemblance in the deposition of three planes found in 4.12 and 4.13b. In the alloy from residue powder, a higher frequency of penetration into the substrate is observed, however, the values exhibited besides not being significant when compared to 4P9, exhibit similar values for the matching lines.

Furthermore, as expected from the analysis of the 4P6 and 4P7 planes, the lack of substrate bonding in the central region occurred for both 4P8 and 4P9. The same behaviour was verified for both three-layer planes, as dilution is observed only at the boundaries and its subsequent reduction and later disappearance when approaching the centre.

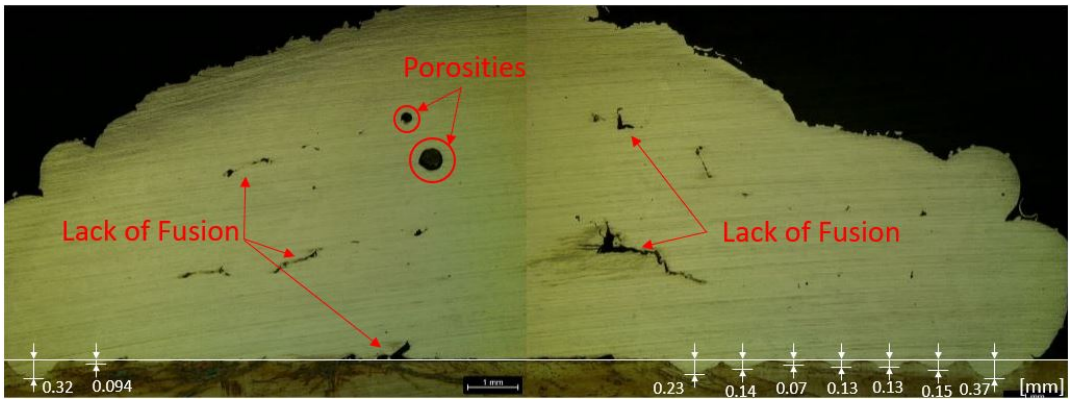

Figure 4.12: 4P7 cross section.

Regarding internal defects, both 4P8 and 4p9 show lack of fusion between layers in the printed alloy and also at the interface with the substrate. Furthermore, Inconel 625 residue exhibits gas porosity, which might be the consequence of trapped gas during the melting process or increased oxygen concentration due to the state of material. In any case, the dilution of both is pretty similar, as are the defects and form after printing.

By the observation of the structural defects pointed out as the lack of fusion, and the reduction of dilution until the absence of bonding of the feeding material with the substrate, it is necessary the optimization of the printing conditions in order to minimize these defects.

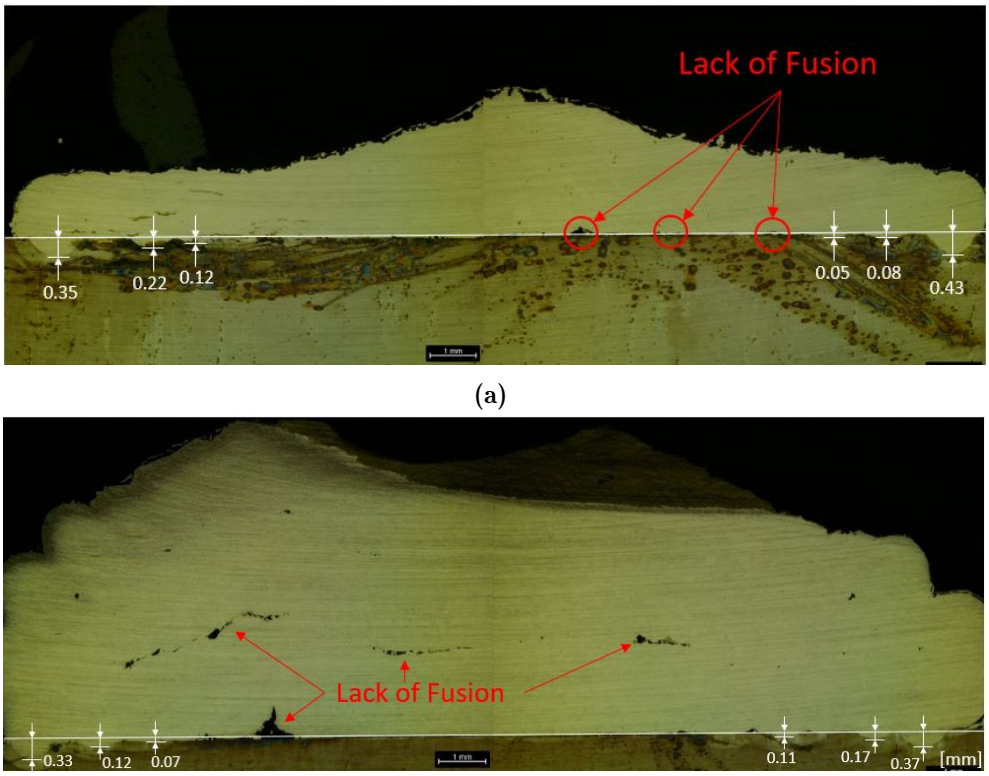

Figure 4.13: a) 4P8 and b) 4P9 planes cross section.

4.3.2.2 Oxidation Analysis

To further understand the impact of powder quality on the oxidation of printed metal, both virgin and waste materials were submitted to SEM analysis, which comprised an microstructure assessment.

In both microstructures, the appearance of elements such as Z0 was common (figure 4.14a and b). By EDS analyses in each material, the appearance of different matrix constituent elements is common, such as Ni, Cr, Mo or Nb, however in both, high concentrations of O are reported. This factor contributes to the assumption, that these fine elements given their sphericity and high amounts of oxygen are probably oxides.

As such, three images (the remaining are presented in the Appendix - C) for the two qualities were used in ImageJ software, where the percentage area of the Z0 elements was performed, and thus provide an estimate of oxidation. To aid this evaluation, tools such as the average area percentage and the standard deviation were used. Subsequent to this data collection, a comparison between the residue and virgin material was performed.

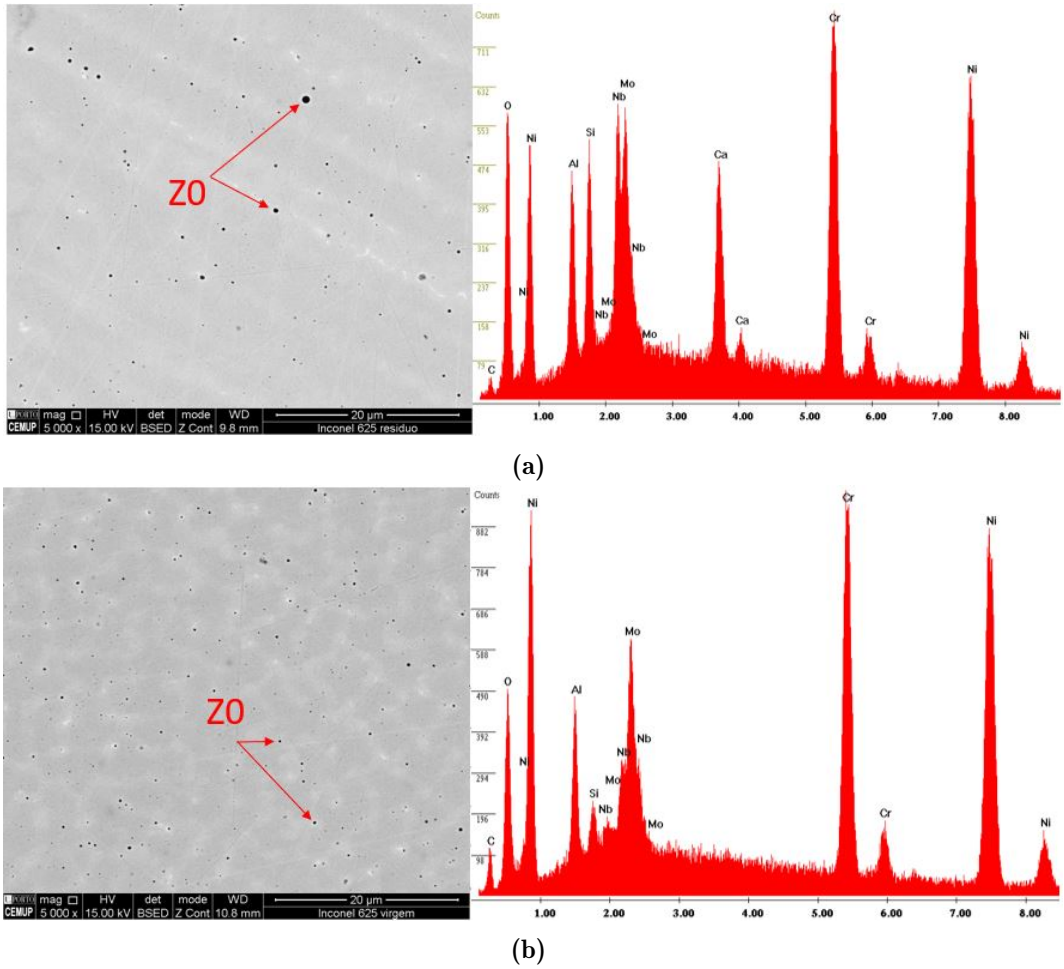

Figure 4.14: a) Residue and b) virgin SEM and EDS analysis .

Table 4.6 shows the results of three distinct image analysis of the oxidation percentage area covered in the both IN625 matrices.

Table 4.6: a) Residue and b) virgin SEM and EDS analysis .

Oxidation Area Percentage [%]	1º Image	2º Image	3º Image	Average
Residue Powder	0.2	0.4	0.2	0.3
Virgin Powder	0.4	0.3	0.4	0.4

Taking into consideration the values presented during all inspections, it can be seen that the residue Inconel 625 has slightly higher values in the second image, while the virgin powder has higher values in the first and third examinations. When all percentage areas for both material qualities are averaged, the presence of oxidation is greater in virgin powder, however, the difference between the two is minimal.

In order to obtain more accurate results, a more extensive study regarding this topic would be necessary. However, this research is in agreement with the idea that after recycling the material the oxidation although it may increase in the material is not significant when compared to a commercial powder. This occurrence evidences that with the recycling of the material from collection and sieving methods, this previously discarded powder could become a viable alternative.

4.3.2.3 Microhardness Assessment

As for the presence of oxidation, also for the virgin and the qualities of the residual material, the mechanical properties, more specifically hardness, were evaluated from distinct measurements on both types. To aid analysis, in addition to the measurements, both the average and standard deviation of the results obtained were taken, with all values detailed in table 4.7.

Table 4.7: Microhardness evaluation of virgin and residue Inconel 625 printed material.

Measurements [HV0.1]	1º	2º	3º	4º	5º	Average	Standard Deviation [%]
Virgin IN625	233	242	263	257	301	259	23
Residue IN625	252	265	259	258	266	260	5

Taking into account the obtained values of microhardness in different regions of the printed material when observed on average, the values for both types prove to be very similar. The standard deviation highlights that despite identical values in terms of mean, metal printed by residue powder shows low disparity in values, unlike metal originated by virgin powder.

The values deviation acquired from metal by virgin powder may be attributable to hardness measurements at locations that experienced different cooling times during the printing process, which has a direct influence on the material's local hardness or due to the mass of the material beneath.

Despite a greater variation in values for virgin metal, the residue powder does not appear to have its mechanical properties, specifically hardness, compromised, for a lower material quality. Not only the material hardness is in agreement with the results from the metal resultant of virgin powder, but is also consistent with the values reported in section 3.1.1.1.

4.4 Inconel 625-Alumina

4.4.1 Parametrization

Following Inconel 625 processing, the composite powder printing was taken and at first, an attempt was made to execute the optimized conditions in line 4. Since the composite powder possessed low flowability, the feeding into the additive manufacturing process was problematic.

Reducing scanning speed and decreasing also laser power became necessary to enable material deposition.

Initially a laser power of 600 W was used, significantly reducing scan speed to 2.5 mm/s to allow a longer feed time during the interaction of the material with the substrate, using a valve opening of 5% to create line 14, however this proved insufficient to achieve an appropriate bead height.

The same thing happened with lines 15, 16, 17, 18, 19, and 20, where the thickness was found to be null despite a drop in laser power and scan speed as well as an elevation in feeding rate and carrier gas.

From line 21 to the remaining, there was a significant rise in the bead height. This modification was caused by a slight and substantial increase in laser power, as well as the opening of the feed valve to 100%. The laser power was augmented to 350 W using total valve opening to generate line 22, which increased thickness but lost the previously attained metallic glow.

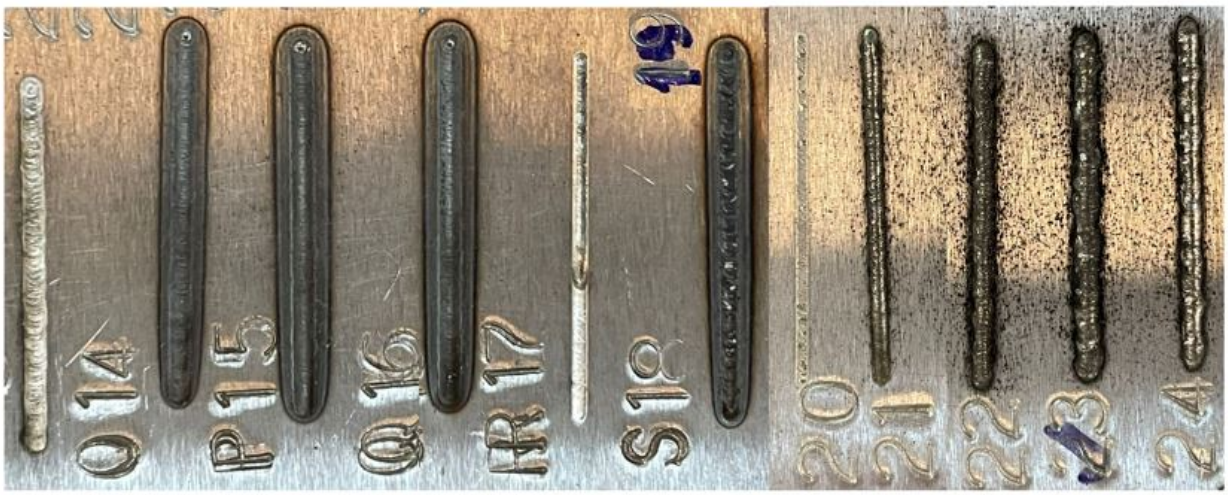

Figure 4.15: Top view of IN625-10 wt.% alumina printed lines.

With constant scanning speed, powder feed rate and carrier gas with the manipulation of the laser power to 450 W in line 23, there was an increase in deposited material and

metallic appearance, however a decrease in bead linearity was also identified. In comparison to the previous two depositions, line 24 was able to recover the previously lost metallic look as well as the linearity at an intermediate energy value of 400 W. Figure 4.15 illustrates the printed composite powder lines.

This behaviour reveals that the application of a carrier gas cannot overcome the poor flowability of the composite powder. Therefore, the mixing conditions should be optimized for future works, avoiding the increase of the particle roughness.

These lines were inspected microscopically in the same way as the Inconel 625 tracks studied. Figure 4.16 displays the resultant beads, while Table 4.8 shows the geometric properties.

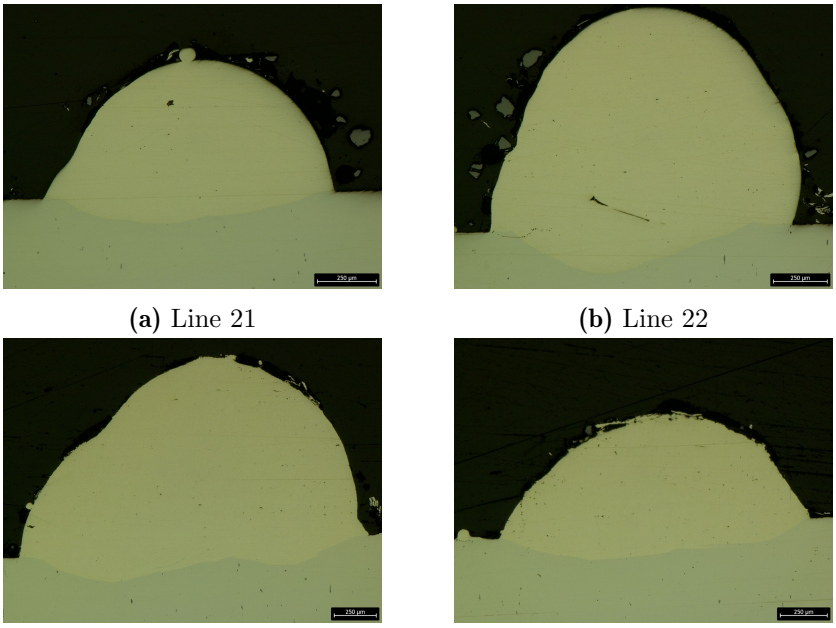

(a) Line 21 **(b)** Line 22

(c) Line 23 **(d)** Line 24

Figure 4.16: Used IN625-10 wt.% Alumina lines cross section.

Table 4.8: Geometrical characteristics of used IN625-10 wt.% Alumina tracks.

Line	H [mm]	W [mm]	D [mm]	Ad [mm^2]	As [mm^2]	Dilution [%]	Left Wettability Angle [°]	Right Wettability Angle[°]
21	0.576	1.261	0.114	0.531	0.085	13.80	60.22	76.30
22	1.028	1.419	0.203	1.185	0.136	10.30	79.48	107.58
23	1.129	2.109	0.181	1.727	0.22	11.30	75.98	60.57
24	0.592	1.645	0.140	0.728	0.176	19.47	58.24	58.43

Apart from occasional inclusions produced by the samples polishing that can be observed in both lines 21 and 22, the prints produced exhibit no visible apparent defects, such

as porosities or cracks, although they do exhibit some spattering on the beads surface.

Due to the material's lack of flowability, the transportation of powder to the melting zone proved unstable and inconsistent. The variation in laser intensity does not appear to have a significant influence on the deposit's dimensions, but rather on the flow rate of powder delivered.

Line 23 gained larger width and height, but not significant penetration regarding the other tracks. Line 22 stood out similarly 23 for its great bead height but, on the other hand, short width and depth dimensions were obtained.

Despite its smaller height, 21 and 24 obtained less disparate penetration as well as a width similar to 22 and 23. It resulted in a deposit area with a lower difference to the dilution area, resulting in improved dilution.

Track 24 has the highest accurate dilution percentage (between 15 and 30%), with the others not presenting appropriate dilution percentages.

Excluding 24, which exhibits good wettability and symmetry of the angles, the angles presented, the corners displayed disparities with more notoriety in 22, where, in addition to this discrepancy being more evident, it also exhibits overly emphasized angles demonstrating its poor wettability.

When submitted to SEM analysis, the microstructure shown in figure 4.17, resulting from the mixture produced becomes more evident.

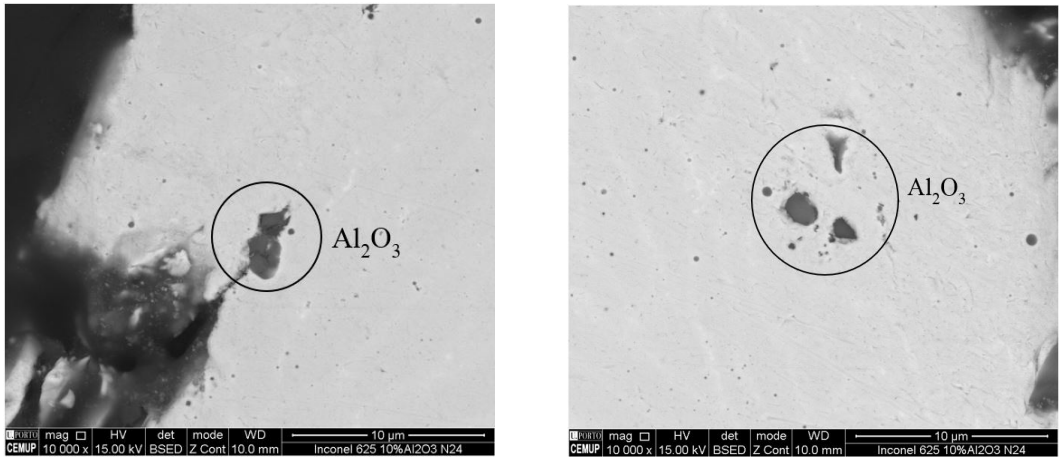

Figure 4.17: Al_2O_3 particles found in the matrix.

It is possible to observe a gamma matrix, where reinforcement particles are sporadically found along the matrix figure, as presented in figure 4.17. A larger percentage of alumina particles spread in the metal matrix was expected, however the frequency of the ceramic elements is low, indicating that the reinforcement powder in the mixture is not homogeneous.

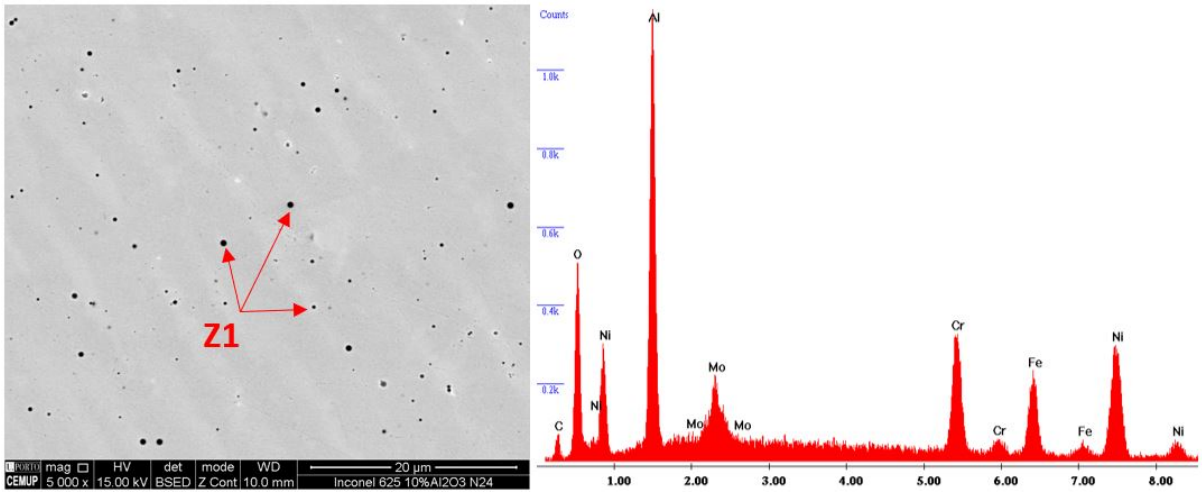

Figure 4.18: SEM and EDS composite powder cross-section analysis.

When examined carefully, elements designated Z1 are found in large quantities in the matrix, as shown in figure 4.18, as well as their EDS spectra. Due to the overall small size of Z1, the EDS has a range that includes material from the Inconel matrix in addition to these components, therefore this may be included in this evaluation.

The first assumption that can be made, is that they are micro particles evolved by oxygen entrapment during the material melting.

The Z1 elements have a predominantly spherical form, which is typical of in-situ oxides and therefore is difficult to associate with reinforcing particles due to their irregular shapes. The interaction is also intimate, supporting the product of the in-situ reaction of the matrix material with these elements.

Since the material's high reactivity with oxygen and the high proportions revealed by EDS, there is a possibility that Z1 represents locally oxidation of the matrix resulting from the IN625 and the printing atmosphere.

Despite this, both aluminium and oxygen compounds are prevalent, followed by typical Inconel constituents such as nickel, chromium, and molybdenum to a lesser extent.

The ultimate suggestion is based on the ceramic reinforcement used. Since the material's typical particle size is on the order of 10 µm, there are particles of both bigger and smaller dimensions involved. This implies that fine alumina particles may have floated on the top of the nickel matrix and have become spread in the surrounding material. The existence high aluminium portions provided by EDS support strongly this assumption. This idea is enforced since there is a great difference in the density of the Inconel 625 and that of the alumina

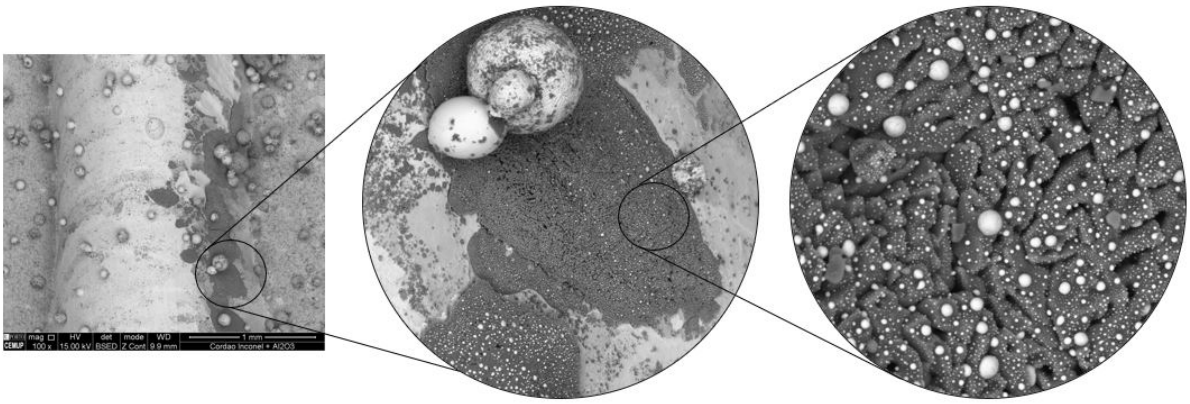

Figure 4.19: SEM analysis on track 24 top view.

In figure 4.19, a SEM analysis is also done on the top of the Inconel625-10 wt.% Alumina track printed. It is noticeable the presence of larger fine spherical particles both on top and around the track.

In addition to this, a dark shape is denoted along the printed line, and when zoomed in on these areas, the presence of agglomerations in large quantities is confirmed that most probably are alumina.

Instead of being disseminated throughout the material's matrix, the ceramic reinforcement has accumulated on top of it. It is speculated that the ceramic material was subsequently transported to the surface of the line due to the marangoni forces inherent in the material melting, culminating in these agglomerations.

4.4.2 Plane Printing

4.4.2.1 Samples Evaluation

After analysis of the Inconel 625-10 wt.% Alumina lines created previously, the parameters that allowed deposition of line 24 were considered for plane printing. The plans printed with this material can be seen in figure 4.20.

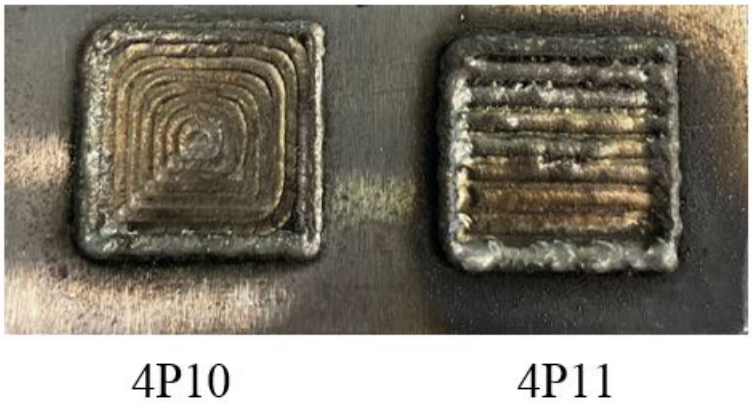

Figure 4.20: IN625-10 wt.% alumina printed planes.

Due to the previously indicated large consumptions, it was proposed in the first phase to print a plan with an offset-in toolpath, creating 4P10. The poor flowability of the material was replicated in the final result once again, as repeated fluctuations in the powder feed rate allowed the contour of the plane to be effectively printed initially, but the remaining track generated received less powder to melt and consequently penetrated the substrate.

Posteriorly a second attempt was made, changing only the print pattern to zigzag. As in the first case, the contouring was done correctly during the material melting process, but there were also oscillations in the material feed rate.

While the machine performed the zigzag pattern, the amount of powder gradually decreased and was ultimately consumed and vaporised. Furthermore, the high fusion energy applied and at the same time, the arrival of tiny powder portions in the meltpool caused the burning of the substrate.

The problem of material flowability was further emphasised at this stage of printing, given the inability to transport carrier gas, which made it impossible to manufacture multi-layered blocks. Hence, the hardness study and more intensive microstructure investigation could not be performed.

4.5 Metco 51060A

4.5.1 Parametrization

Thus, as indicated earlier, due to having a short working time, there was no time to prepare a state of the art on printing Metco 51060A powder. Due to that, were used as a resource the parameters to obtain line 4 with the Inconel 625 residue powder, namely 1200

W, 15 mm/s, and 20 g/min, printing the Metco 51060A and creating track 25. The top view of the printed line can be visualised in figure 4.21.

Figure 4.21: Line 25 top view.

Line 25 showed good linearity, high metallic aspect, and no obvious defects such as porosities or fractures after being printed in a first phase, according to visual analysis and due to this had it parameters chosen for subsequent printings.

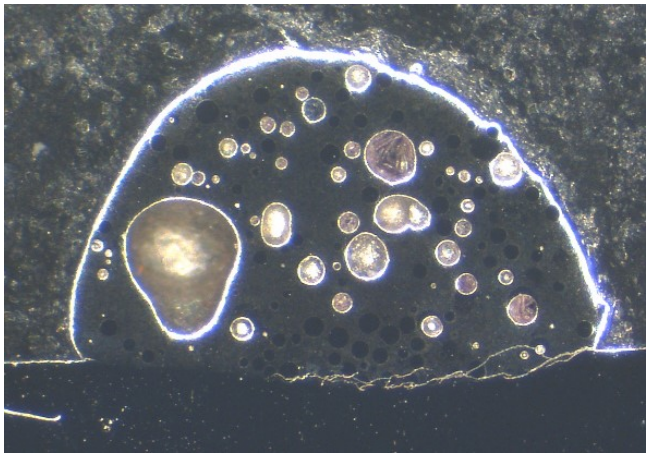

Figure 4.22: Line 25 cross section.

Table 4.9: Line 25 geometrical characteristics

Line	H [mm]	W [mm]	D [mm]	Ad [mm^2]	As [mm^2]	Dilution [%]	left wetting angle [°]	right wetting angle [°]
25	1.112	1.849	0.117	1.653	0.148	8.22	131.85	109.48

While figure 4.22 shows the cross section of the printed metco 51060A track, table 4.9 exposes the geometrical characteristics of the bead. When the sample is evaluated transver-

sally, large porosities and cracks at the interface between the deposited material and the substrate are clearly visible, indicating a high presence of defects.

Some of the pores (between 106 and 45 µm) shown may have formed during the material's cutting process. Since the reinforcement has a high hardness, the application of discs with a lower hardness than carbon tungsten may have contributed in the removal of some unmelted ceramic particles during this action. However, mostly are rounded with smooth surfaces, being gas porosities.

Furthermore, based on the geometric properties of the line, it has a significant height (H) and width (W), but on the other hand a very low depth (D). As a result, there was a large area in the deposit region (Ad) and a relatively small area in the dilution zone (As), resulting in very little dilution of the printed metal on the substrate.

The cross-section also exhibited poor wettability, with both angles gaining dissimilar values while being extremely high. Based on the indicated findings, in order to answer to the detected defects and insufficient dilution, the employed parameters would need to be optimized.

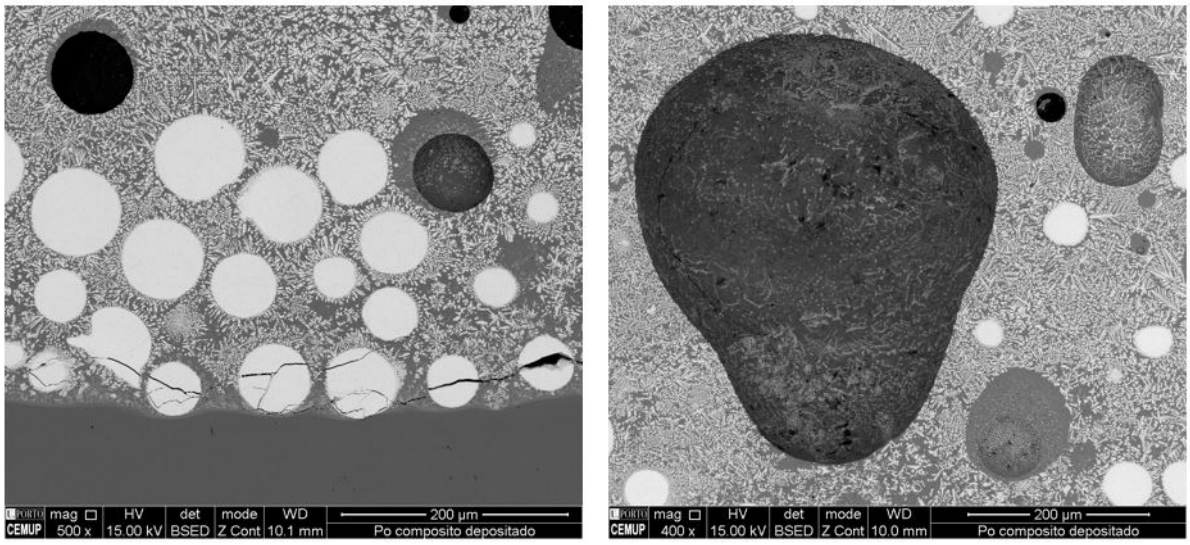

Figure 4.23: Metco 51060A SEM analysis.

Besides all the defects associated with this printing process, the sample when submitted to SEM analysis reveals a complex microstructure. This is exhibited in Figure 4.23.

When the microstructure is magnified, several elements with different morphologies and atomic constracts may be seen. The commercial composite powder, when melted and later solidified, displays a nickel-based matrix, with the presence of chromium, iron, and silicon represented by Z2, and detected via EDS analysis, as shown in figure 4.24 a). There are also bright particles, shown as Z3, that are rich in tungsten.

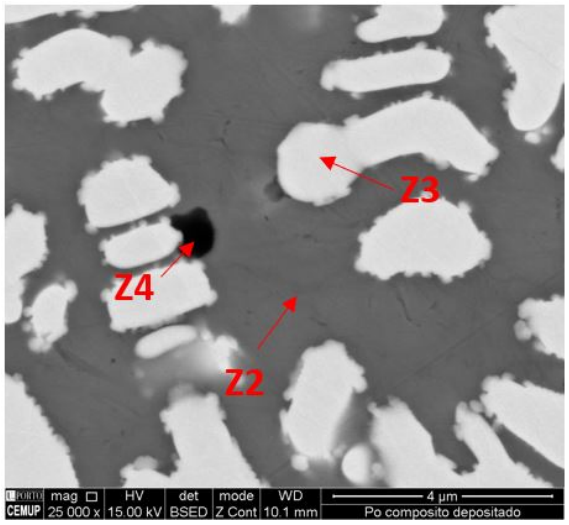

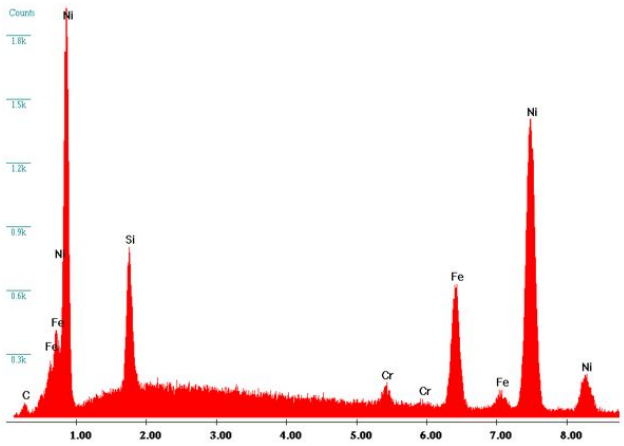

(a) Z2

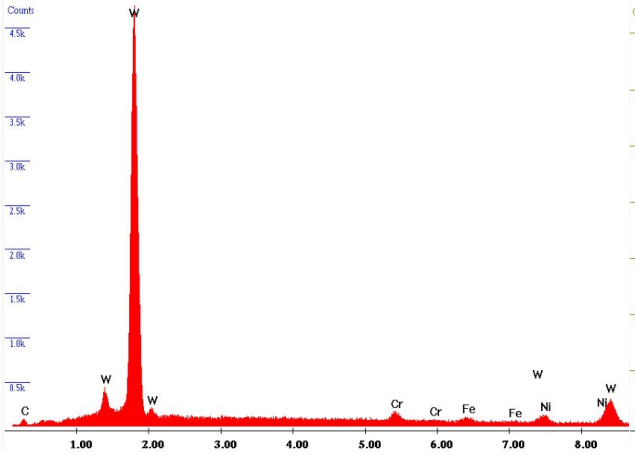

(b) Z3

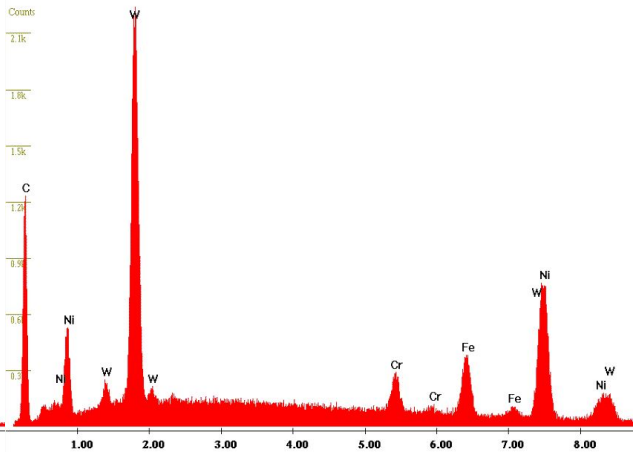

(c) Z4

Figure 4.24: SEM images and EDS analysis of a) Z2, b) Z3 and c) Z4.

Dark zones like Z4 (figure 4.24c) can be found dispersed in the metallic matrix. This region should be constituted of a low atomic density compoud.

However, in the spectra of Z4, figure 4.24c, the peaks of W, Cr, Fe e Ni are seen, caused by volume interaction. Since, as described earlier, the EDS range inevitably includes the neighborhood of the material under investigation, therefore both materials are detected. The fact that WC particles when exposed to high temperatures are prone to decarburize (reactions 4.1 and 4.2) and given the element's high carbon concentrations, it is expected that several carbon-based phases have emerged [110].

$$2\,\mathrm{WC} \longrightarrow \mathrm{WC} + \mathrm{C} \tag{4.1}$$

$$W_2C \longrightarrow 2\,W + C \tag{4.2}$$

The element present in large quantities, however is WC reinforcement, which evolves in various forms. In both Z3 (figure 4.24b) and Z6 (figure 4.25b), the precipitation of carbides occurs by phenomena of diffusion and mutual dissolution of the nickel-based matrix, together with the reinforcement.

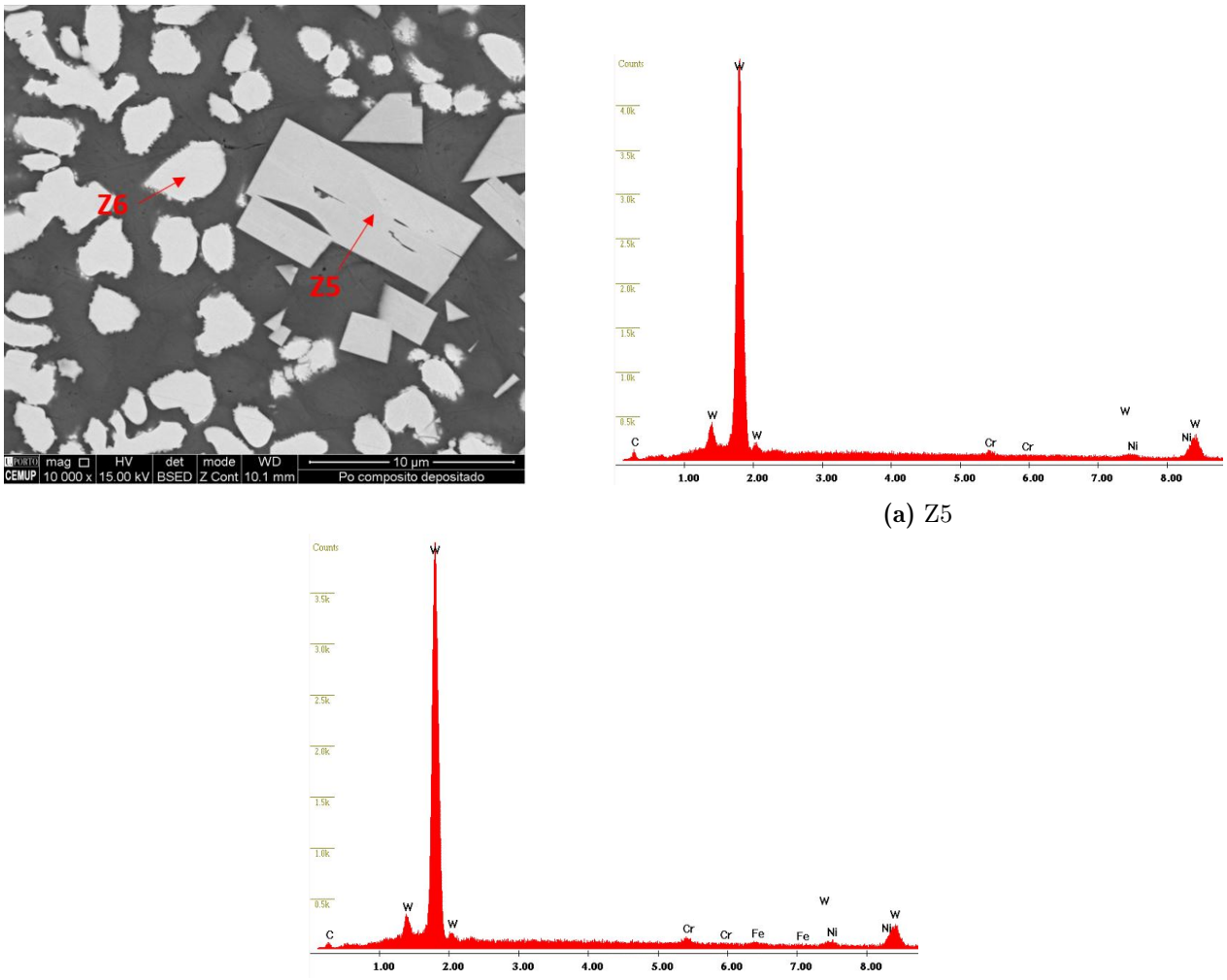

(a) Z5

(b) Z6

Figure 4.25: SEM images and EDS analysis of a) Z5, and b) Z6.

The spherical WC particles referred as Z7 in figure 4.26a, and positioned along the matrix are likewise identified, also evidenced by EDS due to the high tungsten content. Around these, it is identifiable the precipitation of carbides in the form of dendrites.

At the boundary with the matrix, another kind of phase identified as Z8 located at the border of these W particles (figure 4.26b). The tungsten carbide along with the NiCrSiBC matrix, similarly to Z3 and Z6, by dissolution and diffusion, in-situ reactions occurred to form angular carbides at the reinforcements interface.

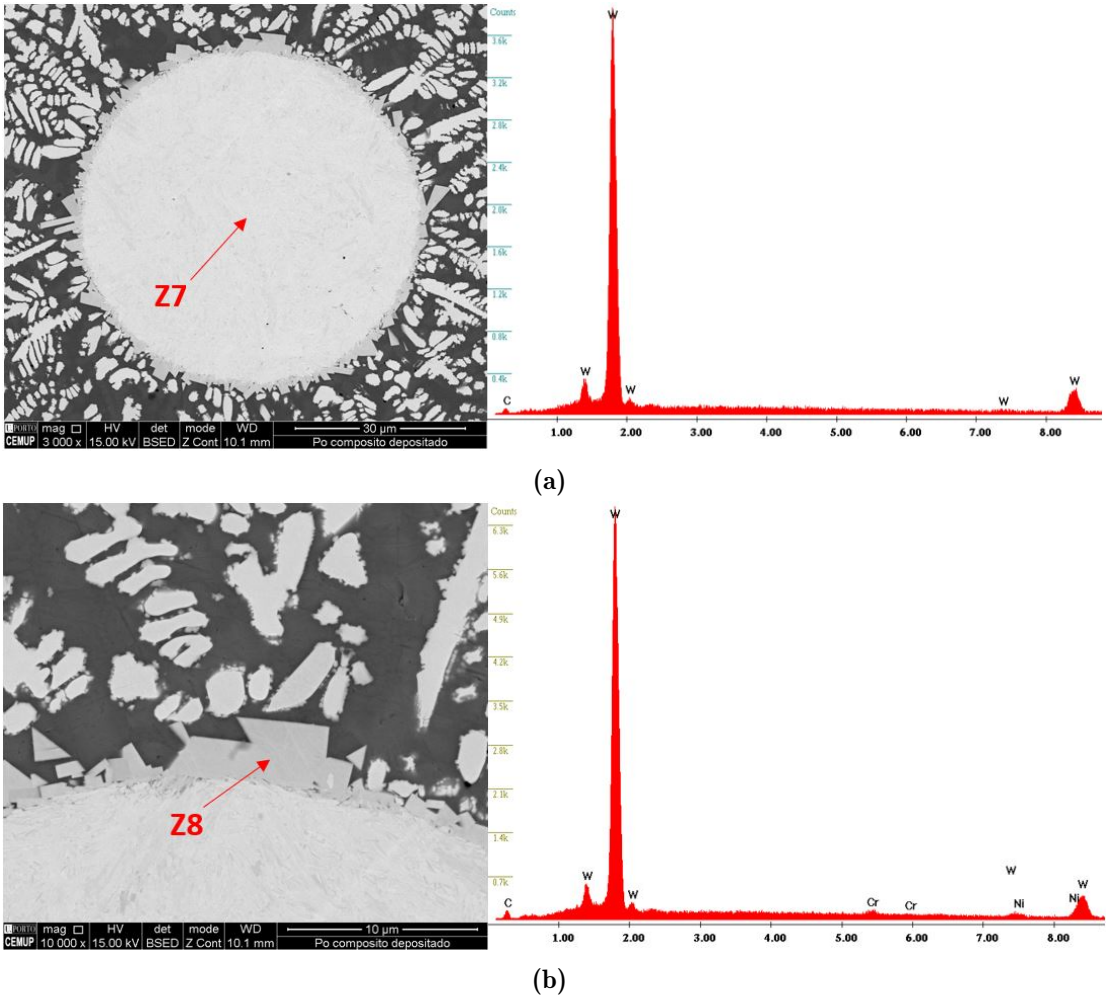

Figure 4.26: SEM images and EDS analysis of the a) Z7, and b) Z8.

This phase's in other areas of the matrix is observed beyond to its presence at the interface of the spherical WC particles. Elements having similar appearance to those found near particle boundaries, such as Z5 (Figure 4.25a), are also discovered.

These phases have the shape of simple polygons, similarly to Z8. Since both elements have a similar chemical composition, it is assumed that they were also created by in-situ reactions between the reinforcement and metal components.

4.5.2 Plane Printing

4.5.2.1 Samples Evaluation

Depositions were made using a raster toolpath, following line printing on both the 1 (4P12) and 3 (4P13) planes of 20x20 mm. By visual analysis of the first plan printed, the following printing of a block of 3 plans was conducted.

Figure 4.27: 4P12 printed plane.

Similarly to line 25, both planes presented high metallic aspect and homogeneity, with no spattering or visible surface defects. Figure 4.27 depicts 4P12 printed plane of metco 51060A.

However, when cut and analyzed in cross-section, the phenomena already identified in line 25 occur with larger repercussion in both samples, as predicted. A large amount of pores, as well as cracks, are present in both 4P12 and 4P13 as figure 4.28 shows (magnified images are available in the Appendix - D).

Furthermore, the dilution appears to be smaller in both the plane and the block generated than in the previously printed line. This must be related to the impact documented with the Inconel 625 residual material, namely the dissipation of laser power from the machine to the adjacent lines during track printing.

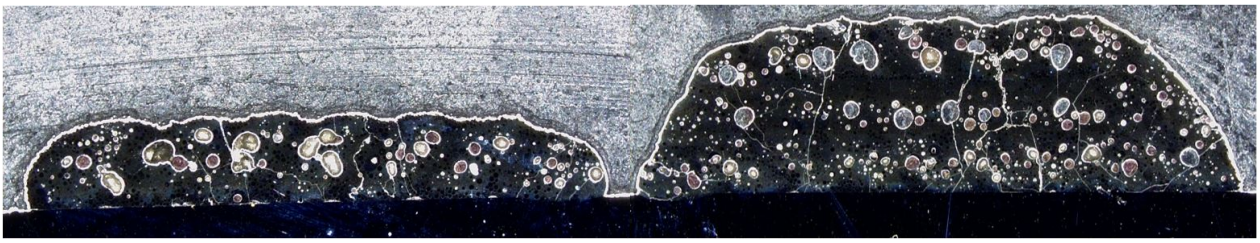

(a) **(b)**

Figure 4.28: a) 4P12 and b) 4P13 planes cross section.

Higher laser powers might be a valuable resource for improving the state of Metco 51060A planes. With the use of higher order energies, it is possible to solve the presence of pores by a more effective melting of the metallic powder, while also allowing for larger dilutions.

Sadhu et al. recommend heating the substrate before the deposition process to address defects found in the microstructure of the post-printed material. Fast cooling rates provide high thermal gradients, which introduce stresses into the material and, as a result, cracking occurs [110].

By pre-heating the substrate, the times for the material to cool is longer, and consequently creates smoother thermal gradients. Other publications suggest that by using heating during the DED process results in a reduction in porosity in the material [111].

Chapter 5

Conclusions and Future Works

5.1 Conclusions

The development and analysis of a composite powder consisting of Inconel 625 residue and Alumina was proposed as part of the current investigation's sequence. To accomplish the same goal, both the residue powder and the mixed powder were utilized as raw and printed materials, and additionally the commercial powder metco 51060A.

The following findings were obtained in each material:

1. **Inconel 625 residue**
    - Using the ASTM B213-97 test, an average powder flow rate of 10.42 s/50 g was measured;
    - During the parameterization of Inconel, lines with favorable traits were acquired for the application of its parameters in plane fabrication, notably 4, who was latter employed (1200 W, 15 mm/s, 20 g/min);
    - The alloy was tested for distinct tool paths and overlaps, surface oxidation, and low/no dilution during plan manufacture was verified;
    - The material resultant from residue powder was compared to the commercial virgin one also printed for the same parameters, and both exhibited low/null dilution, surface oxidation and defects such as lack of melting or porosities;
    - When comparing the material from residue with that from commercial virgin powder, both exhibited similar oxidation and hardness, regardless of the quality of the material, demonstrating a sustainable alternative to commercial powder.
2. **Inconel 625 residue-10 wt.% Alumina**
    - Using both the ASTM B213-97 and ASTM B964-09 tests, the powder remained stationary presenting lack of flowability;
    - The applied powder mixing method caused a reduction in flowability due to an increase in particle roughness, induced by the adhesion of the reinforcement on the Inconel 625 particles;

- Feeding issues developed throughout the parameterisation process due to the consistency of the mixture, but an improved line (400 W, 0.5 mm/s, 100 g/min), was achieved without defects and with good dilution;
- The microstructure of the printed line is constituted by gamma matrix embedding fine aluminium oxide particles, though agglomerations are observed on the surface of the printed line;
- Once applied to more prolonged build-ups, such as planes, the feeding issues intensified, resulting in the vaporisation of the powder and the substrate burning.

3. **Metco 51060A**

   - The same parameters used to form line 4 with Inconel 625 residue (1200 W, 15 mm/s, 20 g/min) were applied to produce a printed line with good surface appearance, however cracks and pores of varying dimensions were observed;
   - The material revealed to be complex microstructurally, consisting of a nickel-based matrix in which carbides of various forms (angular blocks, dendrites and spherical particles) precipitated by diffusion and dissolution between the reinforcement and the matrix. Moreover the decomposition of WC to W+C was observed;
   - In the one and three planes printing for the same conditions, a greater manifestation of the previously issues (porosities and cracks) was observed in both samples;
   - High cooling rates during the process resulted in high thermal gradients in the material and the creation of stresses and consequently cracks.

5.2 Future Works

The next steps could be taken to complement the current study, as a follow-up to the themes discussed:

1. **Inconel 625 residue**

   - Optimising the printing conditions of the material, in order to improve the dilution with increased laser power or reduction of scanning speed, and further study both the microstructure and hardness of the material in the heat affected zone;
   - Studying the effect number of cycles that the reutilized Inconel 625 powder can be used for consecutive production, both in material properties and microstructure;

2. **Inconel 625 residue-10 wt.% Alumina**

- Improvement of the mixing process, and therefore the flowability of the resulting powder. Optimisation of the printing conditions of the material and also properties, as well as microstructure characterization of the printings with the new mixture;
- Mixture of residue Inconel 625 powder with Alumina (nano particle size), and further propertie and microstructure characacterization. Comparison of properties, such as hardness and wear resistance for Inconel 625-Alumina nano and micron sizes. However health conditions should be observed strongly for the operators since nanoparticles can be easily sniffed or penetrated into the skin;
- Comparison of properties, such as hardness and wear resistance for Inconel 625 residue and Inconel 625 residue-10 wt.% Alumina.

3. **Metco 51060A**

- Optimisation of printing conditions for the material, with the substrate preheating and properties and microstructure characterization of the printings, by laser power increase and/or a scan speed reduction;
- Comparison of properties, namely hardness and wear resistance for Inconel 625 residue-10 wt.% Alumina, with this commercial powder.

Bibliography

[1] Tao Peng, Karel Kellens, Renzhong Tang, Chao Chen, and Gang Chen. Sustainability of additive manufacturing: An overview on its energy demand and environmental impact. *Additive Manufacturing*, 21:694–704, 2018.

[2] R Sreenivasan, A Goel, and David L Bourell. Sustainability issues in laser-based additive manufacturing. *Physics Procedia*, 5:81–90, 2010.

[3] Yahya Lahrour and Daniel Brissaud. A technical assessment of product/component re-manufacturability for additive remanufacturing. *Procedia Cirp*, 69:142–147, 2018.

[4] Jon Iñaki Arrizubieta, Olatz Ukar, Marta Ostolaza, and Arantza Mugica. Study of the environmental implications of using metal powder in additive manufacturing and its handling. *Metals*, 10(2):261, 2020.

[5] Shaik Himam Saheb, Vinay Kumar Durgam, and A Chandrashekhar. A review on metal powders in additive manufacturing. In *AIP Conference Proceedings*, volume 2281, page 020018. AIP Publishing LLC, 2020.

[6] John J Dunkley. Metal powder atomisation methods for modern manufacturing. *Johnson Matthey Technology Review*, 63(3):226–232, 2019.

[7] Kazybek Kassym and Asma Perveen. Atomization processes of metal powders for 3d printing. *Materials today: proceedings*, 26:1727–1733, 2020.

[8] Leo VM Antony and Ramana G Reddy. Processes for production of high-purity metal powders. *Jom*, 55(3):14–18, 2003.

[9] Jason Dawes, Robert Bowerman, and Ross Trepleton. Introduction to the additive manufacturing powder metallurgy supply chain. *Johnson Matthey Technology Review*, 59(3):243–256, 2015.

[10] R Gerling, H Clemens, and FP Schimansky. Powder metallurgical processing of intermetallic gamma titanium aluminides. *Advanced Engineering Materials*, 6(1-2):23–38, 2004.

[11] Iver E Anderson, Emma MH White, and Ryan Dehoff. Feedstock powder processing research needs for additive manufacturing development. *Current Opinion in Solid State and Materials Science*, 22(1):8–15, 2018.

[12] Catarina Duarte Batista, Adriana André Martins das Neves de Pinho Fernandes, Maria Teresa Freire Vieira, and Omid Emadinia. From machining chips to raw material for powder metallurgy—a review. *Materials*, 14(18):5432, 2021.

[13] Jiri Zegzulka, Daniel Gelnar, Lucie Jezerska, Rostislav Prokes, and Jiri Rozbroj. Characterization and flowability methods for metal powders. *Scientific Reports*, 10(1):1–19, 2020.

[14] John A Slotwinski and Edward J Garboczi. Metrology needs for metal additive manufacturing powders. *Jom*, 67(3):538–543, 2015.

[15] Marie Naiim, Abdelbassit Boualem, Caroline Ferre, Meryem Jabloun, Alain Jalocha, and Philippe Ravier. Multiangle dynamic light scattering for the improvement of multimodal particle size distribution measurements. *Soft matter*, 11(1):28–32, 2015.

[16] Valdek Mikli, Helmo Kaerdi, Priit Kulu, and Michal Besterci. Characterization of powder particle morphology. *Proceedings of the Estonian Academy of Sciences: Engineering(Estonia)*, 7(1):22–34, 2001.

[17] Mario Renderos, Amaia Torregaray, M$^{\underline{a}}$ Esther Gutierrez-Orrantia, Aitzol Lamikiz, Nicolas Saintier, and Franck Girot. Microstructure characterization of recycled in718 powder and resulting laser clad material. *Materials Characterization*, 134:103–113, 2017.

[18] Heesoo Choi, Sumin Kim, Masahiro Goto, and Sangshik Kim. Effect of powder recycling on room and elevated temperature damage tolerability of inconel 718 alloy fabricated by laser powder bed fusion. *Materials Characterization*, 171:110818, 2021.

[19] Peeyush Nandwana, William H Peter, Ryan R Dehoff, Larry E Lowe, Michael M Kirka, Francisco Medina, and Sudarsanam S Babu. Recyclability study on inconel 718 and ti-6al-4v powders for use in electron beam melting. *Metallurgical and Materials Transactions B*, 47(1):754–762, 2016.

[20] Gowtham Soundarapandiyan, Carol Johnston, Raja HU Khan, Bo Chen, and Michael E Fitzpatrick. A technical review of the challenges of powder recycling in the laser powder bed fusion additive manufacturing process. *IET Journal of Engineering*, 2021(2):97–103, 2021.

[21] Konrad Gruber, Irina Smolina, Marcin Kasprowicz, and Tomasz Kurzynowski. Evaluation of inconel 718 metallic powder to optimize the reuse of powder and to improve the performance and sustainability of the laser powder bed fusion (lpbf) process. *Materials*, 14(6):1538, 2021.

[22] Timothy J Horn and Ola LA Harrysson. Overview of current additive manufacturing technologies and selected applications. *Science progress*, 95(3):255–282, 2012.

[23] K Rajaguru, T Karthikeyan, and V Vijayan. Additive manufacturing–state of art. *Materials today: proceedings*, 21:628–633, 2020.

[24] Kaufui V Wong and Aldo Hernandez. A review of additive manufacturing. *International scholarly research notices*, 2012, 2012.

[25] Mary Kathryn Thompson, Giovanni Moroni, Tom Vaneker, Georges Fadel, R Ian Campbell, Ian Gibson, Alain Bernard, Joachim Schulz, Patricia Graf, Bhrigu Ahuja, et al. Design for additive manufacturing: Trends, opportunities, considerations, and constraints. *CIRP annals*, 65(2):737–760, 2016.

[26] Amit Bandyopadhyay and Susmita Bose. *Additive manufacturing*. CRC press, 2019.

[27] Wei Gao, Yunbo Zhang, Devarajan Ramanujan, Karthik Ramani, Yong Chen, Christopher B Williams, Charlie CL Wang, Yung C Shin, Song Zhang, and Pablo D Zavattieri. The status, challenges, and future of additive manufacturing in engineering. *Computer-Aided Design*, 69:65–89, 2015.

[28] Benjamin Vayre, Frédéric Vignat, and François Villeneuve. Metallic additive manufacturing: state-of-the-art review and prospects. *Mechanics & Industry*, 13(2):89–96, 2012.

[29] David Bourell, Jean Pierre Kruth, Ming Leu, Gideon Levy, David Rosen, Allison M Beese, and Adam Clare. Materials for additive manufacturing. *CIRP annals*, 66(2):659–681, 2017.

[30] Ugur M Dilberoglu, Bahar Gharehpapagh, Ulas Yaman, and Melik Dolen. The role of additive manufacturing in the era of industry 4.0. *Procedia Manufacturing*, 11:545–554, 2017.

[31] Jungeon Lee, Hyung Jun Park, Seunghak Chai, Gyu Ri Kim, Hwanwoong Yong, Suk Joo Bae, and Daeil Kwon. Review on quality control methods in metal additive manufacturing. *Applied Sciences*, 11(4):1966, 2021.

[32] Dong-Gyu Ahn. Directed energy deposition (ded) process: State of the art. *International Journal of Precision Engineering and Manufacturing-Green Technology*, 8(2):703–742, 2021.

[33] David Svetlizky, Mitun Das, Baolong Zheng, Alexandra L Vyatskikh, Susmita Bose, Amit Bandyopadhyay, Julie M Schoenung, Enrique J Lavernia, and Noam Eliaz. Directed energy deposition (ded) additive manufacturing: Physical characteristics, defects, challenges and applications. *Materials Today*, 49:271–295, 2021.

[34] Scott M Thompson, Linkan Bian, Nima Shamsaei, and Aref Yadollahi. An overview of direct laser deposition for additive manufacturing; part i: Transport phenomena, modeling and diagnostics. *Additive Manufacturing*, 8:36–62, 2015.

[35] Ian Gibson Ian Gibson. Additive manufacturing technologies 3d printing, rapid prototyping, and direct digital manufacturing, 2015.

[36] Thomas Lehmann, Dylan Rose, Ehsan Ranjbar, Morteza Ghasri-Khouzani, Mahdi Tavakoli, Hani Henein, Tonya Wolfe, and Ahmed Jawad Qureshi. Large-scale metal additive manufacturing: a holistic review of the state of the art and challenges. *International Materials Reviews*, pages 1–50, 2021.

[37] Barun Haldar and P Saha. Identifying defects and problems in laser cladding and suggestions of some remedies for the same. *Materials Today: Proceedings*, 5(5):13090–13101, 2018.

[38] William E Frazier. Metal additive manufacturing: a review. *Journal of Materials Engineering and performance*, 23(6):1917–1928, 2014.

[39] SL Sing, CF Tey, JHK Tan, S Huang, and Wai Yee Yeong. 3d printing of metals in rapid prototyping of biomaterials: Techniques in additive manufacturing. In *Rapid prototyping of biomaterials*, pages 17–40. Elsevier, 2020.

[40] GA Barragan, D Rojas, JS Grass, and RT Coelho. Observations on laser additive manufacturing (lam) in terms of directed energy deposition (ded) with metal powder feedstock. *Lasers in Engineering (Old City Publishing)*, 50, 2021.

[41] Rasheedat Modupe Mahamood. *Laser metal deposition process of metals, alloys, and composite materials*. Springer, 2018.

[42] Dara Moazami Goodarzi, Joonas Pekkarinen, and Antti Salminen. Effect of process parameters in laser cladding on substrate melted areas and the substrate melted shape. *Journal of Laser Applications*, 27(S2):S29201, 2015.

[43] Suhas Sreekanth, Ehsan Ghassemali, Kjell Hurtig, Shrikant Joshi, and Joel Andersson. Effect of direct energy deposition process parameters on single-track deposits of alloy 718. *Metals*, 10(1):96, 2020.

[44] Adrita Dass and Atieh Moridi. State of the art in directed energy deposition: From additive manufacturing to materials design. *Coatings*, 9(7):418, 2019.

[45] DR Feenstra, A Molotnikov, and N Birbilis. Utilisation of artificial neural networks to rationalise processing windows in directed energy deposition applications. *Materials & Design*, 198:109342, 2021.

[46] Eun Mi Lee, Gwang Yong Shin, Hi Seak Yoon, and Do Sik Shim. Study of the effects of process parameters on deposited single track of m4 powder based direct energy deposition. *Journal of Mechanical Science and Technology*, 31(7):3411–3418, 2017.

[47] Yanmin Li, Haiou Yang, Xin Lin, Weidong Huang, Jianguo Li, and Yaohe Zhou. Laser direct forming of metal components: technical characterizations. In *Lasers in Material Processing and Manufacturing*, volume 4915, pages 395–402. SPIE, 2002.

[48] G Chryssolouris, S Zannis, K Tsirbas, and C Lalas. An experimental investigation of laser cladding. *CIRP Annals*, 51(1):145–148, 2002.

[49] Do-Sik Shim, Gyeong-Yun Baek, Jin-Seon Seo, Gwang-Yong Shin, Kee-Poong Kim, and Ki-Yong Lee. Effect of layer thickness setting on deposition characteristics in direct energy deposition (ded) process. *Optics & Laser Technology*, 86:69–78, 2016.

[50] Jong-Sup Lim, Won-Jung Oh, Choon-Man Lee, and Dong-Hyeon Kim. Selection of effective manufacturing conditions for directed energy deposition process using machine learning methods. *Scientific reports*, 11(1):1–13, 2021.

[51] André A Ferreira, Ana R Reis, Rui L Amaral, João M Cruz, Pedro C Romio, Jorge O Seabra, and Manuel F Vieira. Mechanical and microstructural characterisation of bulk inconel 625 produced by direct laser deposition. *Materials Science and Engineering: A*, 838:142777, 2022.

[52] Eun Seong Kim, Farahnaz Haftlang, Soung Yeoul Ahn, Gang Hee Gu, and Hyoung Seop Kim. Effects of processing parameters and heat treatment on the microstructure and magnetic properties of the in-situ synthesized fe-ni permalloy produced using direct energy deposition. *Journal of Alloys and Compounds*, 907:164415, 2022.

[53] Kandice SB Ribeiro, Fábio E Mariani, and Reginaldo T Coelho. A study of different deposition strategies in direct energy deposition (ded) processes. *Procedia Manufacturing*, 48:663–670, 2020.

[54] Yingbin Hu and Weilong Cong. A review on laser deposition-additive manufacturing of ceramics and ceramic reinforced metal matrix composites. *Ceramics International*, 44(17):20599–20612, 2018.

[55] Donghong Ding, Zengxi Stephen Pan, Dominic Cuiuri, and Huijun Li. A tool-path generation strategy for wire and arc additive manufacturing. *The international journal of advanced manufacturing technology*, 73(1):173–183, 2014.

[56] Jun Yu, Xin Lin, Liang Ma, Junjie Wang, Xingling Fu, Jing Chen, and Weidong Huang. Influence of laser deposition patterns on part distortion, interior quality and mechanical properties by laser solid forming (lsf). *Materials Science and Engineering: A*, 528(3):1094–1104, 2011.

[57] Donghong Ding, Zengxi Pan, Dominic Cuiuri, Huijun Li, and Nathan Larkin. Adaptive path planning for wire-feed additive manufacturing using medial axis transformation. *Journal of Cleaner Production*, 133:942–952, 2016.

[58] Tobias Wasser, Anshu Dhar Jayal, and Christoph Pistor. Implementation and evaluation of novel buildstyles in fused deposition modeling (fdm). In *1999 International Solid Freeform Fabrication Symposium*, 1999.

[59] Jon Flores, Iker Garmendia, and Joseba Pujana. Toolpath generation for the manufacture of metallic components by means of the laser metal deposition technique. *The International Journal of Advanced Manufacturing Technology*, 101(5):2111–2120, 2019.

[60] GQ Jin, Weidong D Li, and L Gao. An adaptive process planning approach of rapid prototyping and manufacturing. *Robotics and Computer-Integrated Manufacturing*, 29(1):23–38, 2013.

[61] Katherine L Terrassa, Thale R Smith, Sen Jiang, Joshua D Sugar, and Julie M Schoenung. Improving build quality in directed energy deposition by cross-hatching. *Materials Science and Engineering: A*, 765:138269, 2019.

[62] Václav Ocelík, O Nenadl, A Palavra, and J Th M De Hosson. On the geometry of coating layers formed by overlap. *Surface and Coatings Technology*, 242:54–61, 2014.

[63] Daichi Tanigawa, Nobuyuki Abe, Masahiro Tsukamoto, Yoshihiko Hayashi, Hiroyuki Yamazaki, Yoshihiro Tatsumi, and Mikio Yoneyama. Effect of laser path overlap on surface roughness and hardness of layer in laser cladding. *Science and Technology of Welding and Joining*, 20(7):601–606, 2015.

[64] Yanxiang Li and Jian Ma. Study on overlapping in the laser cladding process. *Surface and Coatings Technology*, 90(1-2):1–5, 1997.

[65] Parvaneh Zareh and RJ Urbanic. Experimental analysis of single layer multi-track deposition of clad beads with variable overlap percentages. *The International Journal of Advanced Manufacturing Technology*, 109(5):1511–1525, 2020.

[66] Andreas Mortensen and Javier Llorca. Metal matrix composites. *Annual review of materials research*, 40:243–270, 2010.

[67] Mario Rosso. Ceramic and metal matrix composites: Routes and properties. *Journal of materials processing technology*, 175(1-3):364–375, 2006.

[68] Andre Mussatto, Inam UI Ahad, Reza Taherzadeh Mousavian, Yan Delaure, and Dermot Brabazon. Advanced production routes for metal matrix composites. *Engineering reports*, 3(5):e12330, 2021.

[69] NR Bandyopadhyay, S Ghosh, and A Basumallick. New generation metal matrix composites. *Materials and manufacturing processes*, 22(6):679–682, 2007.

[70] SC Tjong and ZY Ma. Microstructural and mechanical characteristics of in situ metal matrix composites. *Materials Science and Engineering: R: Reports*, 29(3-4):49–113, 2000.

[71] F He. Ceramic nanoparticles in metal matrix composites. In *Ceramic Nanocomposites*, pages 185–207. Elsevier, 2013.

[72] Riccardo Casati and Maurizio Vedani. Metal matrix composites reinforced by nanoparticles—a review. *Metals*, 4(1):65–83, 2014.

[73] Karl Ulrich Kainer. Basics of metal matrix composites. *Metal Matrix Composites: Custom-made Materials for Automotive and Aerospace Engineering*, pages 1–54, 2006.

[74] William C Harrigan Jr. Commercial processing of metal matrix composites. *Materials Science and Engineering: A*, 244(1):75–79, 1998.

[75] JW Kaczmar, K Pietrzak, and W Włosiński. The production and application of metal matrix composite materials. *Journal of materials processing technology*, 106(1-3):58–67, 2000.

[76] W Ames and AT Alpas. Wear mechanisms in hybrid composites of graphite-20 pct sic in a356 aluminum alloy (al-7 pct si-0.3 pct mg). *Metallurgical and Materials Transactions A*, 26(1):85–98, 1995.

[77] Guttikonda Manohar, Abhijit Dey, KM Pandey, and SR Maity. Fabrication of metal matrix composites by powder metallurgy: a review. In *AIP conference proceedings*, volume 1952, page 020041. AIP Publishing LLC, 2018.

[78] DL Zhang. Processing of advanced materials using high-energy mechanical milling. *Progress in Materials Science*, 49(3-4):537–560, 2004.

[79] Eskandar Fereiduni, Ali Ghasemi, and Mohamed Elbestawi. Selective laser melting of aluminum and titanium matrix composites: Recent progress and potential applications in the aerospace industry. *Aerospace*, 7(6):77, 2020.

[80] Carl C Koch and JD Whittenberger. Mechanical milling/alloying of intermetallics. *Intermetallics*, 4(5):339–355, 1996.

[81] Malaya Prasad Behera, Troy Dougherty, and Sarat Singamneni. Conventional and additive manufacturing with metal matrix composites: a perspective. *Procedia Manufacturing*, 30:159–166, 2019.

[82] Yongzhong Zhang, Zengmin Wei, Likai Shi, and Mingzhe Xi. Characterization of laser powder deposited ti–tic composites and functional gradient materials. *Journal of materials processing technology*, 206(1-3):438–444, 2008.

[83] Jing Shi and Yachao Wang. Development of metal matrix composites by laser-assisted additive manufacturing technologies: a review. *Journal of Materials Science*, 55(23):9883–9917, 2020.

[84] Bo Chen, Xin Xi, Caiwang Tan, and Xiaoguo Song. Recent progress in laser additive manufacturing of aluminum matrix composites. *Current Opinion in Chemical Engineering*, 28:28–35, 2020.

[85] Muhammad Arif Mahmood, Andrei C Popescu, and Ion N Mihailescu. Metal matrix composites synthesized by laser-melting deposition: A review. *Materials*, 13(11):2593, 2020.

[86] Dongdong Gu, Sainan Cao, and Kaijie Lin. Laser metal deposition additive manufacturing of tic reinforced inconel 625 composites: influence of the additive tic particle and its starting size. *Journal of Manufacturing Science and Engineering*, 139(4), 2017.

[87] Ming-Yue Shen, Xiang-Jun Tian, Dong Liu, Hai-Bo Tang, and Xu Cheng. Microstructure and fracture behavior of tic particles reinforced inconel 625 composites prepared by laser additive manufacturing. *Journal of Alloys and Compounds*, 734:188–195, 2018.

[88] Jan Huebner, Dariusz Kata, Paweł Rutkowski, Paweł Petrzak, and Jan Kusiński. Grain-boundary interaction between inconel 625 and wc during laser metal deposition. *Materials*, 11(10):1797, 2018.

[89] Wanlu Li, Riufeng Di, Ruwang Yuan, Heyu Song, and Jianbo Lei. Microstructure, wear resistance and electrochemical properties of spherical/non-spherical wc reinforced inconel 625 superalloy by laser melting deposition. *Journal of Manufacturing Processes*, 74:413–422, 2022.

[90] Ting Rong, Dongdong Gu, Qimin Shi, Sainan Cao, and Mujian Xia. Effects of tailored gradient interface on wear properties of wc/inconel 718 composites using selective laser melting. *Surface and Coatings Technology*, 307:418–427, 2016.

[91] Ting Rong and Dongdong Gu. Formation of novel graded interface and its function on mechanical properties of wc1- x reinforced inconel 718 composites processed by selective laser melting. *Journal of Alloys and Compounds*, 680:333–342, 2016.

[92] Chen Hong, Dongdong Gu, Donghua Dai, Andres Gasser, Andreas Weisheit, Ingomar Kelbassa, Minlin Zhong, and Reinhart Poprawe. Laser metal deposition of tic/inconel 718 composites with tailored interfacial microstructures. *Optics & Laser Technology*, 54:98–109, 2013.

[93] Dongdong Gu, Chen Hong, Qingbo Jia, Donghua Dai, Andres Gasser, Andreas Weisheit, Ingomar Kelbassa, Minlin Zhong, and Reinhart Poprawe. Combined strengthening of multi-phase and graded interface in laser additive manufactured tic/inconel 718 composites. *Journal of Physics D: Applied Physics*, 47(4):045309, 2013.

[94] Sainan Cao and Dongdong Gu. Laser metal deposition additive manufacturing of tic/inconel 625 nanocomposites: Relation of densification, microstructures and performance. *Journal of Materials Research*, 30(23):3616–3628, 2015.

[95] G Bi, CN Sun, ML Nai, and J Wei. Micro-structure and mechanical properties of nano-tic reinforced inconel 625 deposited using laam. *Physics Procedia*, 41:828–834, 2013.

[96] Lan Chen, Yuzhou Sun, Lin Li, Yunpeng Ren, and Xudong Ren. In situ tic/inconel 625 nanocomposites fabricated by selective laser melting: Densification behavior, microstructure evolution, and wear properties. *Applied Surface Science*, 518:145981, 2020.

[97] GP Dinda, AK Dasgupta, and J Mazumder. Laser aided direct metal deposition of inconel 625 superalloy: Microstructural evolution and thermal stability. *Materials Science and Engineering: A*, 509(1-2):98–104, 2009.

[98] Vani Shankar, K Bhanu Sankara Rao, and SL Mannan. Microstructure and mechanical properties of inconel 625 superalloy. *Journal of nuclear materials*, 288(2-3):222–232, 2001.

[99] Elgiloy Speciality Metals. Inconel alloy 625. 2021.

[100] Special Metals. Inconel® alloy 625. 2013.

[101] Ariel Gamon, Edel Arrieta, Paul R Gradl, Colton Katsarelis, Lawrence E Murr, Ryan B Wicker, and Francisco Medina. Microstructure and hardness comparison of as-built inconel 625 alloy following various additive manufacturing processes. *Results in Materials*, 12:100239, 2021.

[102] Jafar Safarian and Leiv Kolbeinsen. Sustainability in alumina production from bauxite. *Sustainable Industrial Processing Summit*, pages 75–82, 2016.

[103] CES EduPack software. Alumina. 2020.

[104] Accuratus Ceramic Corporation. Aluminum oxide, al2o3 ceramic properties. 2013.

[105] astmsteel. Aisi 4140 steel bar | 1.7225 | 42crmo4 | scm440.

[106] AZO MATERIALS. Aisi 4140 alloy steel (uns g41400). 2019.

[107] ASTM International. Astm b213-97 standard test methods for flow rate of metal powders using the hall flowmeter funnel. 02.05:3, 2017.

[108] ASTM International. Astm b964-09 standard test methods for flow rate of metal powders using the hall flowmeter funnel. 02.05:3, 2016.

[109] André Alves Ferreira, Rui Loureiro Amaral, Pedro Correia Romio, João Manuel Cruz, Ana Rosanete Reis, and Manuel Fernando Vieira. Deposition of nickel-based superalloy claddings on low alloy structural steel by direct laser deposition. *Metals*, 11(8):1326, 2021.

[110] Abhijit Sadhu, Amit Choudhary, Sagar Sarkar, Amal M Nair, Pravanjan Nayak, Sagar Dadasahed Pawar, Gopinath Muvvala, Surjya K Pal, and Ashish Kumar Nath. A study on the influence of substrate pre-heating on mitigation of cracks in direct metal laser deposition of nicrsibc-60% wc ceramic coating on inconel 718. *Surface and Coatings Technology*, 389:125646, 2020.

[111] Mohammad Rabiey, Philipp Würsten, Lukas Senne, and Luca Urban. The effect of pre-and post-heat treatment on hardness and residual stress by laser metal deposition process of tungsten carbide (metcoclad 52052) cladding on a ck45 substrate. *Procedia CIRP*, 108:205–209, 2022.

Chapter 6

Appendix

- **A - MMC'S by AM methodologies study**

	Articles	DOI	Reinforcement Scale	Characteristics (Shape, Size)	Mixture Methodology	Process (DED, SLM)	Mixing Conditions (RPM, Time)	Reinforcement Concentration	Hardness and Wear Resistance
1	2020 - Alumina Reinforcement of Inconel 625 Coatings by Cold Gas Spraying	https://doi.org/10.3390/met10091263	micron	Inconel625 - Spherical Morphology: mean 23.77 µm and Alumina - irregular blocky shape: mean 60.31 µm	Powder	Cold Gas Spray	Spread Simultaneously, using two powder feeders instead of a powder mixture	i) 23 wt%, ii) 30 wt%, iii) 35 wt% e iv) wt45%	
2	1996 - Microstructure of Al2O3 Fiber-Reinforced Superalloy (INCONEL 718) Composites	https://doi.org/10.1007/BF02648422	micron	Two different alumina fibers - 20 µm FP diameter and 125 µm Saphikon diameter fibres	Foundry	Pressure Casting	Pressure Casting made for a 6000 second process with a maximum temperature of 1500 celcius degrees and a pressure of 3.6 Mpa	60% FP and 2% Saphikon	
3	2013 - Additive layer manufacture of Inconel 625 metal matrix composites, reinforcement material evaluation	https://doi.org/10.1016/j.jmatprotec.2013.06.021	micron	Inconel625 - Spherical Morphology - particle sizes (23.17, 31.28, 43.76) µm, alumina - irregular blocky shape (5.85, 8.48, 14.41) µm, SiC- irregular blocky shape (3.07, 4.60, 8.10) µm and TiC- irregular blocky shape(0.22,0.44, 1.18) µm	Powder	Powder Bed Fusion	Used 150 RPM during 1 hour	5 wt% (10% volume)	TiC - MacroHardness - 401HV and MicroHardness - 390 HV; Al2O3 - MacroHardness - 350 HV and MicroHardness - 300 HV
4	2015 - Laser additive manufacturing of ultrafine TiC particle reinforced Inconel 625 based composite parts: Tailored microstructures and enhanced performance	https://doi.org/10.1016/j.msea.2015.03.043	micron	Inconel625 - Spherical particles : 45-49 µm, TiC irregular shaped: 5-7 µm	Powder	Laser Melting Deposition	200 RPM during 8 hours	5 wt%	Wear Rate - 1,3e-4 mm^3/Nm
5	2019 - Microstructure, wear, and corrosion characterization of high TiC content Inconel 625 matrix composites	https://doi.org/10.1016/j.jmrt.2018.09.001	micron	TiC - size ranged from 1 to 19 µm - irregular shape	Fundição	Squeeze Casting	infiltration of the matrix (Inconel 625) melt at 1650 °C into a preform of the reinforcing TiCp	25%, 50% and 70%	
6	2018 - Microstructure and fracture behavior of TiC particles reinforced Inconel 625 composites prepared by laser additive manufacturing	https://doi.org/10.1016/j.jallcom.2017.10.280	micron	Inconel625 - spherical form (75-250) µm and TiC - Irregular Shape with particle size distribution (35-135) µm	Powder	Laser Additive Manufacturing	30 min mechanically mixed	15 wt%	TiC - MacroHardness - 236 HV and MicroHardness - 375 HV
7	2018 - Structure features of the composite materials Inconel 625/TiC, produced by LMD method	https://doi.org/10.1088/1742-6596/1109/1/012053	micron	Dispersibility of Inconel (50-140) µm and TiC (20-50) µm	Powder	Laser Metal Deposition	Was used three different methods: fed by single flasks, gravitational mixer with 60 RPM for 4h and in a planetary ball mill with 200 RPM for 8h	20%	
8	2016 - Microhardness and microstructure evolution of TiB2 reinforced Inconel 625/TiB2 composite produced by selective laser melting	https://doi.org/10.1016/j.optlastec.2016.01.010	micron	spherical Inconel 625 powders with particle size distribution of 11–45 µm were used. A cubic-shaped TiB2 with the particle size distribution 5–12 µm	Powder	Selective Laser Melting	Mixed in a Tumbler Mixing for 4h, RPM not mentioned	5 wt%	
9	2019 - Inconel 625/TiB2 Metal Matrix Composites by Direct Laser Deposition	https://doi.org/10.3390/met9020141	micron	Inconel 625- particle size 50-150 µm and TiB2 with a particle irregular shape size of 0.5 to 5 µm	Powder	Direct Laser Deposition	Only mentioned that were mixed in a planetary ball mill	5 wt%, 30 wt%, 50 wt%, 90 wt% and 100 wt%	
10	2015 - High-temperature oxidation performance and its mechanism of TiC/Inconel 625 composites prepared by laser metal deposition additive manufacturing	https://doi.org/10.2351/1.4898647	micron	Inconel625 - spherical form particle size distribution (15-45) µm and TiC - Irregular Shape with particle size distribution (4-7) µm	Powder	Laser Metal Deposition	Planetary Mill: 200 RPM for 10 hours	2.5 wt% and 5 wt%	
11	2020 - Graphene-strengthened Inconel 625 Alloy Fabricated by Selective Laser Melting	https://doi.org/10.1016/j.msea.2020.140099	micron	Graphene - 10 to 30 µm and spherical Inconel 625 powders of 15–53 µm	Powder	Selective Laser Melting	200 RPM	0.4 vol % and 1 vol%	MicroHardness - 0,4% - 320 HV and 1% - 350 HV
12	2018 - Grain Boundary Interaction between Inconel 625 and WC during Laser Metal Deposition	https://doi.org/10.3390/ma11101797	micron	Inconel625 - particle size 104 µm and WC - particle size of 5 µm	Powder	Laser Metal Deposition	90 min in a ball mill	10 wt%	MicroHardness -502 HV
13	2020 - Microstructure and properties of Inconel 625 + WC composite coatings prepared by laser cladding	https://doi.org/10.1007/s12598-020-01507-0	micron	Inconel625 - particle size 53 to 125 µm and WC - particle size of 15 to 45 µm	Powder	Laser Cladding	Planetary ball mill at 300 RPM for 2 h	10 wt%, 15 wt% and 20 wt%	MicroHardness: 10% - 382,24 HV, 15% - 427,82 HV and 20% - 536,98 HV
14	2022 - Microstructure, wear resistance and electrochemical properties of spherical/non-spherical WC reinforced Inconel 625 superalloy by laser melting deposition	https://doi.org/10.1016/j.jmapro.2021.12.045	micron	Inconel625 - particle size 53 to 150 µm, spherical WC - particle size of 53 to 109 µm and non-spherical WC - particle size of 15 to 45 µm	Powder	Laser Melting Deposition	Only mentioned that the powders were dried at 110 celcius degrees for 2 h	15 wt% for both WC reinforcements	MicroHardness - Spherical WC - 429,636 HV and Non-Spherical WC - 424,35 HV and Wear Loss/g - Spherical -0,007 and Non-Spherical - 0,053
15	2017 - Laser cladding of Inconel 625-based composite coatings reinforced by porous chromium carbide particles	https://doi.org/10.1016/j.optlastec.2017.03.007	micron	Inconel625 - average particle size 40 µm and Cr3C2 - particle size of 45-75 µm	Powder	Laser Cladding	mixed in a tumbler for minimum 0.5 h before the cladding process	40 wt%	

16	2018 - Enhanced wear resistance of laser cladded graphene nanoplatelets reinforced Inconel 625 superalloy composite coating	https://doi.org/10.1016/j.surfcoat.2017.12.047	micron	GNP's - particle size 8-12 µm and spherical Inconel625 - particle size 75-100 µm	Powder	Laser Cladding	Dried at 120°C for 2h, Ball milling - 300 RPM for 3 h in argon atmosphere, where the rotating direction changed every 30 min	11 wt%	MicroHardness - 255 HV and wear rate 3,91e-5 mm^3/Nm
17	2021 -Microstructure and Hardness Evolution of Solution Annealed Inconel 625/TiC Composite Processed by Laser Powder Bed Fusion	https://doi.org/10.3390/met11060929	micron	TiC - particle size 1 to 5 µm and spherical Inconel625 - particle size 10 to 50 µm	Powder	Powder Bed Fusion	e mixed in a ceramic jar in a ball milling system with the application of a speed rate of 60 rpm for 48 h	1 wt%	TiC -Macro Hardness - 341 HV
18	2021 - Characterization of the Structure, Mechanical Properties and Erosive Resistance of the Laser Cladded Inconel 625-Based Coatings Reinforced by TiC Particles	https://doi.org/10.3390/ma14092225	micron	TiC - particle size 50-150 µm and spherical Inconel625	Powder	Laser Cladding	Inconel625/ TiC were prepared, mixed and dried for 1 h at 50 -C	10, 20 and 40 vol %	Micro Hardness TiC : 10% - 278,4 HV , 20% - 293,94 HV and 40% - 324,55 HV. Wear Rate TiC: 10% - 0,53 mg/min, 20% - 0,49 mg/min and 40 % - 0,44 mg/min
19	2013 - Micro-structure and mechanical properties of nano-TiC reinforced Inconel 625 deposited using LAAM	https://doi.org/10.1016/j.phpro.2013.03.155	nano	spherical Inconel particle size of 20-45 µm and TiC nearly spherical particle size with a range of 80-150 nm	Powder	Laser Aided Additive Manufacturing	Dont mention the conditions	0.25%, 0.5% and 1%	MicroHardness - 0,25% - 317,7 HV, 0,5% - 318,6HV and 1 % - 321,9 HV
20	2017 - Laser Metal Deposition Additive Manufacturing of TiC Reinforced Inconel 625 Composites: Influence of the Additive TiC Particle and Its Starting Size	https://doi.org/10.1115/1.4034934	nano	spherical Inconel 625 with particle size distribution of 15–45 µm, the polyangular TiC micropowder with an average particle size of 2–5 µm and near-spherical TiC nanopowder with an average particle size of 40 nm	Powder	Laser Metal Deposition	Planetary ball mill at 200 RPM for 4 h	2.5 wt%	MicroComposites - Micro Hardness - 315 HV and Wear Resistance - 7e-4 mm^3/Nm and NanoComposites - Micro Hardness - 345 HV and Wear Resistance - 5e-4 mm^3/Nm
21	2016 - Microstructure and mechanical properties of Inconel 625/nano-TiB2 composite fabricated by LAAM	https://doi.org/10.1016/j.matdes.2016.08.078	nano	Inconel spherical shape and particle size of 20–45 µm and hexagonal nano-TiB2 powders with an average particle size of 58 nm	Powder	Laser Aided Additive Manufacturing	Planetary mill - 250 RPM for 12h	2.5 wt%	
22	2019 - Comparison of carbon-based reinforcement on laser aided additive manufacturing Inconel 625 composites	https://doi.org/10.1016/j.apsusc.2019.06.008	nano	spherical Inconel 625 powders with particle size distribution of 15–45 µm, Ni-coated MWCNTs with outside diameter of 30–50 nm and length of 10–20 µm and Graphite powder through 325 meshes sieve with 15 µm thickness	Powder	Laser Aided Additive Manufacturing	Planetary mill system - 50 RPM and 12 h of milling duration	0.25 wt%	
23	2014 -Fabrication of nano-TiCp reinforced Inconel 625 composite coatings by partial dissolution of micro-TiCp through laser cladding energy input control	https://doi.org/10.1016/j.surfcoat.2014.03.057	nano	Inconel 625 particle size 45–90 µm and TiC powder particle size 5–7 µm	Powder	Laser Cladding	ball milled for 8 h	5 wt.%	
24	2017 - Relation of microstructure, microhardness and underlying thermodynamics in molten pools of laser melting deposition processed TiC/Inconel 625 composites	https://doi.org/10.1016/j.jallcom.2016.09.098	nano	spherical Inconel 625 powder with the particle size distribution of 15-45 µm, irregular-shaped TiC nano-powder with an average particle size of 40 nm	Powder	Laser melting deposition	planetary ball mill - 200 RPM and a milling time of 4 h	2.5 wt%	
25	2015 - Laser metal deposition additive manufacturing of TiC/Inconel 625 nanocomposites: Relation of densification, microstructures and performance	https://doi.org/10.1557/jmr.2015.358	nano	spherical Inconel 625 powder with the particle size distribution of 15–45 lm and the irregularshaped TiC nano-powder with an average particle size of 40 nm	Powder	Laser metal deposition	planetary ball mill - 200 RPM and a milling time of 4 h	2.5 wt%	MicroHardness - 330 HV and Wear Rate - 5,40e-4 mm^3/Nm

26	2016 - Microstructural characteristics and mechanical properties of carbon nanotube reinforced Inconel 625 parts fabricated by selective laser melting	https://doi.org/10.1016/j.matdes.2016.09.080	nano	spherical Inconel 625 (IN625) powder with particle size distribution of 15–45 µm and the multi-walled carbon nanotube (MWCNTs) with inner diameter of 1–3 nm, outer diameter of 3–20 nm and length of 0.1–10 µm	Powder	Selective Laser Melting	Dried in an oven at 110 °C for 12 h and sieved	0.5 wt%	
27	2020 -Microstructure evolution, mechanical properties, and strengthening mechanism of TiC reinforced Inconel 625 nanocomposites fabricated by selective laser melting	https://doi.org/10.1016/j.msea.2020.139655	nano	Inconel625 (10–50 µm) and TiC with average size of 40 nm	Powder	Selective Laser Melting	Milling process was carried out for 12 h in an argon at?mosphere. The rotation speed was 200 RPM	4 wt%	
28	2017 - MICROSTRUCTURAL AND MECHANICAL STUDY OF INCONEL 625 – TUNGSTEN CARBIDE COMPOSITE COATINGS OBTAINED BY POWDER LASER CLADDING	https://doi.org/10.1515/amm-2017-0078	nano	Inconel 625 – average grain size of 104 µm angular shape and tungsten carbide – average grain size of 0.54 µm	Powder	Powder Laser Cladding	Powders were homogenized for 90 minutes in ball mill	10, 20 and 30 wt %	10% - 396,2 HV, 20% - 397,2 HV and 30% - 469,9 HV
29	2017 - Microstructure of laser cladded carbide reinforced Inconel 625 alloy for turbine blade application	https://doi.org/10.1016/j.ceramint.2017.03.194	nano	Inconel 625 powder having spherical particles of average diameter ϕ=104 µm. The tungsten carbide powder having angular grains of average diameter ϕ=0.64 µm	Powder	Powder Laser Cladding	500 RPM during 90 min	20 and 30 wt %	
30	2018 - Mechanical and tribological behaviors of graphene/Inconel 718 composites	https://doi.org/10.1016/S1003-6326(18)64841-1	micron	Inconel 718 alloy spherical powders - average particle size is 16.3 µm and multilayer GNPs have a platelet size ranging from 5 to 50 µm	Powder	Selective Laser Melting	3 h of stirring and sonication. the suspension is placed into a drying oven at 60 °C for 48 h to vaporize ethanol and obtain the mixture of metal composite powders that are ready for SLMprocessing	0.25 wt%, 1 wt%	MicroHardness - 0,25% - 424 HV and 1 % - 508 HV and Wear Rate - 0,25% - 0,56e-4 mm^3/Nm and 1% - 0,23e-4 mm^3/Nm
31	2013 - Laser metal deposition of TiC/Inconel 718 composites with tailored interfacial microstructures	https://doi.org/10.1016/j.optlastec.2013.05.011	micron	spherical Inconel 718 powder with the particle size distribution of ~45+15 µm and the irregular-shaped TiC powder (99.5% purity) with the particle size distribution of ~45+22.5 µm	Powder	Laser Metal Deposition	planetary mill using a ball-to-powder weight ratio of 5:1, a rotation speed of the main disc of 200 rpm, and a milling time of 4 h.	25 wt%	MicroHardness - 453 HV and Wear Rate - 4,80e-5 mm^3/Nm

32	2018 - The Role of Reinforcing Particle Size in Tailoring Interfacial Microstructure and Wear Performance of Selective Laser Melting WC/Inconel 718 Composites	https://doi.org/10.1115/1.4040544	micron	spherical Inconel 718 powder with the particle size distribution of 15–45 µm and e polygonalshaped WC particles with the initial average size of 21 µm	Powder	Selective Laser Melting	planetary ball milling using a ball-topowder weight ratio of 5: 1, a rotation speed of the main disk of 200 rpm, and the mixing time of 0 h, 4 h, and 8 h	25%	
33	2016 - Formation of novel graded interface and its function on mechanical properties of WC1-x reinforced Inconel 718 composites processed by selective laser melting	https://doi.org/10.1016/j.jallcom.2016.04.107	micron	spherical Inconel 718 powder with the particle size distribution of 15-45 µm, spherical shaped reinforcing WC1-x particle with the size distribution of 25-45 µm.	Powder	Selective Laser Melting	planetary ball mill using a ball-to-powder weight ratio of 4:1, a rotation speed of the main disc of 200 rpm, and a milling time of 4 h	25 wt%,	Micro Hardness - 389,4 HV and wear rate - 2,3e-4 mm^3/Nm
34	2017 - Selective Laser Melting of Graphene-Reinforced Inconel 718 Superalloy: Evaluation of Microstructure and Tensile Performance	https://doi.org/10.1115/1.4034712	micron	Inconel 718 - spherical shape with average particle size of 40 µm and The graphene nanoplatelets platelet size range from 5 to 50 µm.	Powder	Selective Laser Melting	graphene nanoplatelets are added into ethanol with ultrasonic wave applied. Second, Inconel 718 powders are added into the graphene nanoplatelets suspension followed by 3 h of stirring and sonication. Finally, the suspension is placed into a drying oven at 60˚C for 48 h to vaporize ethanol and obtain the mixture of metal powders and graphene nanoplatelet	0.25%, and 1%	
35	2018 -Microstructure evolution, mechanical response and underlying thermodynamic mechanism of multi-phase strengthening WC/Inconel 718 composites using selective laser melting	https://doi.org/10.1016/j.jallcom.2018.03.049	micron	spherical pre-alloy Inconel 718 powder with an average diameter of 30 µm and irregular-shaped WC with average size of 10 µm	Powder	Selective Laser Melting	planetary ball mill with a duration of 4 h	20 wt%	MicroHardness - 475 HV
36	2020 - Microstructure and Tensile Performance of Graphene Reinforced Inconel 718 Alloy Via Selective Laser Melting and Post-Treatments	https://doi.org/10.1115/1.4045765	micron	The Inconel 718 powders have a spherical shape with an average particle size of 40 µm and the graphene nanoplatelets have a thickness of 6–8 atomic layers and size of 5–25 µm	Powder	Selective Laser Melting	The Inconel 718 and GNPs powders are premixed in ethanol using the ultrasonication method and then dried in an oven to vaporize mixing agent.	4.4 vol%	
37	2020 - Development of process maps based on molten pool thermal history during laser cladding of Inconel 718/TiC metal matrix composite coatings	https://doi.org/10.1016/j.surfcoat.2020.126100	micron	Inconel 718 and TiC powder was in the range of 43–100 µm and 5–20 µm respectively	Powder	Laser Cladding	Low energy ball milling of Inconel 718 and TiC in selected proportions was carried out for uniform distribution	30%, 50% and 70%	
38	2020 - Ti2AlC triggered in-situ ultrafine TiC/Inconel 718 composites: Microstructure and enhanced properties	https://doi.org/10.1016/j.jmst.2020.04.002	micron	spherical Inconel 718 powder and e flake?shaped Ti2AlC powders with the particle size distribution 3–11 µm	Powder	Reactive hot-pressing sintering	planetary mono-mill with a ball-to-powder weight of 5:1. The milling process was conducted for 10 h at a rotation speed of 300 RPM	5 vol.%, 10 vol.% and 15 vol.%	
39	2017 - Thermo-mechanical improvement of Inconel 718 using ex situ boron nitride-reinforced composites processed by laser powder bed fusion	https://doi.org/10.1038/s41598-017-14713-1	micron	spherical IN718 with a particle size of 10-45 µm and BN nanosheets with D50 of 0.2 µm	Powder	Powder Bed Fusion	milling occurred at 150 RPM for 24 h	6 and 12 vol%	

40	2020 - In situ TiC/Inconel 625 nanocomposites fabricated by selective laser melting: Densification behavior, microstructure evolution, and wear properties	https://doi.org/10.1016/j.apsusc.2020.145981	nano	spherical IN625 with a particle size of 10-50 µm and TiC with a mean size of 40 nm	Powder	Selective Laser Melting	The ball-to-powder weight ratio and disk rotation speed were 5:1 and 200 rpm, respectively. To avoid powder agglomeration, the mixing time was set to 12 h with a 15 min interval every 2 h.	6 wt%	MicroHardness - 440 HV and Wear Rate 3,5e-4 mm^3/Nm
41	2016 - Direct Diode Laser Cladding of Inconel 625/WC Composite Coatings	https://doi.org/10.5545/sv-jme.2015.3194	micron	spherical IN625 with a particle size of 40-100 µm and WC with a mean size of 100-200 µm	Powder	Direct Diode Laser Cladding	doenst mention	60 vol %	Micro Hardness - 500 HV
42	2014 -Combined strengthening of multi-phase and graded interface in laser additive manufactured TiC/Inconel 718 composites	https://doi.org/10.1088/0022-3727/47/4/045309	micron	spherical Inconel 718 powder with the particle size distribution of 15–45µm and irregular shaped TiC powder with the particle size distribution of 22.5–45µm were used	Powder	Laser Metal Deposition	6 planetary ball mill using a ball-to-powder weight ratio of 5 : 1, a rotation speed of the main disc of 200 rpm, and a milling time of 4 h	25 wt%	Wear Rate - 1,8e-4 mm^3/Nm
43	2016 - Effects of tailored gradient interface on wear properties of WC/Inconel 718 composites using selective laser melting	https://doi.org/10.1016/j.surfcoat.2016.09.011	micron	size distributions of the two kinds of particles were 25–45 µm and 15–45 µm, for spherical WC and Inconel 718	Powder	Selective Laser Melting	6 planetary ball mill using a ball-to-powder weight ratio of 4:1, a rotation speed of the main disk of 200 rpm, and a milling time of 4 h	25 wt%	Micro Hardness - 393,2 HV and Wear Rate - 2,5e-4 mm^3/Nm
44	2022 - A study on selective laser melting (SLM) of TiC and B4C reinforced IN718 metal matrix composites (MMCs)	https://doi.org/10.1016/j.jallcom.2021.163527	micron	IN718 powders are observed tobe spherical-shaped having a particle size distribution in the range of 5–40 µm The as-received TiC and B4C powder particles are irregular shaped, having sharp edges, with particle size of 2–15 µm and 30–55 µm, respectively	Powder	Selective Laser Melting	WC balls with a ball to powder ratio (BPR) of 10:1, for 3 h with a rotation speed of 300 rpm	10,20 and 30 vol %	Micro Hardness - 10 vol% - 519 HV ,20 vol% - 565 HV and 30 vol% - 619 HV and wear volume - 10 vol% - 0,259, 20 vol % - 0,116 and 30 vol%-0,457 mm^3

- **B - Metco 51060A Powder Data Sheet**

Material Product Data Sheet
Spherical Cast Tungsten Carbide – Nickel Alloy Powder Blends

Powder Products:
Metco 51060A, Metco 51059A, Metco 51058

1 Introduction

Metco™ 51060A, Metco 51059A and Metco 51058 are 60/40 blends of spherical, cast tungsten carbide (CTC-S) and self-fluxing matrix materials. This combination of a very hard phase material (tungsten carbide) and a corrosion resistant matrix results in a product that is suitable for laser cladding or PTA deposits that resist erosion from particulates in slurries.

The metallic matrix constituent of the blend is gas atomized that ensures chemical homogeneity and a spherical morphology. All three products employ a nickel chromium silicon boron matrix; however, Metco 51059A has a higher chromium content for better corrosion and erosion resistance and improved flow. Metco 51058 has a coarser particle size distribution and provides excellent protection against high-stress abrasion for stabilizer applications.

The tungsten carbide constituent is manufactured using a unique process that results in a fine non-acicular structure with greater hardness and superior hardness compared to that of conventional fused and crushed tungsten carbide. The high apparent density and improved flow raise the amount of hard phase material present in the clad deposit.

Quick Facts

Classification	Carbide blend
Chemistry	WC 40(NiCrSiBC)
Manufacture	Gas atomized blend
Morphology	Spheroidal
Service Temperature	≤ 500 °C (930 °F)
Apparent Density	6 – 8 g/cm³
Hardness	2700 – 3100 HV0.1
Purpose	Wear and erosion resistance
Process	Laser Cladding, PTA

2 Material Information

2.1 Chemical Composition

Product	Weight Percent (typical)								
	Hard Phase 60 %			Metal Matrix 40 %					
	W	C	Fe	Ni	Cr	Si	B	Fe	C
Metco 51060A	Balance	3.8	< 0.3	Balance	6.8 – 8.3	3.1 – 3.9	1.4 – 1.9	1.7 – 3.3	0.1 – 0.4
Metco 51059A	Balance	3.8	< 0.3	Balance	9.5 – 12.5	3.4 – 4.3	1.9 – 3.6	2.1 – 3.5	0.3 – 0.6
Metco 51058	Balance*	3.8	< 0.3	Balance	6.8 – 8.3	2.8 – 3.6	1.4 – 1.9	1.7 – 3.3	0.1 – 0.4

2.2 Particle Size Distribution, Apparent Density and Former Designation

Product	Nominal Particle Range (µm)	Apparent Density (g/cm³)	Former Product Designation
Metco 51060A	–106 +45	6.0 – 8.0	MetcoClad 52052
Metco 51059A	–106 +45	6.0 – 8.0	WOKA 6050S PlasmaDur 53003 MetcoClad 53003
Metco 51058	–150 +53	6.0 – 8.0	---

Size analysis using sieve (ASTM B214).

- **C - Residue and Virgin Powder Microstructure Images**

  Residue

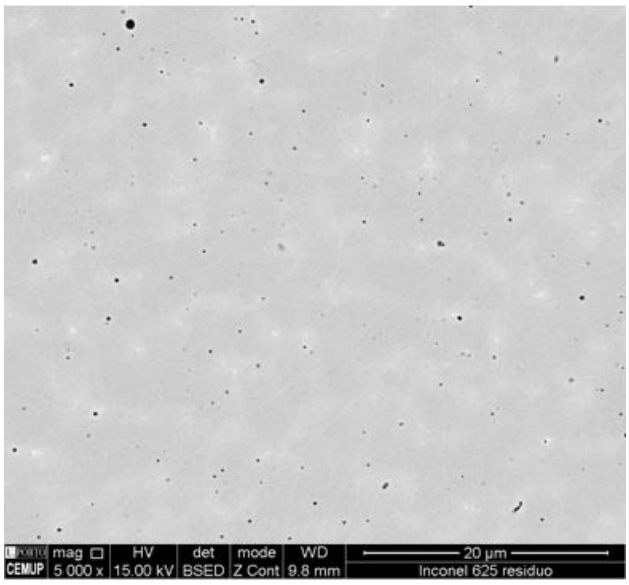

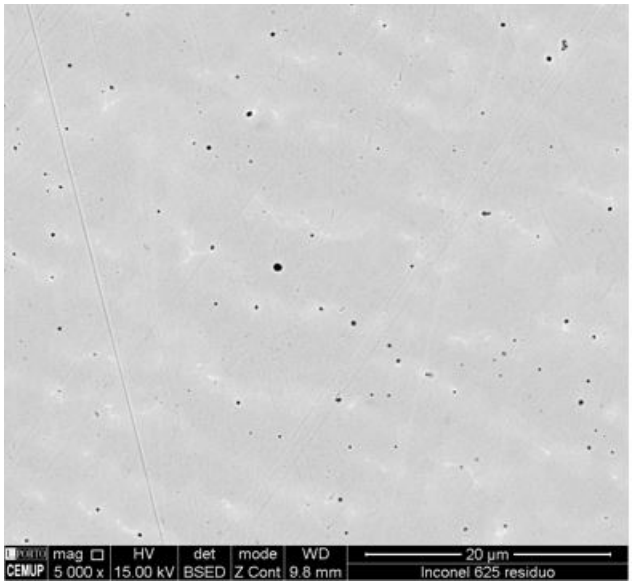

  Virgin

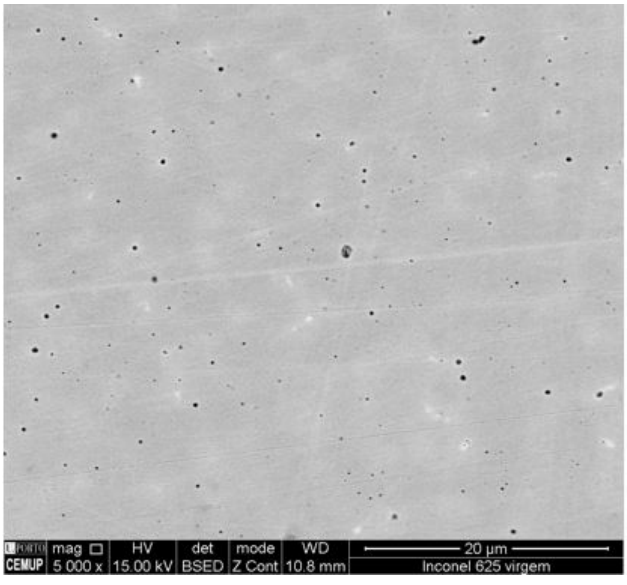

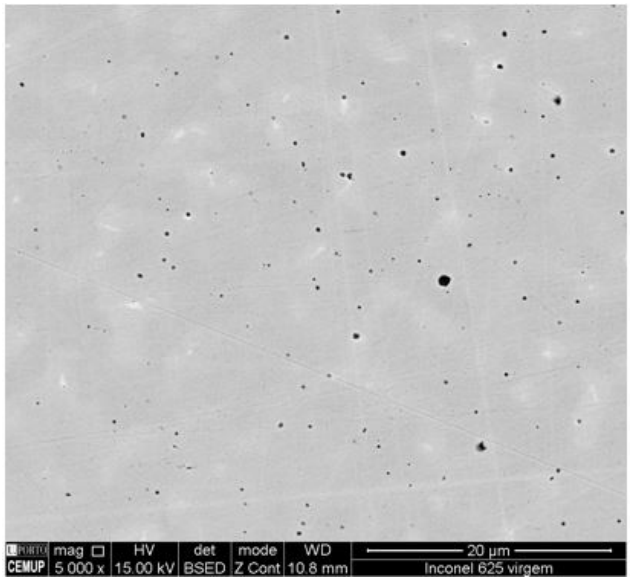

- **D - Metco 51060A microscopic images**

  One layer Plane

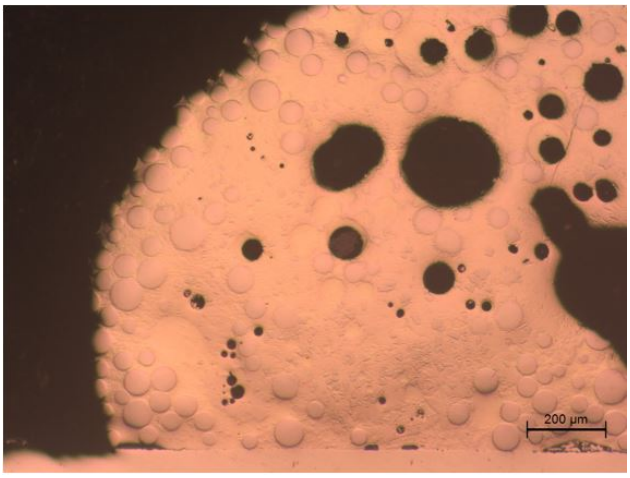

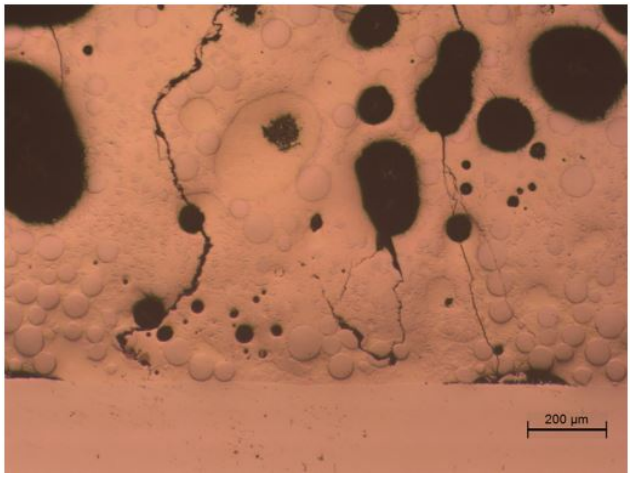

  Three Layer Plane